Evaluation of the Cycle Profile Effect on the Degradation of Commercial Lithium Ion Batteries

Karthik Narayanan Radhakrishnan

Dissertation submitted to the faculty of the Virginia Polytechnic Institute and State University in partial fulfillment of the requirements for the degree of

Doctor of Philosophy

In

Mechanical Engineering

Michael W Ellis – Chair

Douglas J Nelson

Michael von R Spakovsky

Robert B Moore

Partha P Mukherjee

08/02/2017

Blacksburg, Virginia

Keywords: Lithium ion batteries, capacity degradation, cycle profile

Evaluation of the Cycle Profile Effect on the Degradation of Commercial Lithium Ion Batteries

Karthik Narayanan Radhakrishnan

ABSTRACT

Major vehicle manufacturers are committed to expand their electrified vehicle fleet in upcoming years to meet fuel efficiency goals. Understanding the effect of the charge/discharge cycle profiles on battery durability is important to the implementation of batteries in electrified vehicles and to the design of appropriate battery testing protocols. In this work, commercial high-power prismatic lithium ion cells were cycled using a pulse-heavy profile and a simple square-wave profile to investigate the effect of cycle profile on the capacity fade of the battery. The pulse-heavy profile was designed to simulate on-road conditions for a typical hybrid electric vehicle, while the simplified square-wave profile was designed to have the same charge throughput as the pulse-heavy profile, but with lower peak currents. The batteries were cycled until each battery achieved a combined throughput of 100 kAh. Reference Performance Tests were conducted periodically to monitor the state of the batteries through the course of the testing. The results indicate that, for the batteries tested, the capacity fade for the two profiles was very similar and was 11 % ± 0.5 % compared to beginning of life. The change in internal resistance of the batteries over the course of the testing was also monitored and found to increase 21% and 12% compared to beginning of life for the pulse-heavy and square-wave profiles respectively. Cycling tests on coin cells with similar electrode chemistries as well as development of a first principles, physics based model were done in order to understand the underlying cause of the observed degradation. The results from the coin cells and the model suggest that the loss of active material in the electrodes due to the charge transfer process is the primary cause of degradation while the loss of cyclable lithium due to side reactions plays a secondary role. These results also indicate that for high power cells, the capacity degradation associated with the charge-sustaining mode of operation can be studied with relatively simple approximations of complex drive cycles.

Evaluation of the Cycle Profile Effect on the Degradation of Commercial Lithium Ion Batteries

Karthik Narayanan Radhakrishnan

GENERAL AUDIENCE ABSTRACT

Major vehicle manufacturers are committed to expand their electrified vehicle fleet in upcoming years to meet fuel efficiency goals. Understanding the effect of the charge/discharge cycle profiles on battery durability is important to the implementation of batteries in electrified vehicles and to the design of appropriate battery testing protocols. In this work, commercial lithium ion cells were tested using two profiles with the same energy transfer; a pulse-heavy profile to simulate on-road conditions for a typical hybrid electric vehicle, and a simplified square-wave profile with the same charge flow as the pulse-heavy profile, but with lower currents. Cycling tests on coin cells with similar electrode chemistries as well as development of a first principles, physics based model were done in order to understand the underlying cause of the degradation. The results suggest that the degradation observed is not dependent on the type of profile used. These results also indicate that for high power cells, the capacity degradation associated with the charge-sustaining mode of operation can be studied with relatively simple approximations of complex drive cycles.

Acknowledgements

I would like to take this opportunity to thank everybody who has helped me during this incredible journey. I could not have done it without your support and encouragement.

I would like to thank my advisor, Dr. Ellis for taking me in as his graduate student, for all the advice and support over the years.

I would also like to thank Dr. Nelson for serving on my dissertation committee and for his valuable inputs and suggestions for the experiments and model.

I would like to thank Dr. von Spakovsky, Dr. Moore and Dr. Mukherjee for serving on my dissertation committee.

Special thanks to my fellow graduate students Jeremey Beach for putting up with all my questions when I was new, for being a great friend through the years and for all the great music in the lab. Thanks to Dr. Sridharan Ramesh for all the support through the years and all the fun road trips.

I also want to thank Ford motor company for their sponsorship of this project via their university research program (URP), and a special thanks to Thomas Coupar for all the help and inputs relating to battery testing and model development.

Finally, but most importantly, I would like to thank my family for all the unconditional love, support and encouragement they have shown over the years. My mom Latha Radhakrishnan and dad KN Radhakrishnan for their weekly skype calls, their regular reminders to take care of myself, their constant prayers for my success and pampering whenever I got a chance to visit them. Thank you to all my uncles, aunts, cousins and friends for cheering me on from the sidelines. A special shout out to my beloved departed grandma who was always excited and yet amazed at the same time to be video chatting with her (favorite) grandson living thousands of miles away.

Contents

Table of Figures

List of Tables

Chapter 1 - Introduction

1.1 Durability of Lithium Ion Batteries

Rechargeable lithium ion batteries are rapidly emerging as the dominant energy storage technology. Since their introduction in 1990 by Sony, they have become the primary energy storage medium for a variety of applications. Whether it is for personal electronic devices such as phones, tablets or computers or for the emerging battery electric vehicle (EV) or hybrid electric vehicle (HEV), lithium ion batteries provide the necessary energy. Major vehicle manufacturers including Ford, GM, Tesla, Nissan, Toyota, etc. all have pure battery electric vehicles and/or hybrid electric vehicles for sale. The increasing focus on sustainable energy and reduced greenhouse gas emissions makes "local" zero emission vehicles such as all-electric vehicles and fuel cell vehicles an important future platform for the transportation industry. The key advantage of lithium ion technology, high specific energy (Wh/kg), was recently demonstrated by a two pilot team that completed an around the globe flight in a solar powered plane using lithium ion batteries as the storage device for the energy supplied by their solar panels. In a more practical application, commercial aircraft manufacturers like Boeing are starting to use lithium ion battery packs in their aircraft for weight savings. The use of lithium ion batteries in portable consumer electronic devices and in mobile power applications has become attractive because, when compared to other older technology like nickel cadmium or lead acid batteries, lithium ion batteries offer higher specific energy as well as energy density (Wh/liter), little or no memory effects, and a lower rate of self-discharge over time.

If the cost of lithium ion technology can be reduced, lithium ion batteries may also see increased usage in stationary energy storage applications. For example, with the increasing global energy demand by developing nations and the growing call for the reduction of greenhouse gas emissions, more importance is being given to the development of sustainable energy sources such as solar and wind energy. However, due to the unpredictable and uncontrollable nature of these sustainable sources, a mismatch between generation and demand for power is inevitable. Addressing this mismatch will require the development of smart grids and large-scale energy storage devices including lithium ion technology. Thus, rechargeable lithium ion battery technology is poised to be one of the most important energy storage media for these applications as well.

Pure lithium has a high theoretical specific energy of around 11 kWh/kg [1]. Energy storage technology that uses lithium can take advantage of this theoretical energy advantage. However, rechargeable batteries based on a pure lithium negative electrode though desirable, have proven difficult to build and operate with acceptable cycle life and safety. Pure lithium negative electrodes eventually suffer from dendrite formation on charging, and thus experience short circuits and catastrophic failure due to the breach of the separator material by the dendrites. The reactivity of pure lithium is also a safety concern in the event of battery failure or damage.

Instead of a pure lithium negative electrode, modern lithium ion batteries make use of insertion materials[1] for both the negative and positive electrodes. While insertion materials have lower specific energy when compared to pure lithium, they allow for dendrite free cycling and enhanced safety. Lithium ion batteries that use insertion materials consist of three components: (1) a negative electrode usually made of carbon or graphite, coated on a copper current collector; (2) a positive electrode made of a lithium metal oxide ($Li_xM_yO_2$), coated on an aluminum current collector; (3) a separator that physically separates the electrodes to prevent short circuits, usually made of a porous polymer that is imbibed with an electrolyte to allow the diffusion of lithium ions (but not electrons). The electrolyte is usually a lithium salt dissolved in an organic solvent, for example, $LiPF_6$ in ethylene carbonate. Lithium ion batteries can have theoretical specific energy values in excess of 250 Wh/kg and theoretical energy densities in excess of 500 Wh/liter. Technologies used previously, nickel metal hydride batteries for example, have nominal specific energy and energy densities in the range of 70 Wh/kg and 250 Wh/liter respectively, which is roughly half of that of lithium ion battery chemistry [2].

1.2 Working of the Lithium Ion Battery

The operation of a typical lithium ion battery is shown schematically in Figure 1. The battery charges and discharges as the lithium ions are either inserted or removed from the intercalation host material. During this intercalation process, ideally, there would be no change in the structure of the host material. During the charge process, while the negative electrode is reduced Eq. (1.1), the positive electrode is oxidized Eq. (1.2). During the discharge process, the reactions are reversed. The overall charge/discharge equation is indicated in Eq. (1.3).

[1] Insertion materials are defined as host structures into/from which guest species (i.e. lithium ions) can be reversibly inserted or extracted without inducing significant structural changes in the host material

$$C_6 + aLi^+ + ae^- \underset{\text{discharge}}{\overset{\text{charge}}{\rightleftharpoons}} C_6Li_a \quad (1.1)$$

$$Li_xM_yO_2 \underset{\text{discharge}}{\overset{\text{charge}}{\rightleftharpoons}} Li_{(x-a)}M_yO_2 + aLi^+ + ae^- \quad (1.2)$$

$$Li_xM_yO_2 + C_6 \underset{\text{discharge}}{\overset{\text{charge}}{\rightleftharpoons}} Li_{(x-a)}M_yO_2 + C_6Li_a \quad (1.3)$$

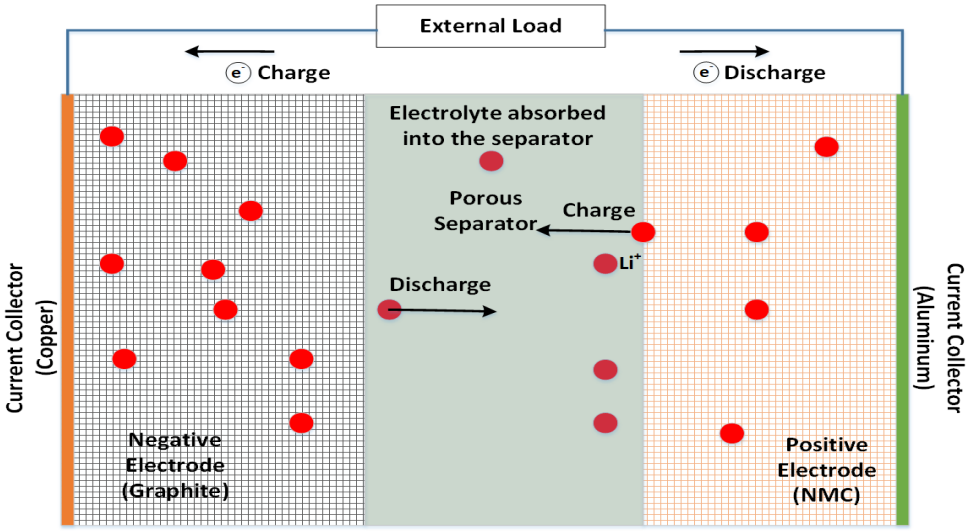

Figure 1: Schematic representation of a Li ion battery

During the charge process, the lithium intercalates into the carbon negative electrode due to the application of an external potential. Due to the potential applied, the lithium ion is forced out of the positive electrode, diffuses through the separator, and then intercalates into the negative electrode material. Due to the absence of metallic lithium, which is quite reactive chemically, these intercalation negative electrodes are inherently safer than pure lithium electrodes. The intercalation of the lithium usually happens in between the layered structure of the graphite and results in the introduction of an amount "a" of lithium atom per six carbon atoms where $0<a<1$. During discharge, this intercalation process is reversed, and the discharge process occurs spontaneously, when the circuit to which the battery is connected is closed. The lithium intercalated in the graphite layers, de-intercalates at a rate that depends on the resistance of the external load, and diffuses back to the positive electrode. The lithium ions then intercalate back into the positive electrode. The $Li_xM_yO_2$ structure of most positive electrodes allows for the placement of lithium and the

transition metal M in alternative layers in octahedral sites of the cubic lattice. This allows for easier extraction of the lithium ions during the charge process [3].

During the charge process, as the lithium ions diffuse into the carbon material, the intercalation process results in a decrease in the potential of the negative electrode until it reaches about $0.005 \leq V \leq 0.01$ V vs. Li/Li^+. This reduction in the potential, as shown in Figure 2 [4] is to be expected as the potential of a fully lithiated carbon negative electrode is very close to that of pure lithium, thus leading to such small potentials against Li/Li^+. Figure 2, also shows that the open circuit potential (OCP) of the graphite negative electrode is relatively flat from around 10 percent to 85 percent depth of discharge (DOD) and then steeply rises from around 85 percent to 100 percent DOD. Generally, the battery is designed in such a manner that the majority of the operational range of the negative electrode is in the relatively flat region between 10 percent and 85 percent DOD.

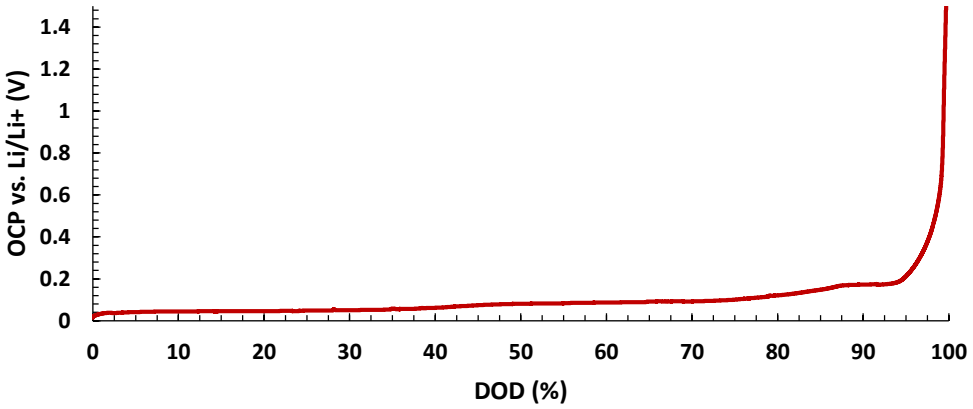

Figure 2: Negative electrode OCP vs Li/Li^+ as a function of depth of discharge

During the charge process, the positive electrode undergoes oxidation as the electrode loses an electron and the transition metals go to higher valences. The lithium ions then travel to the negative electrode via the electrolyte and the electrons move towards the negative electrode via an external circuit. From Figure 3, which shows the OCP vs. DOD relationship of an NMC positive electrode, it can be observed that as the lithium content of the electrode goes towards a minimum (DOD goes towards 100 percent), the potential of the positive electrode vs. Li/Li^+ also decreases.

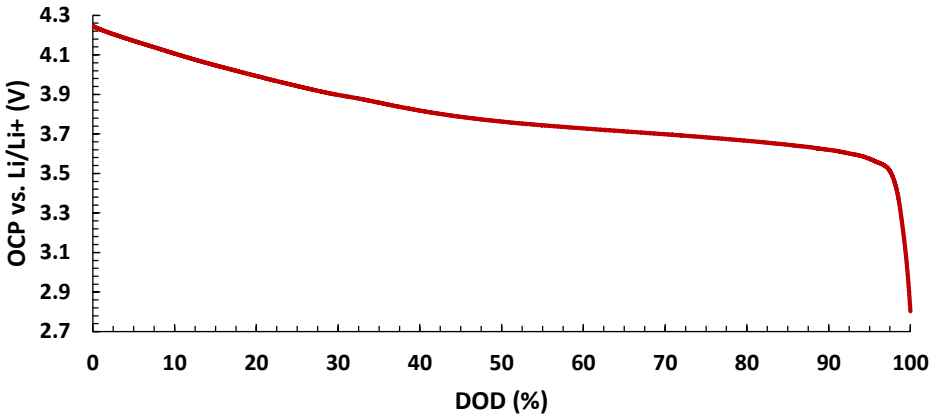

Figure 3: Positive electrode OCP vs Li/Li^+ as a function of depth of discharge

Changing the positive electrode structure, chemical composition etc. can affect this potential vs. DOD relationship. This chemistry dependent OCP vs. DOD relationship of the positive electrode determines the shape of the voltage profile of the battery. Eq. 1.4 shows that the OCV of the battery is given by the difference in open circuit potentials between its two electrodes. Usually, the positive electrode is also the main determinant of the capacity of the battery. Generally, the negative electrode materials can accommodate more lithium than the positive electrode material can provide, thus making the positive electrode the capacity limiting electrode [5].

$$V_{battery,OCV} = \phi_{cathode,OCP} - \phi_{anode,OCP} \tag{1.4}$$

While the electrons in a lithium ion battery transfer from one electrode to the other via an external circuit, the charge transfer inside the battery occurs due to the transport of lithium ions from one electrode to the other through the electrically insulating separator via the electrolyte. The electrolyte, which facilitates this transport, is typically a lithium salt dissolved in a solvent. One of the most common electrolytes in a lithium ion battery is $LiPF_6$ dissolved in an equal mixture of ethylene carbonate (EC) and di-methyl carbonate (DMC). This combination is particularly effective due to high ionic conductivity as well as low viscosity. Usually, in a single carbonate solvent, these two properties are mutually exclusive [6]. The electrolyte, in addition to facilitating the flow of ions inside the battery, also ensures the formation of a passivating protective layer on the negative electrode during the initial charge cycles of the battery called the solid electrolyte interphase (SEI). This layer is crucial to the working of the lithium ion battery and allows the transport of lithium ions to the intercalation electrode while preventing the transport of other

species. The choice of electrolyte also plays an important role in determining the performance of the battery. Usually, during the operation of the battery, there is a potential drop across the electrolyte due to the ionic conductivity as well as a gradient in the concentration of lithium ions. The transport properties of the electrolyte effectively determine this potential drop underscoring the importance of choosing the proper electrolyte for the battery. Recently, emphasis is being placed on developing solid polymer electrolytes and liquid electrolytes that are stable beyond 4.5 V vs. Li/Li^+. Successful development and adoption of such electrolytes will contribute significantly towards increased safety and specific energy in lithium ion batteries.

Though lithium ion batteries have become the main energy storage device for portable devices and are becoming increasingly attractive for automotive and stationary applications, many areas for improvement remain. The specific energy and energy density requirements set by the United States Advanced Battery Council (USABC) (250 Wh/kg and 400 Wh/l) have been met in lab-scale batteries by the use of advanced materials and composites [7]; the cost per kWh target of $125/kWh is not yet a reality. Currently, the cost per kWh is still above $220/kWh [7]. The lithium ion system also faces challenges in terms of capacity fade, safety (thermal runaway for example) and low temperature performance. The capacity and power fade caused by calendar ageing and cycling is one of the most challenging problems faced by lithium ion battery researchers. The USABC in the 2012 “FreedomCAR” initiative calls for fifteen years of calendar life for hybrid electric vehicles. It also calls for 5000 charge depleting and 300,000 charge sustaining cycles [8]. Achievement of these durability targets requires mitigation of the loss of cyclable lithium ions in side reactions (and the related increase in battery impedance) and the loss of active material at both the positive and negative electrodes. While the capacity fade phenomenon in lithium ion batteries has been extensively studied, there is still much that is not yet fully understood. For example, the majority of the side reactions that persist through the life of the battery and consume cyclable lithium ions have not been identified. These reactions if identified and understood, could lead to the development of techniques and technologies that could mitigate the effects of the reactions or stop them completely. Alternatively, consider the case of positive electrodes containing manganese where, studies have shown that the manganese ions can participate in side reactions involving lithium not only leading to cyclable lithium loss but also leading to the structural damage in the positive electrode due to removal of active material [9]. Better electrolyte salts, solvents and additives could be developed so that the capacity fade and impedance rise is minimized. While the

effects of temperature on lithium ion batteries have been well-studied [2], [10], [11], [12], [13], [14], current research is focused on designing improvements to the thermal management systems that work with current chemistries rather than the development of new materials/chemistries that can work safely under higher temperatures. Development of such novel materials can lead to lowered chances of thermal runaway situations.

It is also important to understand how the application affects durability. Intuitively, it could be expected that the capacity fade would depend on driving conditions such as road and traffic conditions, individual driving styles, etc. However, this work has shown [15] that batteries subjected to two different profiles experienced differences in the internal resistance change but little difference in capacity fade. Finally, there is a need for testing large-scale batteries. Most of the published literature uses small-scale batteries as representations of full-scale commercial batteries. While this provides reasonable information about the specific processes, tests on large-scale batteries would give real world information for the overall battery, which can be very useful for the industry in terms of battery design, and the development of better battery management systems. In addition, the availability of large-scale battery data can allow researchers studying smaller scale batteries in the laboratory to compare their results and identify potential areas of disagreement and pursue avenues to correct for such discrepancies.

1.3 Research Objectives

The work proposed for this research project is focused on understanding how charge/discharge cycle profiles affect battery durability. Specifically, this work seeks to understand whether commercial batteries subjected to charge/discharge cycles that correspond to different drive cycles but that involve the same charge throughput yield similar results for capacity fade. Furthermore, we would like to develop a sufficient understanding of the mechanisms underlying capacity fade to determine whether our results can be generalized to other types of cycle profiles and battery applications. The proposed work is organized into three tasks.

1.3.1 Task 1: Determine the effect of cycle profile on capacity fade in commercial batteries

In this task, large-scale commercial lithium ion batteries are cycled using two different profiles to establish whether the profile influences the capacity fade and degradation mechanisms. Specifically, two battery packs are subjected to a pulse heavy profile representative of a small HEV sedan executing the US06 drive cycle and a simple square profile, respectively. These

profiles were created to have the same charge transfer (i.e. RMS current) to isolate the effect of profile characteristics from the effect of charge throughput. Analysis of the test data after cycling will identify differences in the capacity fade between the two profiles. Results from this task will indicate whether simpler and less expensive battery testing protocols can be used to simulate the capacity fade and degradation a battery pack might experience during real world applications. This data can also help establish whether auto manufacturers can reliably predict parameters like battery lifetime, warranty-period, etc. regardless of the driving behavior of the person buying the vehicle. Finally, results from this task will serve as validation data for a first principles model of the battery performance.

1.3.2 Task 2: Develop a validated first principles model to help interpret the experimental results

A model derived from the fundamental equations that govern physical processes like ion transport, diffusion, charge transfer, etc. is developed to extend our understanding of how different parameters affect the performance and life of the battery. The results are compared to results from charge/discharge tests and from other data analysis techniques such as incremental capacity analysis and differential voltage analysis to help identify the significance of mechanisms like loss of lithium, loss of active materials, impedance rise, etc. that are responsible for capacity fade. Additionally, the model also identifies of the key processes and parameters (e.g., particle sizes, volume fractions, diffusion coefficients, etc.) that affect the battery performance and durability. By contributing to a greater understanding of the origins of capacity fade and the processes occurring within a lithium ion battery, this effort helps in understanding the extent to which results from the experimental effort can be generalized to other cycles and applications.

1.3.3 Task 3. Construct lab-scale coin cells, subject them to cycles that result in behavior similar to the commercial cells, and then examine degradation mechanisms

Cycling tests that result in a voltage response similar to the commercial cells are conducted on coin cells of similar chemistry and qualitatively similar construction. The use of coin cells provides capabilities not available with the commercial cells including the ability to conduct post mortem studies and report detailed observations; the ability to independently assess anode and cathode materials relative to a common lithium reference electrode, and the ability to conduct studies quickly since the coin cells have fewer safety concerns and can be cycled continuously (i.e., without supervision). In addition, since the coin cells are assembled from materials with known

properties, they provide another useful tool for assessing the validity of the modeling exercise in Task 2. The results from the coin cell studies, together with the modeling effort, allow for a thorough understanding of the results observed in the commercial cells and can help establish the extent to which conclusions from this work can be extended to other battery designs and applications.

Chapter 2 - Literature Review

The discussion of the capacity fade phenomenon of lithium ion batteries can be divided into two related areas; (1) capacity fade mechanisms and (2) the effects of operational conditions on the mechanisms. Capacity fade mechanisms are quite complex and the degradation of the battery comes from various interconnected processes that involve the electrodes and the operational conditions.

2.1 Capacity Fade Mechanisms

2.1.1 Negative Electrode Contribution to Capacity Fade

The most common negative electrode material used today in lithium ion batteries is graphite [16]. Carbon in other forms such as amorphous carbons coated on tin oxide and TiO_2, and amorphous carbon – graphene composites are also being considered as negative electrodes [17], [18]. However, graphite continues to be of primary interest to researchers and industry as a negative electrode material due to its low cost, its ability to intercalate one lithium atom per six carbon atoms (stoichiometry) and its relative resistance to cracking compared to non-carbon alternatives (e.g. silicon). The electrochemical potential of graphite is very close to lithium making it an ideal lithium insertion negative electrode material. The reversible insertion of lithium into graphite occurs below 0.2 V vs Li/Li^+, with insertion observed between 0.09 – 0.14 V vs Li/Li^+ [19]. Graphite is comprised of carbon atoms arranged in hexagonal rings. Planes made of these hexagonal rings stacked on top of each other make up the structure of graphite. These planes are held together by van der Waals forces. The insertion of lithium into graphite occurs between the graphene planes according to the reaction

$$C_6 + aLi^+ + ae^- \rightleftharpoons C_6Li_a \tag{2.1}$$

Theoretically, the capacity of the graphite negative electrode is 372 mAh/g [20]. The capacity of the negative electrode never really reaches this theoretical value after the initial formation cycle. The capacity of the negative electrode also continues to fade as the battery ages. The capacity reduction or fade in the negative electrode can be attributed to

- Initial Solid Electrolyte Interphase (SEI) formation
- Continued SEI growth during ageing
- Physical changes to the electrode
- Lithium plating

SEI Formation

Lithiated graphite will react with air, moisture and most electrolytes under certain conditions. To prevent this from happening, lithium ion batteries are assembled in the discharged state when there is no lithium in the negative electrode. During the initial charging process, lithium intercalates into the negative electrode for the first time. The charge transfer during this initial process usually exceeds the theoretical capacity of the negative electrode as the lithium ions are consumed in side reactions involving the electrolyte and results in the formation of the solid electrolyte interphase (SEI). During this first cycle, the electrolyte which is typically quite unstable at low and very high potentials vs Li/Li^+ reacts with the carbon electrode and the lithium intercalating into it. These reactions reduce the electrolyte causing it to decompose and form a solid layer on the graphite electrode particles while evolving gaseous products [8], [16]. These reactions consume not just the electrolyte but also the lithium ions thus leading to irreversible loss of lithium and the formation of the SEI. After formation, this SEI layer ideally passivates the negative electrode particles from further reactions and thus further loss of cyclable lithium. The first few charge – discharge cycles are called the formation cycles and are part of the battery manufacturing process. The charge transfer during these formation cycles decreases with each cycle until the SEI reaches a condition that is relatively stable. The charge transfer observed after reaching this relatively stable condition is then reported as the nominal capacity by the manufacturer.

The amount of irreversible capacity loss experienced by a lithium ion battery during the formation cycle varies with the cycling conditions, electrode materials, electrolyte, etc. The SEI formation is usually expected to happen over a few cycles and the thickness of the SEI layer, which has been estimated between 1 and 10 nanometers, depends on factors such as formation current, surface area of the negative electrode material, electrolyte additives, electrolyte solvents and the temperature of the battery. The voltage at which the SEI formation occurs is not a fixed value and neither is the formation rate. Reports in literature suggest values between 0.5 - 2.0 V vs Li/Li^+ however, 0.8 V vs Li/Li^+ is a practical value that has gained acceptance [16].

The SEI is a very complex system consisting of organic and inorganic components. Models of the SEI [21], [22] suggest that the layer consists of inorganic lithium compounds close to the graphite followed by a porous layer consisting of organic lithium salts and some LiF. Depth profiling of the SEI shows different chemistries at different locations [23], [24]. The locations where the lithium intercalates into the graphite (the basal planes and defects) show the presence of organic compounds and polymers whereas the lateral surface shows the presence of lithium and fluorine. The composition of the SEI is also dynamic in nature depending on the chemistry of the cell. Some of the reaction products are known to dissolve in the electrolyte and precipitate later causing the composition to vary with time.

The SEI forms directly on the surface of the particles comprising the negative electrode, so the material properties of the particles directly influence the SEI. Composition and morphology of the negative electrode including the type of carbon used, any pretreatment done to the carbon and the surface area of the carbon being used affect the irreversible capacity loss associated with the formation of the SEI. The higher the surface area of the carbon used, the more the initial capacity loss [16]. Graphite usually has a different specific surface area when compared to amorphous carbon. Two types of carbons with the same specific surface area but with different morphologies were shown to have different irreversible capacity losses [25]. In addition to carbon characteristics, the SEI is influenced by a variety of other factors including the type of carbon, the electrolyte salt, the solvent used for the salt, electrolyte additives, and any surface defects and active sites. Any pretreatment done to the carbon before the assembly of the cell also plays a role in the characteristics of the SEI. Various pretreatments like reduction of the negative electrode material as well as the suppression and removal of certain surface functional groups by etching have been explored in an effort to change the characteristics of the SEI and reduce the irreversible capacity loss to varying degrees of success. For example, the reduction of the graphite before assembly of the cell led to a thick but brittle SEI layer and the etching process resulted in an improved specific charge capacity, which was attributed to the formation of nano cavities in the graphite [16].

Once the SEI forms, ideally it allows the diffusion of lithium ions to and from the negative electrode during the charging and discharging of the battery. At the same time, it restricts the transport of all other species that may be present in the electrolyte. Thus, the SEI layer limits further degradation of the electrode by stopping the reactions involving the electrolyte, cyclable

lithium and negative electrode material. While the SEI layer ideally passivates the negative electrode from further degradation, it is a poor conductor and its formation does increase the impedance of the battery.

Continued SEI growth

In an ideal case, the SEI forms a passivating layer allowing the transport of lithium through to the graphite planes and preventing the further reduction of electrolyte and corrosion of the carbon. However, the SEI never behaves in an ideal manner and continues to allow the diffusion of impurities, solvated lithium ions and electrolyte species. This non-ideal behavior of the SEI continues past the formation period and extends into the life of the battery thus allowing a slow but continuous reduction of the electrolyte and its solvents by lithium, leading to the loss of cyclable lithium, corrosion of the lithiated negative electrode and further capacity loss along with simultaneous growth of the SEI during the service life. The continuous albeit slow growth of the SEI after formation, and the resulting capacity fade has been extensively studied [1], [8], [26], [27], [28], [29].

The formation mechanisms and the reactions that lead to the formation of various degradation products is still highly debated. The various operating conditions and battery testing conditions also contribute to a considerable amount of ambiguity when it comes to establishing consistent reaction mechanisms. However, there is a general agreement regarding the identity of the degradation products. Some common reaction products identified and published in the literature are included in Table 1 [23], [30], [31], [32], [33], and [34] where, "R" stands for some organic species (e.g.C_2H_3O).

Table 1: List of common side reaction products in a lithium ion battery

$(CH_2OCO_2Li)_2$	$ROCO_2Li$	Li_2CO_3	ROLi
LiF	Li_2O	LiOH	$Li_2C_2O_4$

The properties of the SEI depend on the composition of the electrolyte. The most common salt used in the electrolyte, $LiPF_6$, is known to produce HF and PFO_3 by reacting with the solvents used, both of which are highly reactive to both the negative electrode and the positive electrode.

Despite this disadvantage, $LiPF_6$ is more suitable than some of the other commercially available lithium salts. For example, $LiClO_4$ is explosive; $LiBF_4$ provides BF_4^- ions that cause problems with passivation of the negative electrode; $LiSO_3CF_3$ has low conductivity etc. [35]. The type of solvent and the concentration of the electrolyte salt plays a critical role in the type of reaction products formed. For example, polycarbonates and Li_2CO_3 are known to appear in electrolytes using ethylene carbonate (EC) and propylene carbonate (PC). However, the Li_2CO_3 disappears under high EC and PC concentrations giving way to reaction products like $ROCO_2Li$ [16]. The dielectric constants, viscosity and polarity of these solvents may also play a role in the determination of reaction products [36]. The chemistry of the electrode-electrolyte interphase is further complicated by inter-species reactions. For example, in battery systems containing $LiBF_4$ and $LiPF_6$ in EC and dimethyl carbonate (DMC) the Li_2CO_3 formed will react with HF (provided by the hydrolysis of the salt) and form LiF and CO_2. LiF has been identified as one of the contributors to the instability of the SEI [37]. The rate at which these reactions occur during regular cycling is much lower than during the initial formation cycles. However, considering the long life expectancy of lithium ion batteries meant for heavy-duty applications, the continuous growth of the SEI and the corrosion of the negative electrode are major contributors to the overall capacity fade over the life of the battery. Also, considering that the SEI grows throughout the service life of a lithium ion battery, the impedance of the battery will also continue to increase, possibly leading to increased power fade as the battery ages [38], [39].

Physical Changes to the Electrode

The cyclic intercalation and dis-intercalation of lithium causes physical changes to the graphite particles as their volume changes with the insertion of lithium. During the charging process, the lithium intercalates into the graphene layers as given by Eq. (2.1) and this process causes a volume change in the material, which is on the order of 10 percent [40]. Since the majority of the passivating surface layer or SEI is formed during the initial formation cycles, it will also have to accommodate the volume change by expanding and contracting with the graphite particles. It is theorized that during repeated cycling, the surface film cracks creating macro pores thus exposing fresh negative electrode surfaces to the electrolyte and allowing the kind of reactions that created the SEI in the first place to happen albeit at a slower rate. These changes in the particle and thus the SEI volume become more important as we consider heavy-duty applications, for example, in

a HEV, where the rapidly changing road conditions could cause the particle to expand and contract at much faster rates.

In addition to the volume changes, the graphite particles can fracture due to other effects such as gas evolution and exfoliation. It is known that certain reactions that consume lithium evolve gasses like ethylene, hydrogen, carbon dioxide and carbon monoxide [21]. When these reactions happen in crevices that occur in the graphite, the resulting solid reaction products can block the passage of the evolved gasses. This causes a localized increase in pressure that can easily crack the graphite particles. Fracture in the negative electrode particles can lead to loss of physical contact between the graphite particles or between the graphite particles and the copper current collector. In addition to the physical loss of contact, the cracking also exposes fresh graphite surface for lithium-consuming side reactions to occur. Physical changes in the graphite particles can also arise from the use of certain electrolyte solvents. For example, when propylene carbonate is used as the solvent, graphite exfoliation is observed. This exfoliation is explained by the co-intercalation of solvent molecules into the structured graphite layers along with lithium. The ordered structure of the graphite is subsequently distorted or destroyed when the intercalated solvent molecules undergo secondary reactions [41]. Loss of electrical continuity or exfoliation of graphite layers leads to carbon material that is not active. The result of these processes is denoted, “loss of active material”.

Lithium Plating

Metallic lithium plating is generally rare in the normal operating voltage window of the lithium ion battery. However, if the battery is charged beyond 4.2 V – 4.3 V, or used in certain high current charge conditions, for example, during regenerative braking in an electrified vehicle, the lithium instead of intercalating into graphite can form a metallic lithium layer on the graphite. This occurs when the lithium is moving into the negative electrode faster than it can diffuse into the carbon, thus causing an excess of lithium on the carbon particles that can lead to plating. This situation is further exacerbated by low operating temperatures, which are possible in automotive applications. Graphite when compared to other carbons like coke or other hard carbons [42] is especially susceptible to lithium plating as its electrochemical potential is very close to that of the lithium deposition potential, around 50 mV - 100 mV vs Li/Li^+ [43], [44]. Battery Management Systems

(BMS) are designed to prohibit the overpotentials needed to plate lithium onto graphite. However, deliberate over-lithiation of negative electrodes has shown that lithium plating can occur on the negative electrode [44]. Any metallic plating of lithium onto the negative electrode will increase the capacity fade of the battery, as metallic lithium is highly reactive to organic species. This accelerates the reactions that deposit solid products on the negative electrode. This accelerated growth of the passivating layer, will in turn, increase the impedance and cause higher overpotentials. A further effect of lithium plating is that a film of lithium over the negative electrode particles eventually exhibits dendrite formation, piercing the separator and causing short circuits. Lithium plating also reduces the inherent safety of the battery, as solid lithium is known to increase the chances of a thermal runaway reaction causing fires and/or explosions [43].

2.1.2 Positive Electrode Contribution to Capacity Fade

The energy density, charge capability and power density of a lithium ion battery is also dependent on the type of positive electrode material used [29]. Generally, the positive electrode is fabricated from relatively expensive metal oxides and is a major determinant of the cost of the battery. The positive electrode of a lithium ion battery, like the negative electrode, is an intercalation material. The lithium ion battery is assembled in a state of discharge (i.e., the lithium is intercalated into the positive electrode) during the assembly process. During the charge process, the transition metals lose electrons and undergo oxidation to higher valences and the lithium in the positive electrode solvates into the electrolyte solution, diffuses through the separator, and intercalates into the negative electrode [45]. During discharge, the lithium ions are intercalated back into the positive electrode and the electrons from the negative electrode reduce the transition metals to lower valences. The rate of this reduction process and the rate of lithium insertion decide the overpotentials and, thus, the voltage response of the battery which is analogous with performance [45]. The most common positive electrode materials in use today for lithium ion batteries are oxides of transition metals like cobalt, nickel, manganese, etc. Different structures of these transition metal oxides are used as electrodes, with the most common oxides being layered compounds ($LiMO_2$), spinel compounds (LiM_2O_4) and olivine compounds ($LiMPO_4$) where M stands for the transition metal.

Like the negative electrode, the positive electrode in a lithium ion battery also contributes to the capacity fade associated with batteries as they age. For example, changes in the positive electrode as the battery ages can result in the inability to accept lithium thus reducing capacity also referred to as 'loss of active material' or the morphological changes can also affect the overpotentials and overall impedance of the battery. However, the positive electrode contribution to the overall capacity fade is generally less than the negative electrode contribution. The positive electrode contribution to fade also varies from one battery to the other as the chemistry and morphology of the positive electrode material dictate the capacity fade mechanisms [8]. Additionally, the positive electrodes are generally more susceptible to high temperature capacity fade than negative electrodes. Currently the most important transition metal in consideration as a positive electrode material in high power and energy applications is manganese. Manganese is being considered as a replacement for cobalt in the positive electrode as it is much cheaper and more abundant than cobalt and it is more environmentally friendly when compared to cobalt, which is known to be a toxic heavy metal [46]. The capacity fade at positive electrodes containing manganese can be attributed to structural changes and to manganese dissolution due to chemical changes.

Structural Changes in the Positive electrode

The positive electrode material usually has manganese ions in different valences namely Mn^{3+} and Mn^{4+}. However, when the amount of Mn^{3+} ions in the positive electrode is more than 50 percent, the positive electrode is susceptible to distortion [47]. This distortion is classified as "Jahn – Teller" distortions. During the discharge process, lithium ions travel more quickly through the electrolyte than through the spinel positive electrode particle. This results in an aggregation of lithium ions on the surface of the positive electrode particle and this in turn creates areas of high Mn^{3+} concentration that induces the Jahn-Teller distortion. This effect is usually exacerbated with increased discharge rates. In positive electrodes containing high concentrations of Mn^{3+} ions, the cubic structure of the spinel positive electrode changes to a tetragonal structure causing a large direction dependent or anisotropic volume change and damage to the spinel during the charge-discharge process. This volume change and the presence of cubic and tetragonal structures causes a mismatch between planes and changes the lithium diffusion pathways thus leading to loss of active material and hence to capacity fade.

Capacity fade due to Jahn-Teller distortions has however been reduced by partial substitution of manganese in the spinel with cations of other metals like aluminum, cobalt, chromium and magnesium. In addition to these metals, excess lithium has also been used to reduce the manganese content [48]. These methods of substituting other metals for manganese has led to a reduction in the number of Mn^{3+} ions in the positive electrode, thus providing increased stability by reducing the chances of the Jahn-Teller distortions. These improvements have led to a reduction in the volume change during cycling causing less damage to the spinel. In addition to the substitutions, the use of nano-sized materials may reduce damage to the electrode particles, thus mitigating capacity fade [9]. This reduction in particle damage is attributed to the ability of entire nano domains to reversibly switch between the cubic and tetragonal structures upon lithium intercalation and de-intercalation [46].

Chemical Changes and Manganese Dissolution

Manganese ions are known to dissolve into the electrolyte solution in positive electrodes made of spinel material [9]. This dissolution leads to capacity fade, as it is a loss of active material. Two models explain the dissolution of manganese into the electrolyte. The first model addresses the decomposition of the Mn^{3+} ions at low potentials. At low positive electrode potentials vs. Li/Li^+ (i.e., at higher depth of discharge), the Mn^{3+} ions decompose according to the reaction

$$2Mn^{3+} \longrightarrow Mn^{4+} + Mn^{2+} \tag{2.2}$$

Here the Mn^{4+} product is a solid whereas the Mn^{2+} ions are soluble and diffuse into the solution reacting with other species in the solution to form carbonates and oxides of manganese. Since the structure of the spinel is maintained, the vacancies left by the dissoluted manganese is filled by lithium leading to a lithium rich spinel. The second model suggests manganese dissolution by catalytic activity of HF [49]. In the previous sections, the production of HF in batteries containing $LiPF_6$ was discussed. The $LiMn_2O_4$ can react in the presence of hydrofluoric acid to produce MnF_2 according to the reaction

$$Li_{(1-x)}Mn_2O_4 + 2(1-x)HF \longrightarrow \frac{(3+x)}{4}\lambda Mn_2O_4 + (1-x)LiF + (1-x)H_2O + \frac{(1-x)}{2}MnF_2 \tag{2.3}$$

These reaction products like MnF_2 deposit on the positive electrode surface causing an increase in the impedance of the battery. In addition, the manganese ions (Mn^{2+}) dissolved in the electrolyte solution diffuse through the separator, react with the various species on the SEI and deposit in the SEI. Additionally, the Mn^{2+} ions can react with the electrolyte solvent causing electrolyte degradation as well. This deposition of manganese on the negative electrode SEI can also lead to self-discharge of the lithiated negative electrode material due to electrolyte decomposition [49].

2.1.3 Electrolyte Additives

Most commercial batteries are manufactured with a variety of electrolyte additives, which affect the formation and continued growth of the SEI. Most of the electrolyte additives that affect the negative electrode can be classified as reducing agents, reactive agents and morphology modifiers [26]. Reductive type additives like vinylene chloride (VC) or vinyl ethylene carbonate are reduced preferentially during the initial SEI formation process and are known to replace some of the solvent reduction reactions thus changing the initial irreversible capacity loss and the composition of the SEI. Reactive agents are not reduced during the initial SEI formation but rather react with some of the intermediate compounds and radicals or final reaction products during cycling to form compounds that are more stable. This in turn creates a SEI that is more stable against the electrolyte and solvents. For example, isocyanate compounds used as additives scavenge any water or HF produced due to other reactions. HF has been shown to change the composition of the SEI and is responsible for the dissolution of Mn from the positive electrode. Reactive type additives like lithium bis (oxalato) borate or LiBOB for short are known to suppress the reduction of electrolyte solvents like PC thus stabilizing the interphase during extended cycling. Though these types of additives do not necessarily reduce the initial irreversible capacity loss, they stabilize the SEI during the life of the battery and reduce the capacity loss during cycling. Morphology modifiers like boron-based receptors react with LiF produced by the reaction of Li_2CO_3 with HF. This removal of LiF stabilizes the SEI. Potassium salts added to the electrolyte on the other hand decrease the solvation of the Li^+ ions in the solvents (since the K^+ ions are more selective) and reduce the intercalation of solvent molecules into the graphite thus decreasing graphite corrosion and solvent reduction reactions [50].

2.2 Effect of Operational Conditions on Capacity Fade

2.2.1 Temperature Effects

Temperature plays a very important role in the capacity fade of the lithium ion battery. In an electric vehicle, the battery pack might experience ambient temperatures ranging from negative 25 °C to 50 °C during operation depending on the geographical location. In addition to the influence of the ambient air temperatures, the temperature of the battery is affected by the thermal energy released during the charge-discharge process. This thermal energy originates from reactions at the negative and positive electrodes and from electrical and ionic resistances [10]. The wide operational temperature window and the internal thermal energy release make thermal management an important issue for lithium ion batteries systems. The critical nature of thermal management was highlighted when the Nissan Motor Company announced the replacement of battery packs for their Leaf battery vehicle due to severe capacity fade when operating in hot climates like Arizona. Both excessively low and high temperatures can have detrimental effects on the lithium ion battery.

Low Temperature Effects

When lithium ion batteries operate under cold conditions, they can deliver up to 90 percent of their discharge capacity whereas it is impossible to charge the battery back to its original state under cold conditions [11]. The detrimental effects of low temperatures are attributable to the occurrence of lithium plating at the negative electrode. The rate of lithium intercalation into the negative electrode depends directly on the temperature dependent diffusion coefficient of lithium into graphite. At low temperatures (below 0°C), this diffusion coefficient is low enough that instead of intercalating into the negative electrode, the lithium starts plating on the negative electrode. As long as this low temperature is maintained, the plated lithium will not diffuse into the negative electrode particles causing the observed difference between the discharge and charge capacities. This lithium plating also leads to permanent capacity fade. Metallic lithium is quite reactive towards the organic species and the solvents in the electrolyte producing organic and inorganic deposits on the SEI. These reactions consume cyclable lithium eventually leading to capacity fade. In addition to capacity fade, the additional deposits on the negative electrode also increase the impedance of the electrode causing power fade.

High temperature Effects

During high temperature operation of the lithium ion battery (above 45 °C), the dissolution of manganese into the solvent and the subsequent deposition on the negative electrode SEI is accelerated. Certain species in the SEI can also dissolve at elevated temperatures and react with the manganese ions and the electrolyte causing increased impedance in the negative electrode due to deposition of these reaction products. Compounds of manganese like oxides and fluorides have also been shown to redeposit on the positive electrode creating a passivating layer that restricts the passage of lithium thus reducing the capacity and power of the battery [12].

The safety of the battery is also an important consideration at higher temperatures. In cases where there is poor or no thermal management, thermal runaway reactions can happen leading to hazardous conditions. Thermal runaway is caused when high temperatures inside the battery cause exothermic reactions between the electrolyte and other species/materials in the battery, thus further increasing the internal temperature and accelerating the reactions ultimately leading to battery fires [2]. A proposed mechanism identified in the literature involves the SEI exothermally decomposing above 70°C. The resulting energy release is then either absorbed by the separator causing it to melt and creating a short circuit and more subsequent energy release or absorbed by the electrolyte solvents, which then vaporize. These vaporized organic compounds combust easily in the presence of oxygen, which can be generated easily by the decomposition of the oxygen rich positive electrode at high temperatures. In case of extreme thermal runaway, there is a possibility of the aluminum current carrier melting if the battery has not already exploded due to the combustion of vaporized products [13]. All of these situations call for adequate battery thermal management and quick removal of heat from the battery during cycling.

2.2.2 Effect of Charge/Discharge Rates

In an electrified vehicle, the batteries experience both discharge and charge conditions. Discharge occurs at a rate determined by the driver's demand for power. Charging occurs at a rate determined by the battery management system as it interacts with the charging station or with the regenerative braking system. The magnitude of current flowing to and from the battery during a drive cycle or a regenerative cycle can vary significantly based on the driving conditions. For example, batteries can experience large current draws when the vehicle is under heavy acceleration or the battery pack can experience high charge rates if the vehicle control system is set to operate at high

regenerative braking conditions. Besides the regenerative cycle, charging stations can be designed to supply energy at high charge rates in order to reduce charging time.

Some studies have shown that cycling at high rates can have a detrimental effect on the batteries resulting in increased capacity fade and impedance [51], [52], [53], and [54]. In the previous sections, the effects of volume changes in the negative electrode, and structural changes in the positive electrode, on the capacity and power fade of the lithium ion battery were noted. These changes in the electrodes occur due to cyclic lithium insertion and de-insertion and, the rate at which the lithium ions diffuse into and out of the electrodes directly depends on the current flow or the C-rate[2]. Large C-rates tend to exacerbate the effects of the structural changes that occur in the electrodes leading to increased degradation. Lithium plating on the negative electrode and its effect on the side reactions were also noted in the previous sections. Lithium plating tends to occur in the electrode during high C-rate cycling when, the lithium ions move into the electrode faster than they can diffuse into the electrode particles. In addition to the physical changes in the electrodes, temperature effects were also discussed in the previous sections. Higher C-rates can lead to higher working temperatures in the batteries. The battery temperature is dictated by the amount of thermal energy generated due to current flow and the action of the thermal management system. The amount of thermal energy generated in the battery is proportional to the square of the current as given by the expression I^2R. This dependency of temperature on the C-rate ensures that the higher the C-rate or current flow, the higher the battery temperature. Studies indicate that batteries cycled at higher temperatures with higher rates show increased degradation compared to batteries cycled with similar rates at lower temperatures [55], [56], and [57].

Most studies, [51], [52], [53], [54], [55], [56], [57] that try to understand the effect of cycling on the degradation of the battery, do not take the regenerative braking experienced by an electrified vehicle into consideration and focus on cycles in which the battery is discharged until it reaches the lowest permissible SOC. In these tests, the batteries are repeatedly charged at low rates, while discharging between the permissible voltages at high rates to observe degradation caused by high discharge rates. For example, [54], [58], [59], [60], and [61] use CC-CV charge and CC discharge cycles between the limiting voltages to study the degradation. Studies such as [24] and [11] use

[2] A 1C-rate simply refers to either fully charging or discharging the nominal capacity over a period of one hour. In the case of the commercial batteries used in this study, a rate of 1C refers to a current of 5 A since these batteries have a nominal capacity of 5 Ah.

the USABC dynamic stress test (DST) and the PNGV power assist cycle to study the effects of degradation. There are a few studies [57], [62] and [63], that try to assess the power fade in high power batteries using the charge sustaining (CS) cycle test profile as established in the FreedomCar manual [64]. However, this profile is a constant power discharge and charge process separated by a rest period. This test profile, while suitable to study the power fade in the batteries, does not fully consider the varying loads that can be imposed by a profile designed to simulate on-road conditions. There are a few studies that include cycle life testing using a charge-sustaining cycle somewhat comparable to the cycle used in this study [65], [66], [67], [68], and [69]. The effect of cycling batteries made with a NMC-LMO composite positive electrode using a charge sustaining cycle profile was reported in [12], and [13], and capacity loss of around 4 percent was observed after 10 - 15 kAh of cycling. In addition, the studies conducted in [65] consider a cycle derived from on-road conditions to evaluate the effect of cycling on battery behavior and to assess the difference between temperature dependent calendar ageing and cycle ageing. That study concluded that cycle ageing was the main contributing mechanism for degradation but storage at high temperatures can result in comparable calendar ageing.

2.3 Models to Understand Capacity Fade

Models that emulate the operation of the battery using key parameters affecting capacity fade can support a deeper understanding of the capacity fade mechanisms. For example, a physics based model can help to deconvolute the mechanisms leading to the behavior observed in certain curves generated by analysis techniques such as differential voltage analysis (DVA) or incremental capacity analysis (ICA). By directly manipulating parameters like active material fractions or internal resistance, the model-generated analysis curves can be compared to the experimental analysis curves for similarities in the evolution of such curves. A useful model must capture the relevant physical processes and must be validated by comparison to experimental data. Mathematical models found in the literature usually employ one of two methods. The first, an equivalent circuit method, is highly parametric in nature and requires accurate EIS data for calibration [70], [71], [72], and [73]. The second method, a first principles model involves simplifying and solving a system of partial differential equations, and algebraic expressions that describe the thermodynamics, electrochemistry, and transport processes to obtain the battery voltage [4], [67], [74], [75], and [76].

The equivalent circuit model (example shown in Figure 4) attempts to emulate the battery by representing it as an electrical circuit. This type of model relies upon the electrical circuit to recreate the input-output characteristics of the battery. As seen in the figure, Most equivalent circuit models, such a the one illustrated in the figure, have a voltage source V_0, that serves as the OCV of the battery, a resistance in series that serves as the ohmic resistance of the battery, (which includes both the electrodes and the electrolyte), and a resistor capacitor pair that serves to mimic the transient response of the battery during the charge-discharge process. Other types of circuit components such as Warburg elements can be added for higher complexity by models that try to identify diffusion related dynamics in a battery. Though equivalent circuit models can represent physical concepts like voltage, resistance, etc., they cannot directly relate the battery behavior to detailed physical properties and processes.

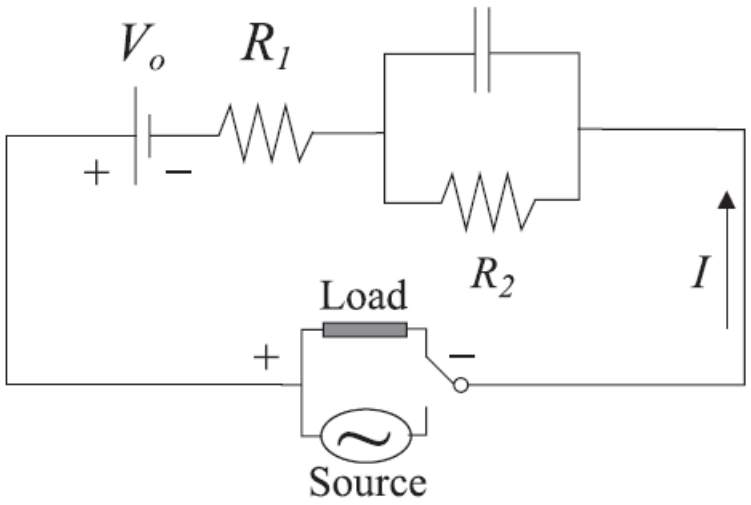

Figure 4: Example of an equivalent circuit model [77]

Most models based on first principles, called porous electrode models stem from the so-called porous electrode theory developed by Newman et al. [78]. These types of models consider the transport of ions from one electrode to the other via diffusion as well as other physical processes like reaction kinetics that control the voltage behavior of the battery. These models frequently use simplifying assumptions about the electrodes and the ion species. The single particle model (SPM) used in this study is an example of this type of model where, a single particle is assumed representative of the average behavior of the electrodes [27]. The extent of the simplifying assumptions determines the complexity of the model. For example, earlier, simpler models based

on the SPM ignored the effects of the lithium concentration gradient in the electrolyte [58], [79]. On the opposite end of the spectrum, some models ignore the SPM and consider the gradient of lithium along the thickness of the electrode in addition to the concentration gradient in the electrolyte[80], [81]. A high fidelity battery simulation program to study the degradation in batteries developed by the Department of Energy with Argonne National Lab can be considered a prime example of a model at the complex end of the modelling spectrum [82]. The equations governing the physical processes used in the present implementation of the SPM model are discussed in detail in Chapter Four (Section 4.2 The Single Particle Model).

There are several techniques used to solve the differential equations and algebraic expressions used in physics based models. Some studies consider analytical expressions derived from one-dimensional heat and mass transfer problems for obtaining the concentration of lithium in the electrode [83], [84]. These analytical solutions, while providing acceptable results regardless of the C-rate, can often lead to convoluted solution methods while trying to solve the equations that govern the transport processes in the cell, especially when the boundary conditions are time dependent. A method often used to avoid such complexities is to replace the analytical solution with some approximation that sacrifices accuracy for ease of computation. One such approximation is to consider an approximate polynomial solution for the differential equations that govern the diffusion of lithium into the electrodes. This approach often leads to good agreement with the experimental data at low C-rates. However, the extent to which the model agrees with the experiments at high C-rates depends directly on the degree of the polynomial used. Accurate prediction of high C-rate behavior demands the use of higher order polynomials, which often result in estimating a large number of unknown polynomial coefficients [83], [85].

Some studies consider a “reduced-order” model that tries to replace the analytical solutions with approximation techniques like Padé approximations [4], [76], [86], [87]. These techniques are often useful when developing models to be used in a battery management system (BMS) where, often, some level of detail needs to be sacrificed in order to decrease the computational complexity and solution time. The latter is crucial for a BMS that may need to analyze the batteries in a pack at high frequencies for real-time estimations of range and battery health.

2.4 Summary

While lithium ion batteries are becoming one of the most important energy storage technologies for the future, they still face challenges in areas including capacity and power fade. The previous sections have reviewed some of the most important battery degradation mechanisms, the effects of the operational conditions including temperature and cycling rates as well as models used to analyze, and understand the physical processes and mechanisms that affect the battery degradation. This work aims to use experimental and analytical techniques to improve our understanding of the degradation of commercial power batteries. Further, we identify the dominant capacity fade mechanisms for the specific commercial cells used in this study and for similar lab-scale cells, thus contributing to an improved understanding of the lithium ion battery, and its durability in automotive applications.

Chapter 3 - Experimental Methods

3.1 Overview of Experimental Analysis Techniques

The mechanisms leading to battery degradation can be evaluated by either non-destructive tests or destructive post-mortem tests. Non-destructive tests are done periodically during the cycling to evaluate how the batteries degrade with cycling, and to monitor the health of the batteries. Non-destructive testing can provide information to evaluate the loss of battery capacity and changes to the battery impedance. These non-destructive tests also provide data that can, with post-processing, be interpreted to identify degradation mechanism(s). Some examples of non-destructive tests include capacity and power monitoring, electrochemical impedance spectroscopy (EIS), current interrupt tests, temperature and stress monitoring, differential voltage analysis and incremental capacity analysis.

Post-mortem tests involve dismantling the cycled batteries and obtaining materials for further analysis. These tests by their nature, involve destroying cells, which will then be unavailable for continued testing. The use of destructive testing methods is better suited for smaller lab-scale cells that can be assembled and disassembled with relative ease compared to commercial scale batteries. However, these types of destructive tests can provide information on the contribution of individual electrodes to the capacity degradation or impedance change, without involving complex post-processing of data or reliance on battery models. Post mortem tests can also provide detailed information on the physical and chemical changes happening in the battery due to cycling. Some examples of these destructive techniques include electrochemical testing of half-cells, pore size and surface area analysis, X-ray diffraction studies (XRD), scanning electron microscopy (SEM) and X-ray photoelectron spectroscopy (XPS) analysis of cycled electrodes. The present work focuses primarily on non-destructive tests, which can be conducted periodically without the need to remove the batteries from the cycling protocol. These techniques are reviewed in the following sections along with selected destructive techniques that are employed in this work.

3.1.1 Capacity and Power Monitoring

The straightforward, non-destructive method of tracking changes to the battery due to cycle ageing or calendar ageing is to conduct tests that monitor the capacity and power capability. Usually, these tests are conducted at regular intervals as a part of the test protocol and are often called reference performance tests (RPTs). Capacity tests are useful in keeping track of the amount of energy available from the battery as it ages. These tests are also usually indicative of the severity of the

degradation campaign. Usually a severe ageing method results in a larger change in the observed capacity. Capacity tests are usually conducted at relatively low currents or C-rates (compared to the capability of the battery) in order to neglect any losses associated with resistance, concentration overpotentials etc. and provide a true measure of the capacity of the battery. Tests that subject the battery to high current discharge (or charge) can be used to assess the battery discharge (or charge) power capability. Periodic tests that monitor power capability enable the tracking of the performance as well as certain changes to the electrodes that can occur as the battery ages. The power capability of a battery is usually closely related to the cell resistance and any loss in the power indicates increased cell resistance. This increased cell resistance can often be attributable to side reactions that consume cyclable lithium and deposit the reaction products on to the electrode surfaces. The power capability of the battery is also dependent on the state of charge and thus, these power tests have to be conducted using carefully prescribed protocols.

3.1.2 Electrochemical Impedance Spectroscopy Studies

Details about the capacity fade mechanisms can be elucidated with electrochemical impedance spectroscopy (EIS), which subject the cell to a sinusoidal voltage (or current) perturbation over a range of frequencies and measure the current or voltage response. In the simplest application, the response at high frequency yields the cell resistance, which may be affected by interfacial changes like deposits from lithium-consuming side reactions that limit electron or ion transport [88]. EIS is frequently used to identify the change in impedance of the battery due to cycling, calendar ageing, SOC differentials and temperature changes [89]. EIS conducted on fresh and aged samples from 18650-cells (lithium cobalt oxide) has been used to identify the positive electrode as the major contributor to impedance rise and thus power fade. These studies showed increasing charge transfer resistance at the positive electrode with cycling [51], [90], and [91]. The variation of the response with frequency can also be used to ascertain losses related to electrochemical kinetics. EIS data additionally can be used for constructing equivalent circuits to identify and study specific capacity fade mechanisms [51], [88], [90], and [92].

3.1.3 External Monitoring – Temperature and Stress

In the literature review chapter, the effects of temperature on capacity fade, battery safety and the need for thermal management of the battery pack were discussed. Monitoring of the battery surface temperature by attaching thermocouples is the simplest and most straightforward method, but the use of heat flux sensors to measure the heat transfer from the surface of the cell can also yield

useful information. Having the temperature data for all the batteries in a pack allows for the analysis of the effect of temperature on the battery degradation mechanism, and provides insights into the thermal energy distribution in the pack. This information can support the design of the thermal management system and identify anomalous behavior in the battery pack [93]. Temperature measurements have also been used to analyze the use of phase change materials as possible heat sinks in battery packs [94].

In addition to the temperature measurements, monitoring the volume change of the cell by instrumenting a restraining fixture can identify structural changes in the electrode materials by directly comparing the volume of the cell to the state of charge. The cyclic lithium insertion and removal process eventually leads to a permanent increase in the electrode volume, and these structural changes in the electrodes can lead to significant loss of cyclable lithium and increased capacity fade [95]. The volume change in the electrodes can affect other parts of the battery as well. For example, pore closures have been identified in the separator material due to stress experienced during the volume change of the electrodes [96]. Analysis of the separator after cycling showed that mechanical deformations and viscoelastic creep were the leading causes of pore closures. The loss of pores directly affects the charge and discharge rates of the battery by lowering diffusion rates of lithium ions through the separator. In the present work, battery surface temperatures are monitored. The cell volume is held constant by restraints but no attempt is made to measure the resulting stress.

3.1.4 Half-Cell Studies

The characteristics of individual electrodes can be investigated by dismantling the cell and preparing smaller electrodes from the cycled electrodes. These cells, often called “half-cells” are then subjected to capacity and rate measurement tests as well as diagnostic techniques like EIS, SEM, and XPS etc. Results can provide insight into the origin and significance of degradation at each electrode and help de-convolute compound effects usually found in other analysis techniques such as differential voltage and incremental capacity analysis of full cells. For example, a study using the half-cell approach concluded that for $LiFePO_4$ batteries, the structural changes for both electrodes and the loss of active material is small, and the capacity fade is primarily attributable to the loss of cyclable lithium due to side reactions with the electrolyte [97], [98]. In another project, half-cell studies of $LiCoO_2$ electrodes, along with diagnostic tests like EIS and SEM identified

charge transfer resistance to be the cause of the impedance rise in the positive electrode and the subsequent reduction in cell power [90]. Half-cell tests have also shown that the positive electrode degradation contributes more to the overall degradation at elevated temperatures whereas at lower temperatures, the negative electrode is the more significant contributor [99].

3.1.5 Microscopy and Spectroscopy methods

Various microscopy and spectroscopy methods can provide useful information when studying the degradation in the lithium ion battery or when evaluating new materials for better performing batteries. Some common techniques include SEM, XPS, XRD, etc. SEM stands for scanning electron microscope and it enables the imaging of materials at the nano-scale. This is a useful technique when trying to study changes occurring in the electrode surface. SEM studies were shown to be effective in studying cathode materials synthesized from various inorganic salts. This study was able to identify particle agglomeration and secondary particle formation only for electrode materials synthesized from salts with the nitrate anion [100]. SEM was also used to study the surface of a composite graphite anode material [101]. The SEM images showed the presence of micro-cracks in the surface of the composite material with possible filling of the cracks by reaction products. XPS, which stands for X-ray photoelectron spectroscopy, can be used for identifying the presence of various chemical compounds. XPS has been successfully used in order to identify the composition of the SEI [23]. This technique revealed the presence of compounds containing the C_2H, $C_2H_3O_2$, C_2H_3O and other C_xH_y hydrocarbon groups. XPS was also used to study the degradation in electrolyte solvents when used with higher voltage cathodes needed for high power batteries [102]. At higher voltages (4.5 - 5.3 V vs. Li/Li^+), the organic solvents used in the electrolyte solution were shown to polymerize and thus degrade.

3.2 Commercial Cell Testing

One of the primary research goals of this work is to assess the impact of the cycle profile on battery durability. This goal was pursued by subjecting a set of commercial batteries to two distinct cycle profiles over an extended period while conducting periodic performance tests. The resulting data provides a direct assessment of the relative effects of the two profiles on durability. Additionally, the data gathered from these tests can be used to support additional analytical methods to help identify the source of the observed degradation. The batteries used in this study, as shown in Figure 5, are commercial power cells with graphite as the intercalation material for the negative electrode

and $LiNiMnCoO_2$ (NMC) for the positive electrode. The nominal beginning of life capacity of the batteries was 5 Ah and thus the 1C-rate is 5 A. These batteries operate within a voltage range of

Figure 5: Batteries assembled into two test packs

2.5 – 4.1 V and are capable of discharge rates of up to 48C (240 A) and charge rates of up to 36C (180 A). The batteries were housed in a test chamber during the testing period. The air temperature in the chamber was maintained at 30 °C ± 2 °C and the individual battery temperatures were monitored. The cutoff limit for the battery surface temperature during cycling was 50 °C.

3.2.1 Cycling Tests

The fundamental purpose of this work is to identify the effect of cycle profile on battery degradation. In order to accomplish this, two battery packs containing eleven batteries each in series were assembled (the number of cells in each pack was limited by the voltage limit of the battery cycler). These packs were then subjected to two very different profiles called the "Pulse" and "Square" profiles. The pulse profile is representative of an aggressive drive cycle while the square profile simply alternates between constant current charge and discharge. The square profile is designed to achieve the same RMS current as the pulse profile and hence the same amount of charge transfer over the entire cycle; but the current and peak voltages encountered by the batteries using these two profiles are very different. The net charge transfer during testing is zero for both profiles and this maintains a constant SOC during the test phase. For the baseline case, the battery packs were maintained at 40 percent SOC to remain within the voltage limits recommended by the manufacturer.

Figure 6a shows the pulse profile current for the battery pack, and Figure 6b shows the corresponding voltage response from a single battery in the pack. The pulse profile, used to simulate on-road conditions is based on data derived from tests conducted on a charge sustaining

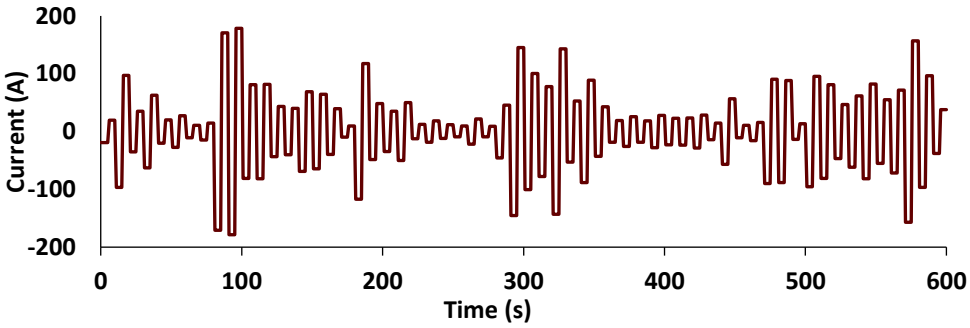

a: Current – pulse profile

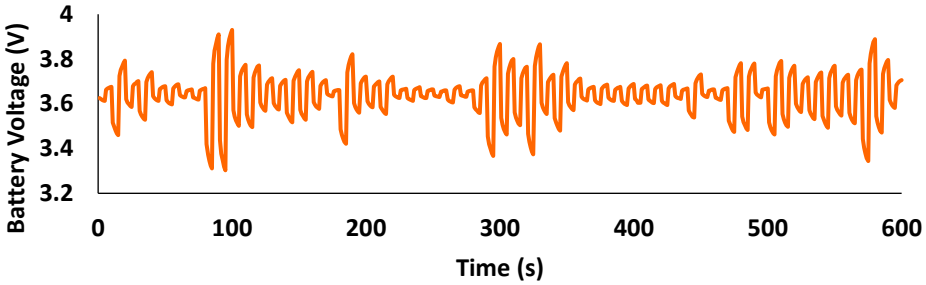

b: Voltage response – pulse profile

Figure 6: Pulse profile current and voltage response

electrified vehicle executing the US06 drive cycle [103]. This profile has a peak current of 36C (180 A) and root mean square (RMS) current of 14C (70 A).

The square profile shown in Figure 7a is a simple square wave signal with a magnitude of 14C (70 A). The square profile provides the same charge throughput as the pulse profile but does so with much lower peak current (70 A versus 180A) and a much smaller voltage differential (±0.24 V versus ± 0.63 V). This sharp contrast between the two profiles should help draw clear conclusions on whether the cycle profile really does have an effect on the degradation of batteries.

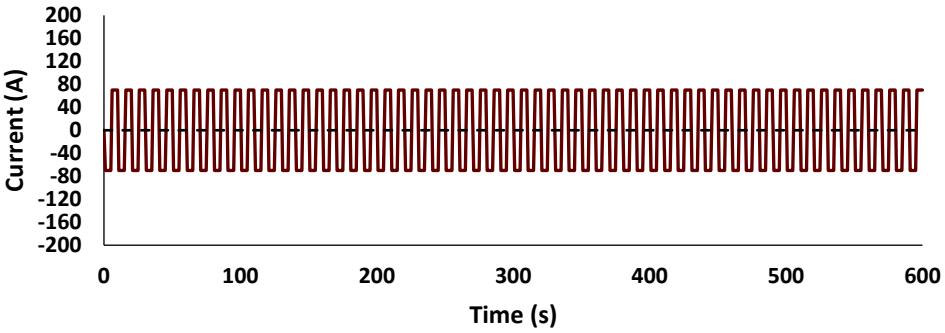

Figure a: Current – Square Profile

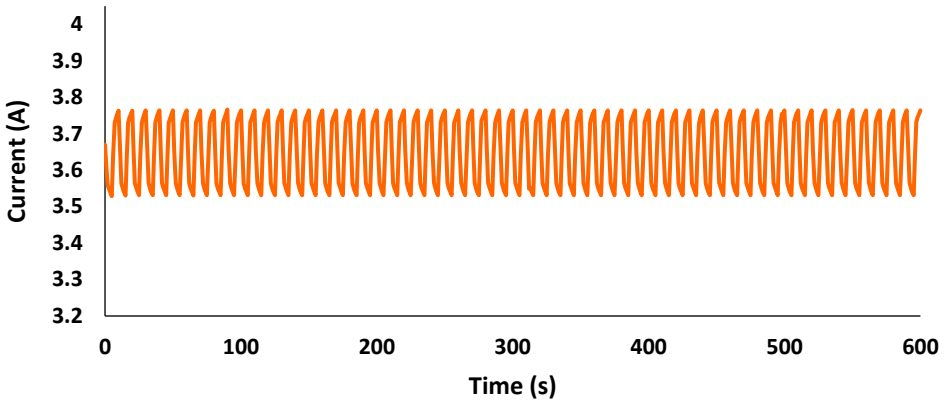

Figure b: Voltage response – Square Profile

Figure 7: Square profile current and voltage response

Key characteristics of the baseline pulse profile case (Figure 6) include the operating voltage window of 3.33 V – 3.94 V and the maximum SOC differential of 4.96 percent. To assess the influence of these characteristics on durability, additional cycling tests were designed. For these additional cycling tests, four batteries from each of the original packs were removed after 40 kAh to test how the capacity and power fade change under different cycling conditions. These new conditions include first, cycling the batteries using the same profiles at a higher SOC thus raising the voltage window in which the batteries operate. This is illustrated in Figure 8 and Figure 9, which show the voltage response to an increased SOC (60 percent) during cycling for the pulse profile and the square profile respectively (60 percent SOC was used to remain within voltage limits with same current levels). In these figures, the dashed black lines indicate the upward shift in the rest voltage of the battery.

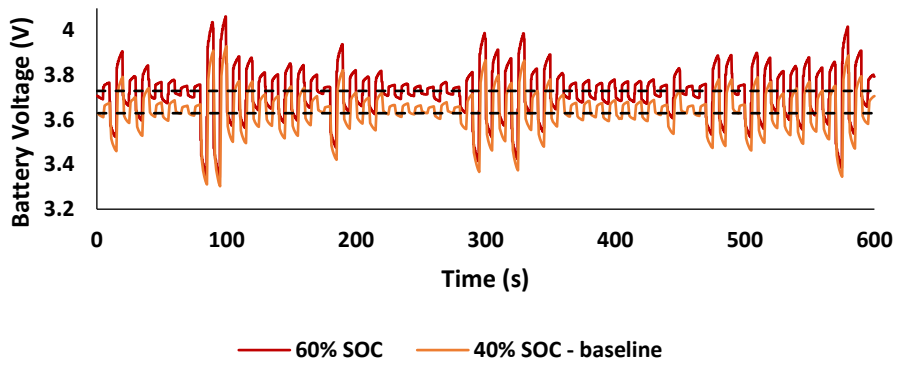

Figure 8: Voltage response – pulse profile at 60 and 40 percent SOC

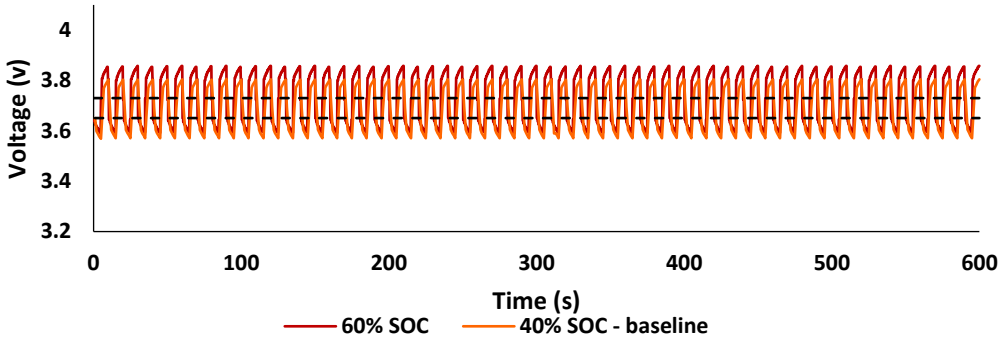

Figure 9: Voltage response – square profile at 60 and 40 percent SOC

The second condition is the cycling of batteries at the same midpoint SOC as the baseline condition (i.e. at 40 percent) but with the charge and discharge pulses doubled in duration to effectively increase the SOC differential. The maximum SOC differential for the pulse profile goes up from 4.96 percent (in the baseline tests) to 11 percent and the SOC differential for the square profile goes up from 1.94 percent (in the baseline tests) to 4.32 percent. The voltage response to the new test conditions is shown in Figure 10. It can be observed that the cycle time has doubled from 600 seconds to 1200 seconds and the voltage response of the batteries implies a larger SOC differential compared to Figure 6 or Figure 7. The dashed black lines here indicate the maximum and minimum voltage achieved with the pulse profile in the baseline case. The voltage windows and the SOC differentials for the batteries cycled with the three before mentioned cases are given in Table 2.

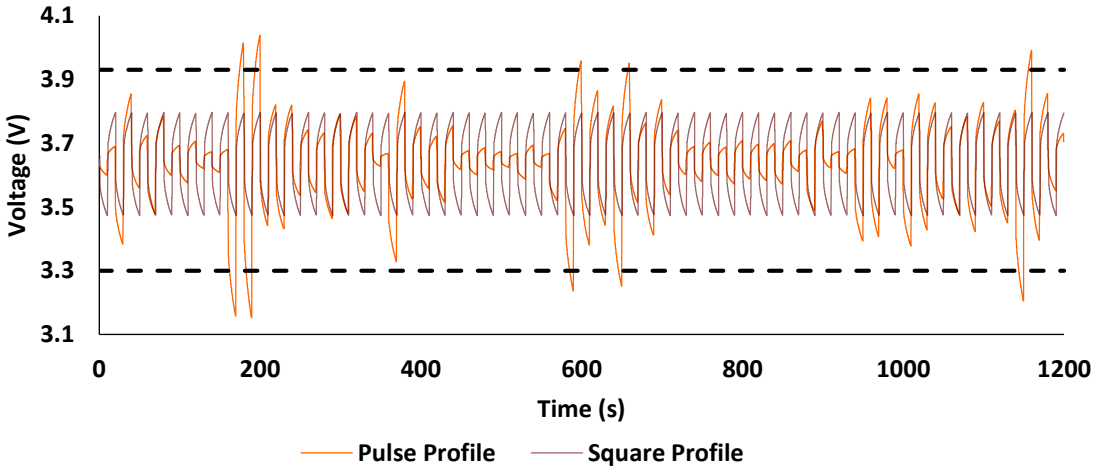

Figure 10: Voltage response – square and pulse profile with increased SOC differential

Table 2: Operational parameters for batteries tested with the three cases

Case	Voltage window		Maximum SOC differential	
	Pulse	Square	Pulse	Square
Baseline, cycling at 40% SOC	3.31 V – 3.94 V	3.53 V – 3.77 V	± 4.96 %	± 1.46 %
Case 1, base SOC at 60%	3.34 V – 4.06 V	3.60 V – 3.86 V	± 4.96 %	± 1.46 %
Case 2, increased SOC differential	3.10 V – 4.05 V	3.46 V – 3.79 V	± 11.0 %	± 4.32 %

3.2.2 Reference Performance Tests (RPT)

In order to establish a relationship between the voltage, age, and capacity of the battery, reference performance tests (RPTs) were performed at regular intervals during the cycling of the batteries. Reference performance tests were conducted every 10 kAh until 40kAh of cycling. From 40 kAh of cycling until end of testing (100 kAh), the reference tests were performed every 20 kAh. This 10 kAh is a cumulative throughput consisting of both charge and discharge cycles. The RPT incorporates two separate tests – a capacity measurement test and a power capability test.

The capacity measurement test begins with a standard constant current – constant voltage (CC-CV) charge process as shown in Figure 11. During the CC-CV charge process, the battery is first charged at a constant 1C-rate (5 A). Once the battery reaches the maximum permissible voltage (4.1 V), the constant current charging is stopped. The battery voltage is then held constant at this maximum value and charging is continued until the current drops to a set value (usually a C/20 or

C/25 rate). This CC-CV method ensures that the battery is charged completely to its maximum capacity. The charge process is followed by a rest period of 30 minutes to stabilize the battery. Then, a constant current discharge process is executed at the 1C-rate until the battery reaches the minimum permissible voltage. This test allows the measurement of the charge and discharge capacity of the battery and is repeated periodically to track changes to the capacity over the course of testing.

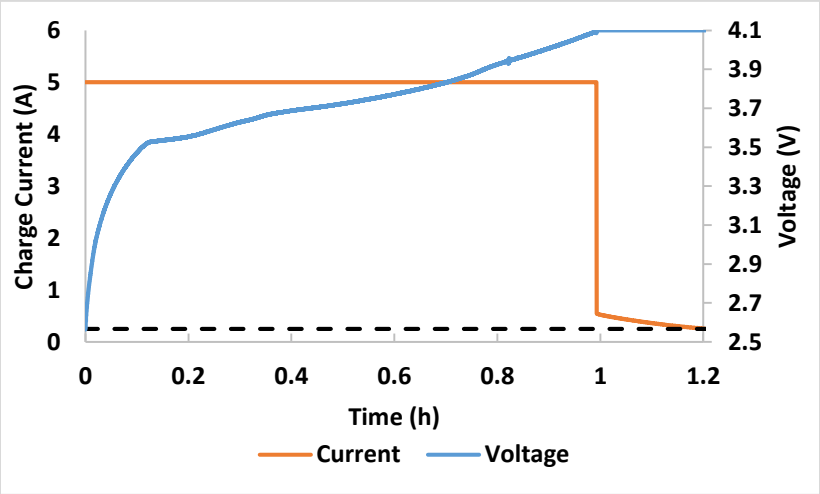

Figure 11: CC-CV charge profile at 1C-rate

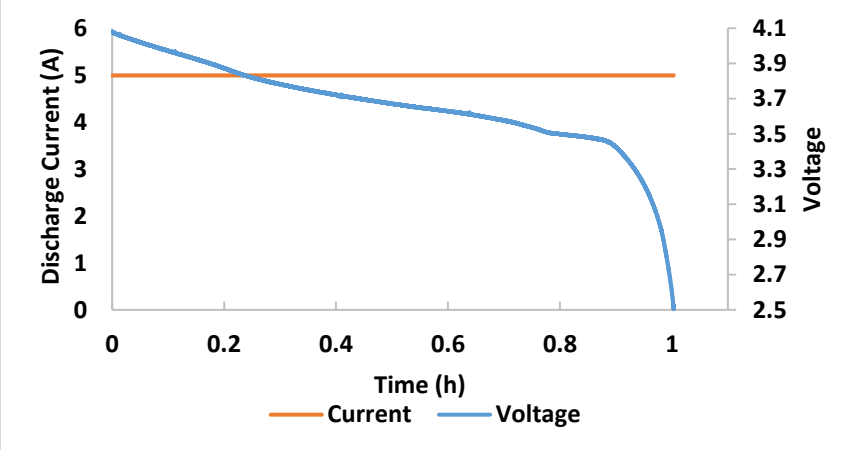

Figure 12: Constant current discharge at 1C-rate

The second test in the RPT is the pulse power test, also known as the Hybrid Pulse Power Capability (HPPC) test. The specific test employed in this work is based on the HPPC-L test described in the 2003 version of the FreedomCar manual [64]. The standard test consists of a 10-

second discharge pulse at a rate of 5C or at a rate of 25 percent of the maximum discharge rate, I_{max}, whichever is greater. The discharge is followed by a 40-second rest period and then a 10-second charge pulse at 75 percent of the discharge current, bringing the total cycle time to one minute. This profile is shown in Figure 13. In the standard test, this procedure is repeated across a series of battery SOC values from 90 percent to 10 percent (in 10 percent increments) with a rest period of 60 minutes between each SOC value. In this work, the standard HPPC-L test was modified to increase the discharge current to 40 percent of I_{max} while the charge current remained 75 percent of the discharge current or 30 percent of I_{max}[3]. In addition, the tests were conducted only at 80, 50, and 20 percent SOC. These three SOCs were chosen to be representative of a high (80 percent), nominal (50 percent), and low (20 percent) SOC in a battery. These SOCs also ensure limiting voltages are not reached during the test. The modified HPPC test was conducted at ambient temperature.

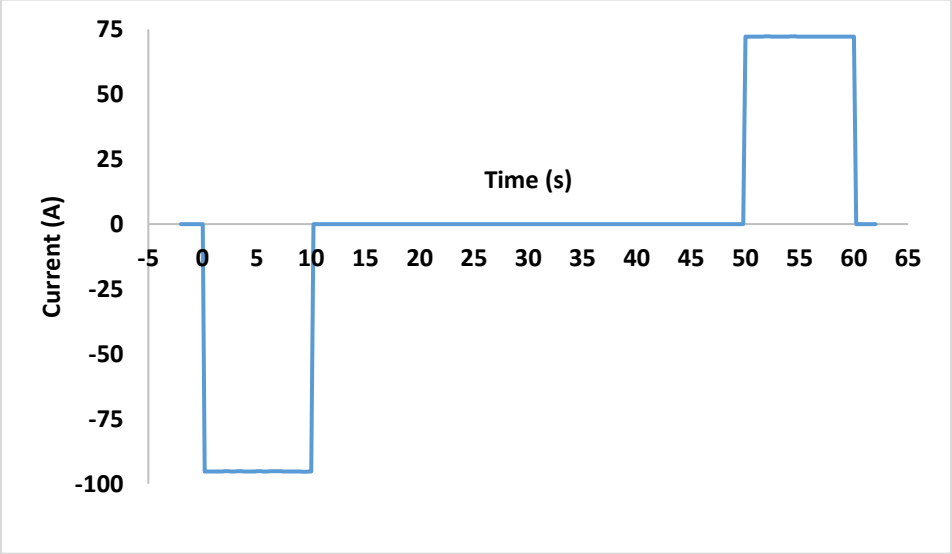

Figure 13: HPPC current pulse

In the modified HPPC test as shown in Figure 14, the battery is initially fully charged using the CC-CV method described previously followed by discharge to the first test SOC followed by a rest period of 30 minutes. Once this rest period is complete, the pulse test is done, followed by another 30-minute rest period after which, the battery is discharged to the next SOC. This

[3] I_{max} for the batteries under consideration is 240 A, making the HPPC discharge current 96 A and the charge current 72 A

procedure is conducted three times during the modified HPPC test. The data obtained from the HPPC tests was used in the PNGV model [64] to obtain the internal resistance of the batteries. Like the capacity test, the HPPC test was also performed periodically to track changes in the power capability and internal resistance of the battery.

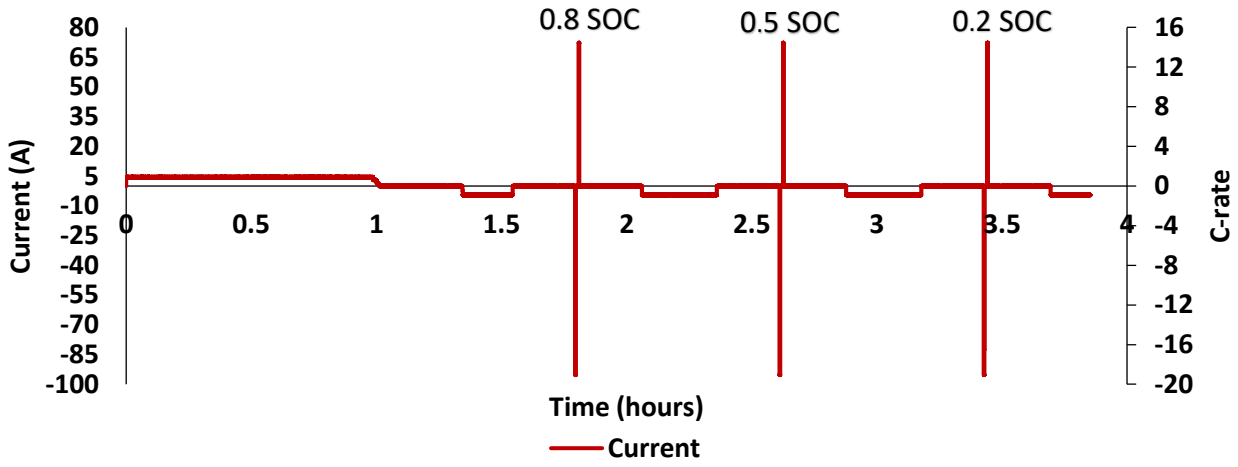

Figure 14: Modified HPPC test current profile

3.3 Coin Cells

In addition to the study of degradation in commercial cells, it is of interest to identify whether degradation in lab-scale coin cells is similar compared to commercial cells. The use of coin cells also provides capabilities not available with the commercial cells. For example, using coin cells it is possible to conduct post mortem studies and independently assess anode and cathode materials relative to a common lithium reference electrode. The coin cells also have fewer safety concerns compared to commercial cells and can be cycled continuously without constant supervision. Finally, the use of coin cells provides control over the physical properties of the coin cell components. For example, electrode thickness, current collector area etc. that were unknown for the commercial cells and that had to be estimated either from battery behavior or literature are now determined by direct measurement or selected as part of the coin cell design. Better knowledge of the coin cell components facilitates the validation of a mathematical model, which can be used for the study of battery degradation. In order to study the degradation in lab-scale cells due to cycling, coin cells (CR 2032) were fabricated and tested. The components required for the coin cells were purchased from MTI Corporation, the details of the components are given in Table 3.

Table 3: Properties of components used in coin cell fabrication

Parameter	Unit	Positive Electrode	Negative Electrode
Electrode Thickness	μm	45	40
Current collector material	-	Aluminum	Copper
Material theoretical capacity	mAh/g	155	330
Electrode disk diameter	cm	1.11	1.43
Active material mass fraction	-	0.942	0.957
Average electrode mass	mg	17.5	21.13
Current collector thickness	μm	15	9
Mass of active material	mg	12.78	7.85
Electrode theoretical capacity	mAh	1.98	2.6
Manufacturer	-	MTI Crop.	MTI Corp.
Model number	-	bc-af-241NCM-ss523	bc-cf-241-ss-005
Electrolyte – 1M $LiPF_6$ in 1:1 EC:DMC, manufacturer Sigma-Aldrich Separator – 1.9 cm diameter disk, 25 μm thick, manufacturer – Celgard LLC			

3.3.1 Coin Cell Fabrication

Lithium ion batteries can be adversely affected by the presence of oxygen or moisture on the electrodes. For example, even trace amounts of water can combine with the $LiPF_6$ salt and form HF, which is extremely corrosive. Thus, it is imperative that the components used in the assembly of the coin cells are free of any surface moisture and oxygen. All components used in the assembly of the batteries were stored in an inert argon atmosphere glovebox. During the fabrication of the cells, the electrode sheets were briefly exposed to the atmosphere while punching out electrode discs (using a hydraulic press). In order to remove any surface moisture and oxygen that may have adhered during this process, the electrode discs were dried in a vacuum oven at 110 °C for 3-4 hours. The dried electrodes were then immediately transferred to the glovebox for assembly. The separator material, commercially referred to as Celgard, is a polymer that shrinks when exposed to temperatures above 60 °C. Therefore, separator disks were held under vacuum without exposure to a heat source in order to remove any surface moisture. The dried separator discs were then

soaked in the electrolyte solution and held under slight vacuum to remove any gases trapped in the polymer. The coin cells were then assembled inside a glove box in the order given in Figure 15, starting from the negative case and ending with the positive case. Once all the components were assembled in the correct order, a hydraulic crimper was used to compress (4900 kPa) and seal the components inside the cell. The assembled coin cells were then transferred out of the glove box and rested for 6 – 8 hours (to let the electrolyte redistribute inside the cell) prior to the formation cycles. During all phases of the assembly process, plastic tipped instruments were used to handle all components to prevent any accidental short circuits. Despite all the precautions taken in order to avoid coin cells of poor quality, the assembly process resulted in variabilities between the capacities of the cells. Close to 250 individual coin cells were made during the course of this study (excluding half-cells made from tested cells). Out of which, one third of the cells failed even before the start of the formation cycles due to internal short circuits and registered cell voltages in the order of a few microvolts. A third of the cells were rejected due to failing to cycle between voltage limits during the formation cycles. Finally, twenty cells with similar capacities were chosen for cycling from the cells that worked past the formation stages. The chances of a working coin cell was one in three and of those cells that worked past the formation cycles, only 40 percent shoed similar capacities. This low success rate underscores the difficulties in the cell assembly and fabrication processes at the laboratory scale.

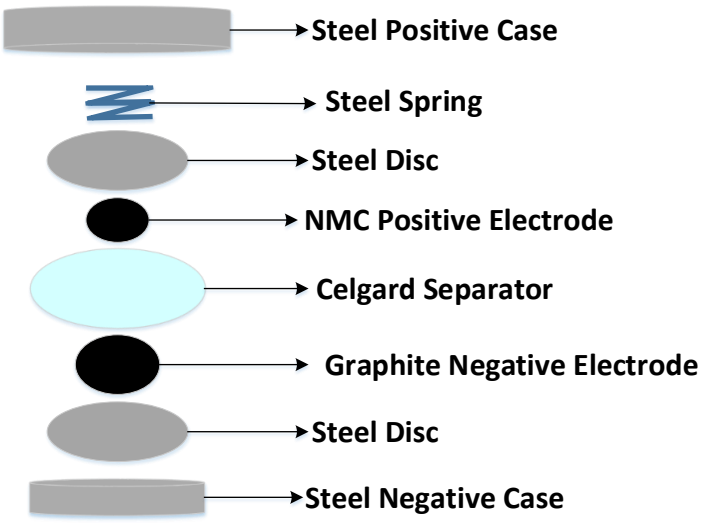

Figure 15: location of parts in the coin cell

3.3.2 Formation cycles

All lithium ion batteries have a passivating SEI layer on the negative electrode[4]. The SEI layer is usually formed during the first few charge-discharge cycles due to deposition of reaction products formed during the reaction between cyclable lithium and electrolyte solvents. The thickness, uniformity and structure of the SEI layer depend on the current used to cycle the battery during these formation cycles. Usually, a rate of C/10 or smaller is used during the formation process to achieve a SEI layer with optimum properties. The low rate ensures that the reaction products deposit uniformly over the negative electrode surface and inhibits the formation of any dendrite like structures.

The maximum theoretical capacity of a coin cell made from the components described in Table 3 is approximately 2.0 mAh. However, the initial SEI formation cycles result in an irreversible loss of lithium due to side reactions and the coin cells exhibit lower capacities. In order to perform the formation cycles, the rested cells were subjected to the charge-discharge cycles using a current of 0.2 mA (~ C/10) within a voltage range of 4.1 – 2.5 V until no negligible drop in the battery capacity was observed between cycles (typically 3 to 5 cycles). A typical coin-cell discharge curve is given in Figure 16.

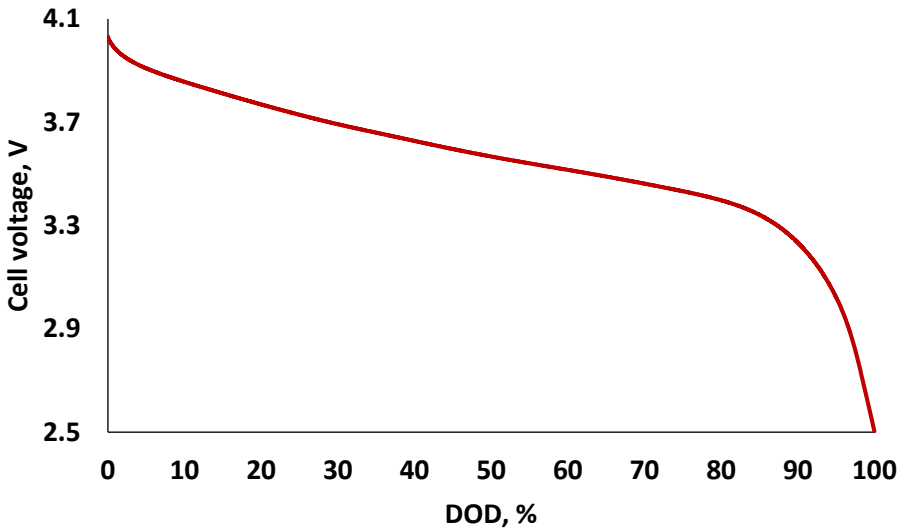

Figure 16: Coin cell discharge curve

[4] The details of SEI formation and the function of the SEI is discussed in Chapter 2

3.3.3 Cycling tests

The lab-scale coin cells are not expected to have the same rate capability as the commercial cells. Thus, scaled versions (based on the C-rate) of the profiles used to cycle commercial cells are not viable for cycling coin cells. Instead, cycle profiles that reflect the lower C-rate capability of the coin cells were developed. During the development of the coin cell specific profiles, key features of the voltage response of the commercial cells to cycling (Figure 6b and Figure 7b) were studied. All commercial cells subjected to the square profile experienced voltages less than 3.8 V during the 100 kAh of charge transfer. In contrast, commercial cells subjected to the pulse profile experienced voltages in excess of 3.8 V for eight percent of each cycle duration. While the cells subjected to the pulse cycle also experienced even higher voltages, the accumulated duration at these higher voltages was less than eight percent. Thus, we chose 3.8 V as representative of the higher (possibly damaging) voltages associated with the pulse-heavy driving cycle. The coin cell specific profiles were then developed based on time spent above 3.8 V. Specifically, we developed four cycles to study the effect of time spent above 3.8 V.

The four profiles study the effect of cycling the coin cells for 0 %, 10 %, 15 %, and 20 % time above 3.8 V respectively. A simple square-wave with a C-rate rate of C/2 spent zero percent of the time above 3.8 V and was chosen as the baseline case. The other three profiles that subject the battery to voltages greater than 3.8 V, also have the same duration as the base case and each is a combination of two separate square-wave profiles. The first part, with a C-rate of 1.5, ensures that the batteries spend time above 3.8 V. the duration the first part depends on the amount of time to be spent above 3.8 V. The second part that constitutes the remainder of the profile, subjects the battery to a square wave with a rate that ensures the same overall charge throughput as the base case. The duration and respective C-rates for these three profiles are given in Table 4 and, all four profiles are illustrated in Figure 17.

Table 4: C-rates and profile durations used for coin cell cycling

time above 3.8 V, (%), s	Total profile duration (s)	High current rate	Low current rate
(0), 0	600	C/1.5	C/1.5
(10), 60	600	1.5C	C/2.60
(15), 90	600	1.5C	C/3.22

(20), 120	600	1.5C	C/6.25

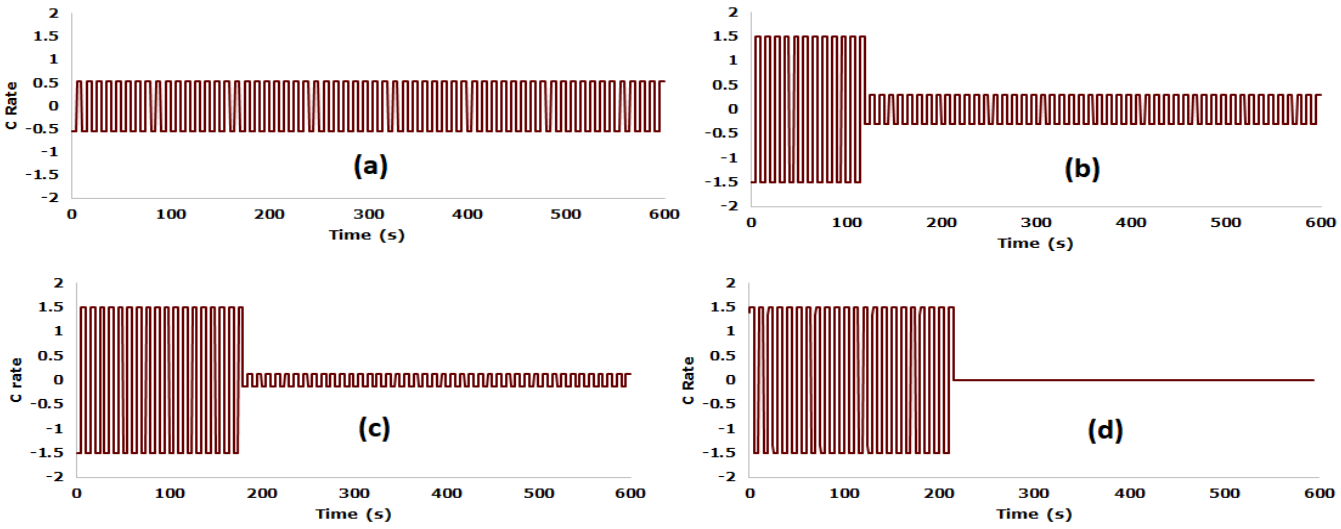

Figure 17: Profiles used study effect of cycle profile on coin cells (a) 0 %, (b) 10 %, (c) 15 % and (d) 20 % pulse time spent above 3.8 V

3.3.4 Coin Cells Subjected to High Voltage without Cycling

In order to isolate the effects of high voltage from the effects of cycling, four coin cells were maintained at voltages in excess of 3.8 V without cycling over a period of thirty days while other coin cells underwent cycling tests. These cells were monitored routinely to ensure that the voltage did not fall below 3.8 V due to self-discharge. RPT tests were conducted once every two days in order to keep track of changes to the capacity and resistance.

3.4 Hardware

3.4.1 Hardware Used for Commercial Cell Testing

The current profiles used for the testing of the battery packs were generated and administered by two heavy duty battery cyclers capable of 500 A at 48 V (DC) made by Bitrode Corporation USA shown in Figure 18.

Figure 18: Bitrode battery cycler

The voltage, temperature and current were measured using a supervisory system built from National Instrument hardware whose configuration is shown in Figure 19. This system has the capability to simultaneously measure 22 voltage channels, 2 current channels, 32 temperature channels and control two relays, which are used in conjunction with the safety sub-system. The safety sub-system consists of the relays, which control high-current interrupt switches that connect the batteries to the cyclers. The logic used for the supervisory system to collect data as well as enforce the safety limits is illustrated in Figure 20. This system checks for all established safety limits before the relays engage the switches for the first time and actively enforces the safety limits, shutting down the battery testing in case any of the limits are breached. The system runs on the LabVIEW software also developed by National Instruments.

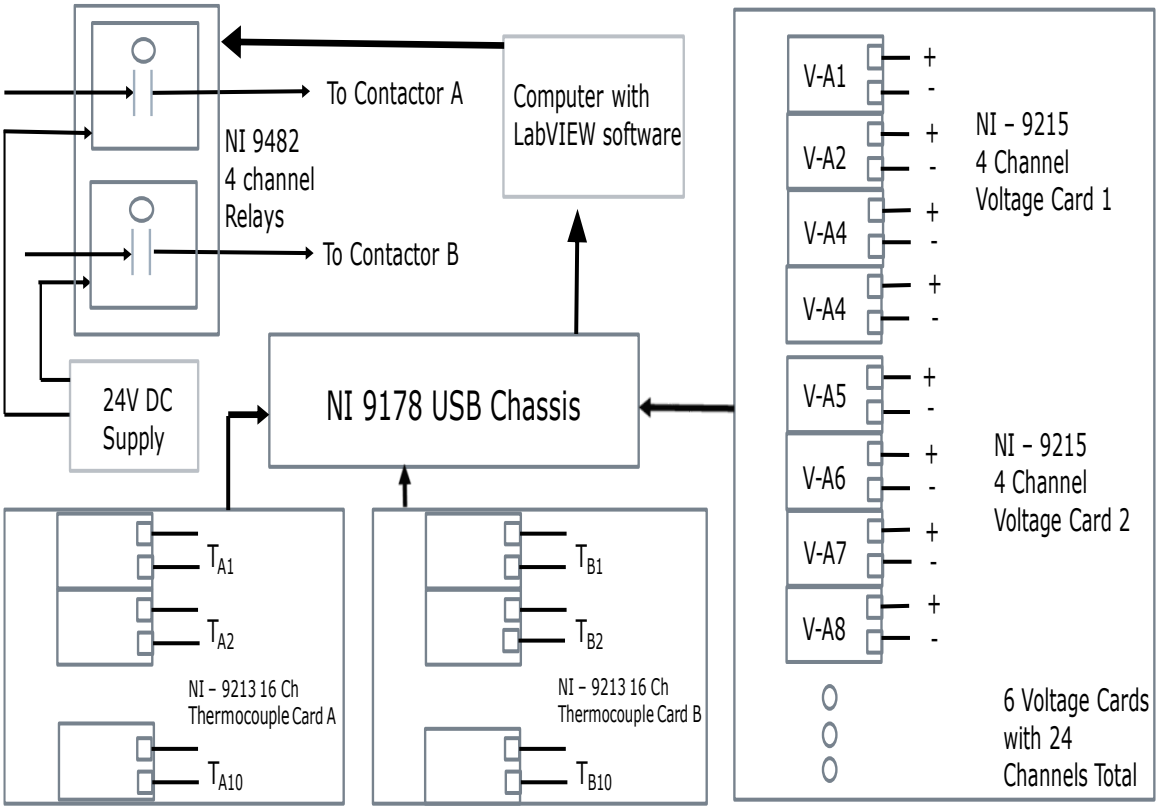

Figure 19: Supervisory system configuration

Table 5: List of safety monitors and limits for commercial cell testing

Monitored parameter	Upper limit	Lower limit
Battery surface temperature	55 °C	10 °C
Battery voltage (low C-rate conditions)	4.1 V	2.5 V
Battery voltage (high C-rate, less than 10 seconds)	4.3 V	2.45 V
External power supply to the data acquisition and supervisory system	If the system detects backup battery power use for more than 2 continuous minutes, the testing is paused, data is saved, the user is notified via email and a computer shutdown is triggered after an additional 2 minutes.	

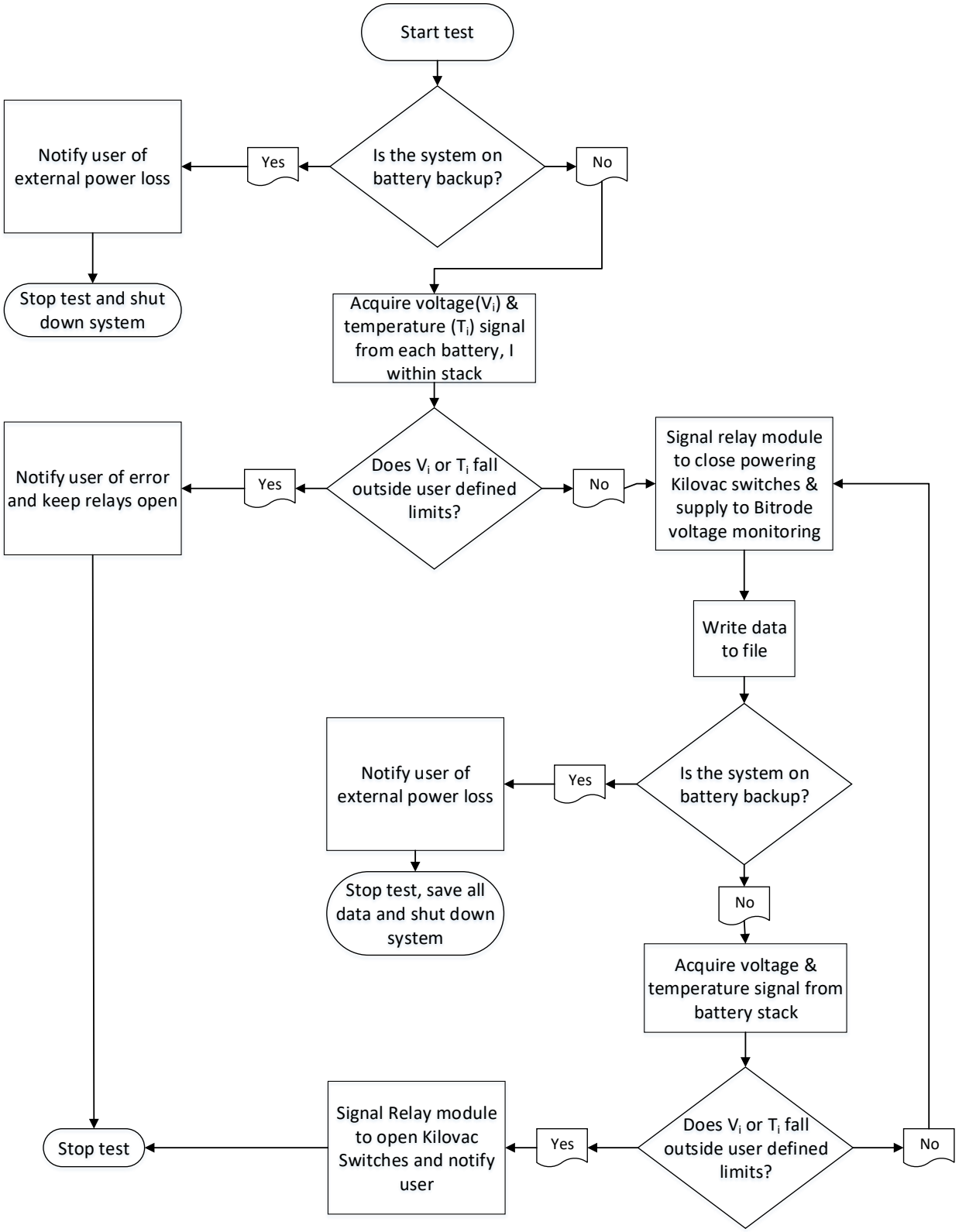

Figure 20: Supervisory system logic

3.4.2 Hardware Used for Coin Cells

The cycling of coin cells involves currents in the range of a few milliamperes and thus does not require extensive safety systems or high current battery cyclers. However, the coin cell testing needs an accurate potentiostat capable of measuring low currents. All of the cycling and testing operations for the coin cells were performed on a Solatron 1420 eight-channel potentiostat, with a built in frequency response analyzer (FRA) as shown in Figure 21, capable of measuring currents as low as 50 nA and of conducting EIS tests to identify changes in cell resistance.

Figure 21: Solatron eight-channel potentiostat used for cycling coin cells

3.5 Uncertainty Analysis

All experimental data must include an assessment of the error associated with measurement. The error in the experiment can arise from either the operator (human error) or the accuracy of the measuring instrument, which is a parameter dependent on the instruments design and manufacture. The uncertainty of an experiment is the quantification of the doubt associated with the measurement. The uncertainty is a derived quantity while the error associated with the measurement is used to derive the uncertainty of the experiment. For example, if the length of an object were to be measured with a ruler, it can be expressed as

$$length = l\,(m) \pm error(m) \tag{3.1}$$

where, the length "l" represents the true value and the error identifies the upper and lower value that can be measured based on the accuracy of the measuring instrument. This can be used to identify the uncertainty in the measurement of the length. Kline and Mclintock [104] estimated the uncertainty due to n measurements as

$$w_M = \pm\left(\sum_{1}^{n}\left(\frac{\partial M}{\partial x_n}\right)^2 w_n{}^2\right)^{\frac{1}{2}} \tag{3.2}$$

Where, M is the desired derived quantity that can be computed with 'n' individual measurements, x_n is some particular parameter being measured and w_n is the error associated with each measurement.

For example, consider the length of a cube, measured as $a \pm err$ and, M is the derived quantity volume. From basic mathematics, volume can be defined as $M = a^3$ and the uncertainty associated with the volume based on Eq. 3.2 is $[(3a^2)^2(err)^2]^{\frac{1}{2}}$

In the case of the supervisory system, the voltage of the batteries was measured using a NI 9215 analog voltage input device and the current was calculated by measuring the voltage drop across a shunt using a NI 9219 analog input device. In order to calculate the uncertainty, the accuracy of these devices must be quantified. The error in these devices is a sum of two individual errors; 1) the gain error, which is a percentage of the measurement, and; 2) an offset error that in independent of the reading and depends only on the measurement range of the devices. The accuracy values of these devices are given in Table 6. The current is measured using a shunt that has a resistance of 0.000333 Ω and the voltage drop measured across the shunt has an uncertainty of ±0.25 percentage as specified by the manufacturer.

Table 6: Error associated with voltage measurement devices

Device	Voltage Range	Gain Error (% of reading)	Offset Error (% of range)	Total Error
NI 9215	$\pm$10.4 V	0.02	0.014	Gain error + offset error
NI 9219	$\pm$125 mV	0.1	0.012	Gain error + offset error

Using Eq. (3.2), the accuracy values from Table 6, and the uncertainty associated with the precision resistor, the uncertainty in the battery capacity and the power generated during the 1C capacity test and the HPPC test respectively, can be identified. The maximum current used during the capacity tests is 5 A at BOL and the maximum current used during the HPPC test is 96 A. During the HPPC test, the voltage of the battery changes with time. However, in order to reduce computational

complexity, the maximum permissible battery voltage of 4.1 V can be considered as the working voltage for the uncertainty calculations. The voltage drop across the shunt for any current can be calculated using Ohm's law

$$V = IR \tag{3.3}$$

The resistance of the shunt in Eq. (3.3) can be given as $3.333 \times 10^{-4}\Omega \pm 8.32 \times 10^{-7}\Omega$ and the voltage measured for a current of 5 A by the NI device can be given as 1.665 mV ± 35.83 μV and the uncertainty in the current for a value of 5 A can be calculated from Eq. (3.2) as 5±0.108 A

The capacity of the battery can be calculated using the formula

$$C = It \tag{3.4}$$

Where, t is the time for which the battery experiences a current of magnitude I

Using Table 6 and Eq. (3.2), Eq. (3.3) and Eq. (3.4) the uncertainty in the capacity can be calculated as

$$w_m = \left(\left(\frac{dC}{dI}\right)^2 (0.108)^2\right)^{\frac{1}{2}} = 0.108t \tag{3.5}$$

Considering time t equals 1 hour, w_m equals $\pm$ 0.108 Ah this translates to an uncertainty of $\pm$ 2.16 percent.

$$C = 5\ Ah \pm 0.108\ Ah \tag{3.6}$$

During the HPPC test, the maximum current used is 96 A and the voltage can be considered 4.1 V for ease of computation. Using Table 6, and the shunt uncertainty, the current can be expressed as 96 A $\pm$ 0.43 A and voltage can be expressed as 4.1 V $\pm$ 0.0038 V. The uncertainty in power, which is the product of voltage and current VI, can be calculated as

$$w_m = \left(\left(\frac{\partial(VI)}{\partial I}\right)^2 (0.43)^2 + \left(\frac{\partial(VI)}{\partial V}\right)^2 (0.0038)^2\right)^{\frac{1}{2}} \tag{3.7}$$

Eq. (3.7) results in a w_m of 1.88 W, which is around half a percent of the power generated.

Chapter 4 - Analysis of Battery Degradation

In this chapter, the methods used for analyzing experimental data and predicting the performance of the battery are discussed. The analysis methods make use of the discharge profile of the battery to derive characteristic curves. The changes in these curves as the batteries age can address questions regarding the degradation mechanisms. This chapter also discusses the physics-based model used to predict the voltage response of the battery to an applied current. The development of such a physics-based model allows for a deeper understanding of the various phenomena happening in the battery. Development of a model also enables us to observe the effects of different parameters on the battery performance and degradation.

4.1 Analysis Techniques

4.1.1 Differential Voltage and Incremental Capacity Analysis

Techniques for non-destructive evaluation are particularly useful because they allow more rapid evaluation of full-scale batteries that are not designed for disassembly. The simplest technique that can be used to identify and quantify capacity fade is to cycle the batteries while conducting periodic Reference Performance Tests (RPTs)[5]. The RPTs also provide the data necessary to perform either differential voltage analysis (DVA) or incremental capacity analysis (ICA), either of which can provide information on the degradation mechanisms. Differential voltage analysis of full cells has been used to provide insight into the cause of degradation. For example, phase changes in the active material were identified using differential voltage analysis, which led to capacity fade due to a stress induced diffusion mechanism [65], [105]. This mechanism involves continuously increasing exposure of active carbon for continued SEI growth due to continuous insertion and de-insertion of lithium ions, thus, gradually increasing capacity fade due to loss of lithium. Phase changes in the active material lead to increased mechanical stresses and thus to structural damage of the electrode causing degradation.

[5] The RPTs are discussed in detail in the experimental methods chapter.

DVA or ICA can be done using data obtained from the RPTs, specifically, the 1C capacity data. These tests can be conducted on full cells to identify general capacity fade mechanisms and they can be performed on half cells assembled from cycled batteries, to identify the individual electrode contributions to the capacity fade [106], [107] [108]. Incremental capacity and differential voltage profiles from the literature and experimental test data from the present work are shown in Figure 22 through Figure 27.

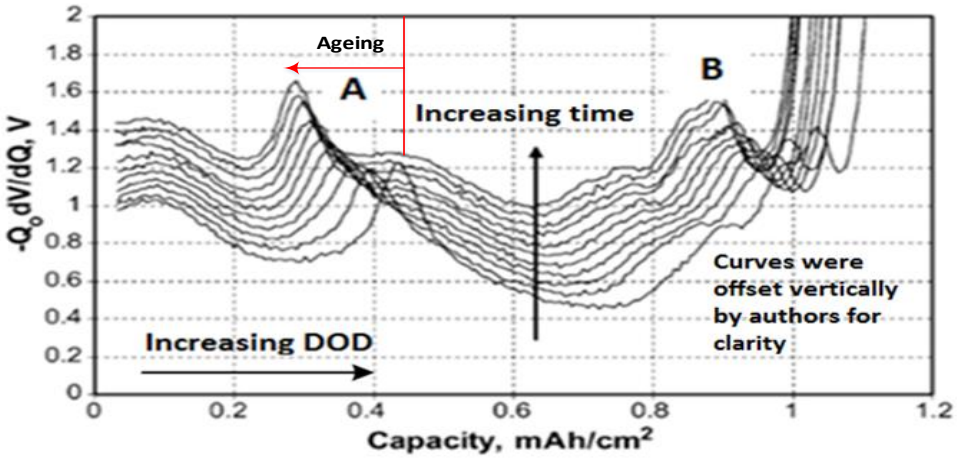

Figure 22: Differential voltage analysis plot from ref. [106] [6]

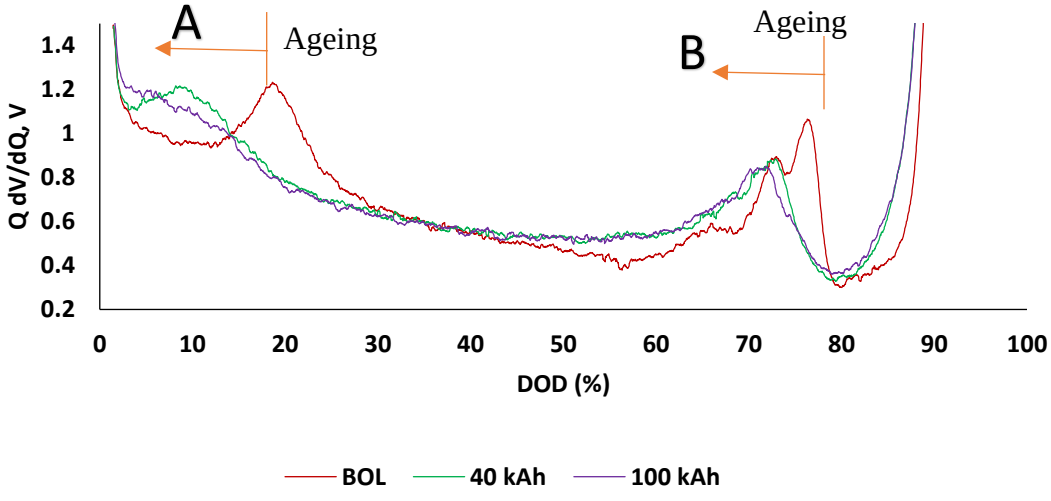

Figure 23: Differential voltage analysis for a battery cycled using the pulse profile

[6] Reprinted with permission from Elsevier, license number 4127741393697.

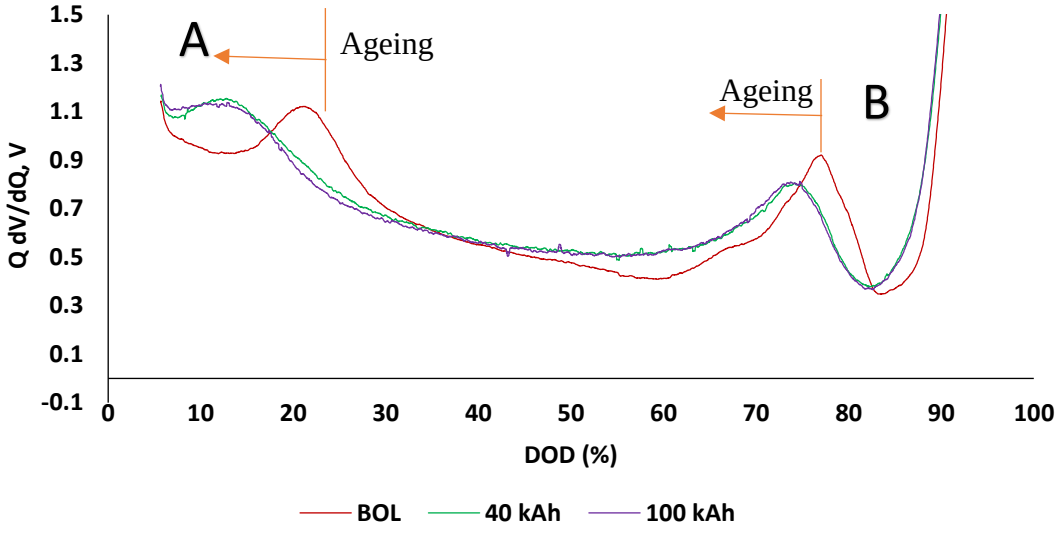

Figure 24: Differential voltage plot for a battery cycled using the square profile

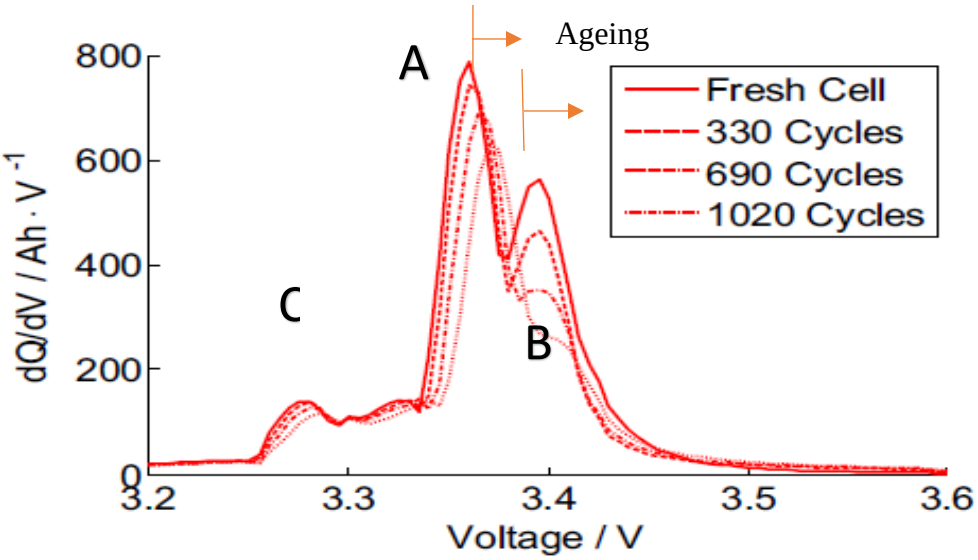

Figure 25: Incremental capacity plot from Ref. [68] [7]

[7] Reprinted with permission from Elsevier, license number 4127831045894.

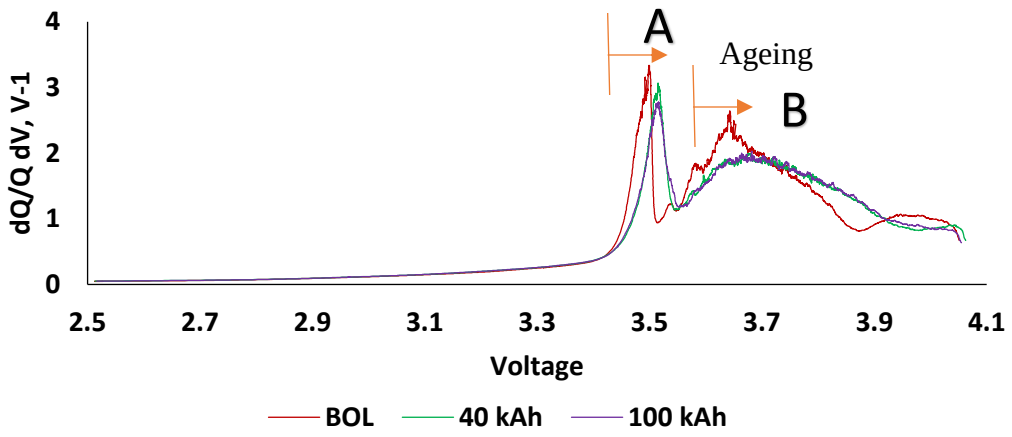

Figure 26: Incremental capacity plot for a battery cycled using the pulse profile

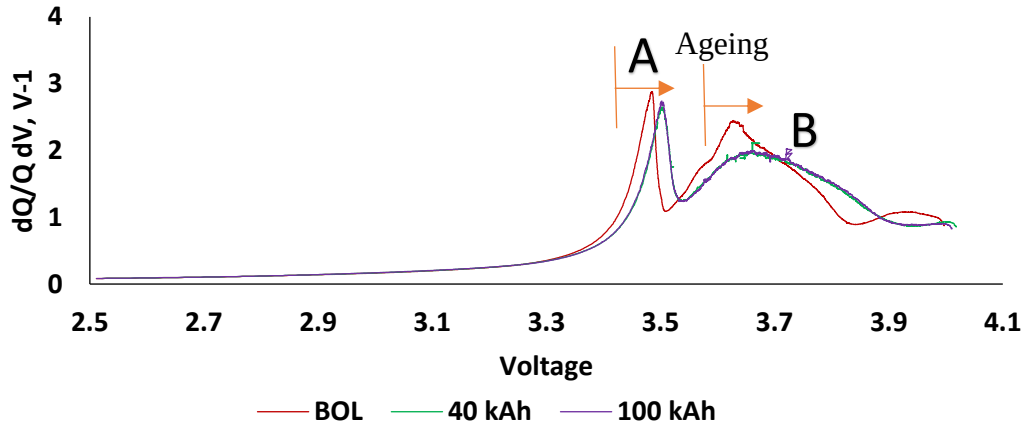

Figure 27: Incremental capacity plot for a battery cycled using the square profile

The shape of the ICA and DVA plots and peak locations for the experimental data differ from the plots obtained from literature. This phenomenon can occur due to the variations in the electrode chemistry. For example, two batteries with different ratios of nickel, manganese, and cobalt in their positive electrodes (and hence different ICA and DVA plots) can still be referred to as NMC positive electrodes. Though the shapes of the analysis plots differ between the experimentally generated data and the reference material, there are some similarities in how the characteristic peaks change as the batteries age. For example, comparing Figure 22, Figure 23, and Figure 24 there is an evolution of the peaks marked A and B as the batteries age. The peaks in Figure 22 shift

towards the left as the batteries age. This type of peak shift can be observed in Figure 23 and Figure 24 as well. *This shift is attributed by the authors to the loss of lithium due to side reactions* [106]. The differential voltage curves in reference [106] have been offset vertically by the authors for the sake of clarity but the slight broadening of the peaks at location B can be seen and this broadening of peaks can be observed in the experimentally generated curves as well. *A change in the shape of peaks can generally be attributed to a loss of active materials* [106].

Similar to DVA, ICA curves can also provide insight about the battery degradation mechanisms. For example, [109] lists some of the most common mechanisms of capacity fade and their corresponding contributions to the ICA plots. Generally, slight shifts in peaks to higher voltages can correspond to increased internal resistance of the battery while *changes in all observable peaks can indicate loss of active electrode material*. Figure 25 shows the ICA curves from reference [68]. Though the chemistries differ, certain similarities can be observed in the peak evolutions of Figure 25, Figure 26, and Figure 27. The peaks labeled A slightly shift to higher voltages which can indicate an increased resistance as the battery ages and there is also a change in the magnitude of the peaks for all observable peaks indicating a loss of active materials. The peak labeled B in Figure 25 does not shift to higher voltages but there is a significant change as the battery ages. The authors of [68] conclude the loss of lithium contributes to this change. This large change in peak magnitude is observed in the experientially generated curves as well suggesting loss of cyclable lithium due to side reactions.

Though the DVA and ICA can be done on full cells, the profiles generated in such tests tend to convolute the contributions of individual electrodes. Some of the peak evolutions observed in Figure 22 through Figure 27 can hold data about contributions from both electrodes and can only be decoupled by acquiring half-cell data or by the use of a mathematical model.

4.2 The Single Particle Model

The model used in this work to interpret the results from full cell measurements is based on the single particle model [27] and takes a macroscopic view of the battery. The single particle model simplifies the details of the electrodes and makes certain assumptions to relate physical parameters like concentration, active material, etc. to measureable parameters like current or voltage. The single particle model is derived from the 1+1D model [75], which is in turn derived from the

porous electrode theory [78], [110]. The assumptions made by these models are discussed in the following sections.

4.2.1 Porous Electrode Theory

The porous electrode theory was developed by Newman and Tiedmann in 1975 to address the simulation of flooded electrodes in primary and secondary batteries and electrochemical flow reactors, while considering phenomena such as the adsorption of ions by the electrodes as well as double layer charging near the electrodes.

- The complex geometry of the electrode is characterized by a specific interfacial area that is equal to the surface area per unit volume of the active material and this area is considered the active surface in the electrode.
- The amount of active material relative to the total electrode volume in an electrode is represented by a volume fraction ε_i
- The particles in the positive and negative electrode are joined together by an electrolyte pathway that allows for the axial movement of lithium ions but prevents the flow of electrons. This pathway represents the electrolyte/separator assembly that lies between the positive and negative electrodes and prevents the flow of electrons through the battery, preventing short circuits.
- The porous electrode theory assumes electro-neutrality in the electrodes and electrolyte. This means that there is always a balance between the number of positively and negatively charged particles in the system.
- Current density (A/m^2) is assumed uniform in the positive and negative electrodes and is considered zero in the separator.

4.2.2 1+1D Model

The porous electrode model can be simplified further into the 1+1D model (schematic shown in Figure 28) by making certain assumptions about the geometry of the electrodes and the reactions that occur at the electrodes. This model also assumes all the previously stated assumptions from the porous electrode theory. The assumptions added by the 1+1D model are

- The electrode is assumed to consist of spherical particles of equal size with a radius, R_i (m).
- Electrochemical reactions in the electrodes occur only at the surface of the spherical particles.
- The axial length can be discretized and a spherical particle can be assigned to each node.
- Gradients in current and potential occur only in the axial or x-direction.
- The lithium ions are stored inside the spherical particles and diffuse through the particle to participate in the electrochemical reactions at a rate determined by the flux at the particle surface.
- The diffusion of lithium in the particle is modelled as a species diffusion through a spherical particle.
- The electrochemical reactions happening at the surface of the particle are modelled with Butler-Volmer kinetics to calculate the activation overpotentials.

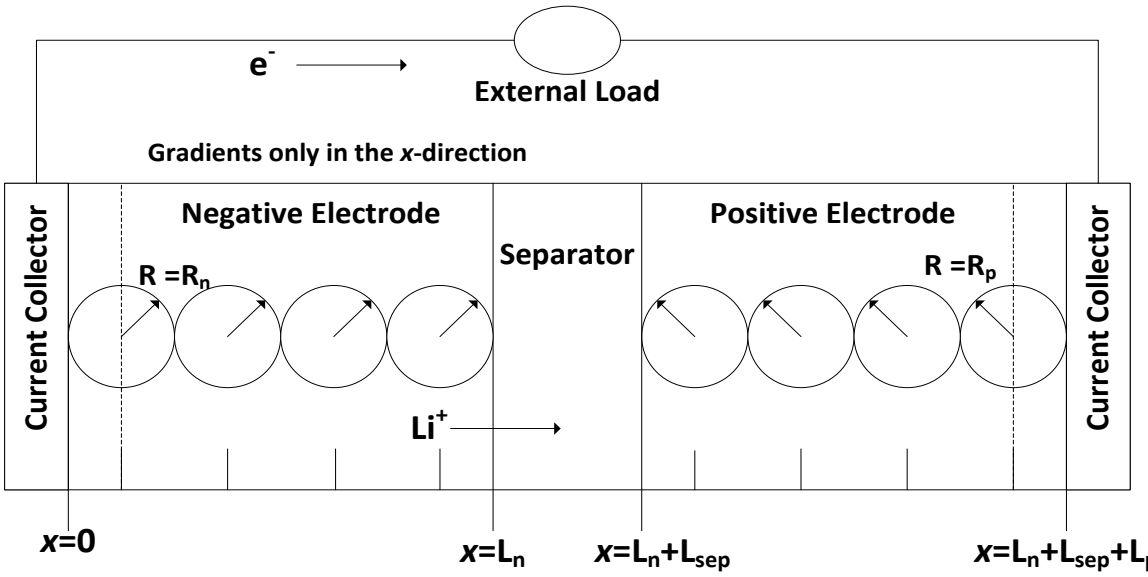

Figure 28: Schematic of the 1+1D model

The domain for the 1+1D model is characterized by the two spatial dimensions, x and r. This model has governing equations for the solid and electrolyte phases coupled by the current density. These partial differential equations (PDEs) can be solved for the concentration of lithium ions and, subsequently potentials, by discretizing in time and spatially in x and r. The resulting equations are then solved using a finite difference method.

4.2.3 The Single Particle Model Single Particle Assumption

The single particle model (SPM) is a further simplification of the 1+1D model that disregards the dependence of concentration on the x dimension in the electrodes thus allowing a single particle to be used to represent the average behavior of the active solid phase in each electrode. The schematic of the SPM is shown in Figure 29.

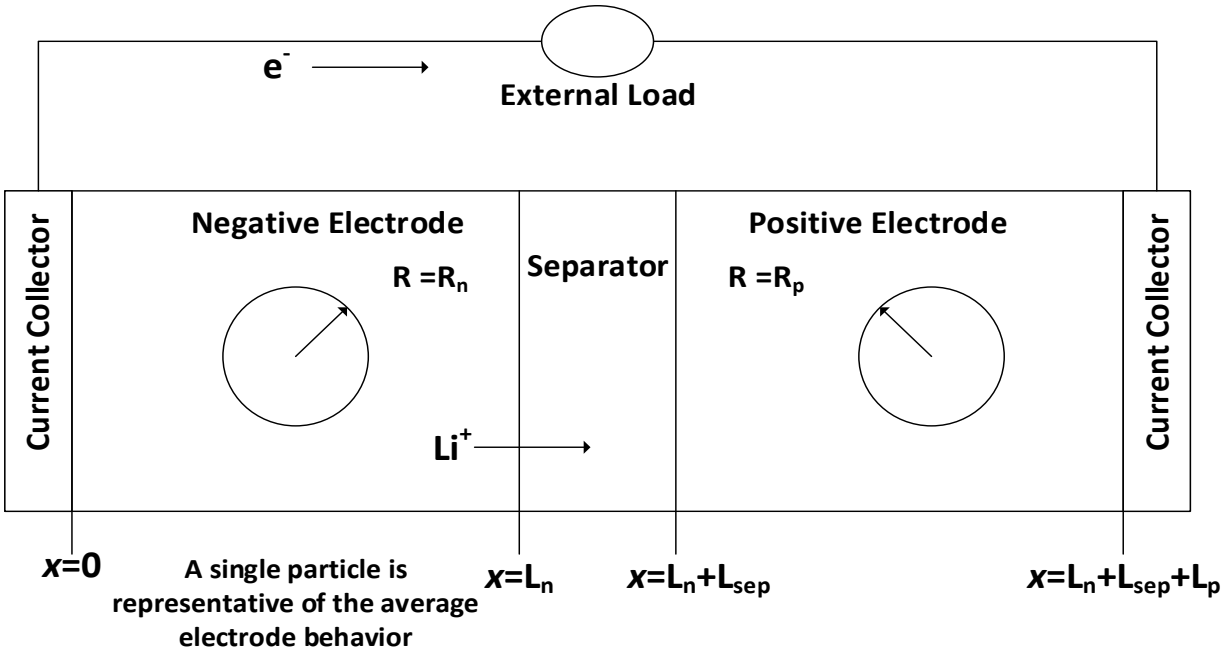

Figure 29: Schematic of the SPM

In the SPM, a single particle represents the average behavior of the entire electrode. The current density j_i (A/m^2) is averaged over the entire active surface and thus is uniform over the entire electrode particle. This current density for the electrode is given by the relation

$$j_i(t) = \frac{I(t)}{a_i A L_i} \tag{4.1}$$

where, I(t) (A) is the applied current, A (m^2) is the area of the current collector, L_i (m) is the thickness of the electrode and a_i (m^{-1}) is the interfacial area per unit volume of the electrode.

The interfacial area per unit volume of the electrode can be derived by first considering the ratio of surface area to the active volume of the electrode, which is given by

$$\frac{A_s}{V_p} = \frac{n_p 4\pi R_i^2}{n_p \frac{4}{3}\pi R_i^3} = \frac{3}{R_i} \tag{4.2}$$

where, n_p is the number of particles and V_p is the volume of the electrode particles. However, the particle volume of the electrode, Vp, can be written as

$$V_p = \varepsilon_i (L_i A) \tag{4.3}$$

where, L_i is the electrode thickness (m), A (m^2) is the current collector area and ε_i is the active volume fraction of the electrode. Using Eqs. (4.2) and (4.3),

$$\frac{A_s}{\varepsilon_i (L_i A)} = \frac{3}{R_i} \tag{4.4}$$

Thus, the active surface area per unit volume can be expressed as;

$$a_i = \frac{A_s}{(L_i A)} = \frac{3\varepsilon_i}{R_i} \tag{4.5}$$

The SPM is simpler than the 1+1D model because it does not account for the axial variation of the lithium ion concentration within the electrodes (a linear gradient is a simple assumption) but rather, considers the behavior of a single particle as an average representation of the electrode behavior, thus reducing the dependency of the solid phase lithium ion concentration in the model to only the r direction.

Usually, the SPM neglects the lithium ion concentration gradient in the liquid electrolyte phase and considers the potential drop across the electrolyte to be proportional only to the current. However, this assumption is only valid for low C-rates (< 1C) and the model used in this work takes the concentration gradient in the electrolyte into consideration, while calculating the potential drop across the electrolyte. This concentration gradient is calculated by considering a one-dimensional diffusion of the lithium ions from one current collector to the other through the electrolyte.

4.3 Governing Electrochemical Equations

4.3.1 Open Circuit Voltage and Electrode Potential

The open circuit voltage (OCV) of a cell is the potential difference between the electrodes of the cell when they are at equilibrium with no current flow. Usually, this OCV is a function of the SOC

of the cell. The potential of an electrode is always measured with respect to a reference electrode. Typically, the open circuit potential (OCP) of an electrode in a lithium ion cell is specified as the potential difference between the electrode and a pure lithium electrode. For example, the OCPs of the positive and negative electrodes of a graphite-NMC cell are given by

$$OCP_{NMC} = \phi_{NMC} - \phi_{Li} \tag{4.6}$$

$$OCP_{Li\,C_6} = \phi_{Li\,C_6} - \phi_{Li} \tag{4.7}$$

Thus, by combining equations (4.6) and (4.7), the OCV of the cell can be given by equation (4.8). Practically, the potential difference measured between the two electrodes when there is no current flow is considered the OCV of the cell.

$$OCV_{Cell} = OCP_{NMC} - OCP_{LiC_6} = \phi_{NMC} - \phi_{Li\,C_6} \tag{4.8}$$

The potential of an electrode is related to the change in the Gibbs free energy ΔG (J) and is given by the relation

$$\Delta G = -nF\Delta\phi \tag{4.9}$$

where, $\Delta\phi$ is the potential difference between the products and reactants in a reaction, n is the number of electrons involved in the reaction occurring at the electrode and, F (C/mol) is Faraday's constant. The Gibbs free energy change is a measure of the maximum useful work that can be obtained from a system for the given conditions of temperature, pressure, and concentration of the reacting species. The Gibbs free energy change at standard conditions of temperature, pressure and concentration is denoted by ΔG^0 and the relation between the standard potential and the Gibbs free energy change is

$$\Delta G^0 = -nF\Delta\phi^0 \tag{4.10}$$

The relationship between ΔG and ΔG^0 is given by;

$$\Delta G = \Delta G^0 + \bar{R}T\ln\left(\frac{\Pi_p a_p}{\Pi_r a_r}\right) \tag{4.11}$$

where $\bar{R}$ (J/K-mol) is the universal gas constant, T (K) is the temperature, $\Pi_p a_p$ is the product of the activities of the products, and $\Pi_r a_r$ is the product of the activities of the reactants, each evaluated at actual conditions. The activity is a measure of the deviation of the concentration from standard conditions. Eq. (4.9), (4.10) and (4.11) can be combined to form the Nernst equation that states the potential at non-equilibrium conditions.

$$\Delta\phi = \Delta\phi^0 + \frac{\bar{R}T}{nF}\ln\left(\frac{\Pi_p a_p}{\Pi_r a_p}\right) \tag{4.12}$$

The open circuit potential of an insertion material is given by Newman et.al. [110] as

$$\Delta\phi = (\phi^0 - \phi^0_{ref}) + \frac{\bar{R}T}{nF}\left(\ln\left(\frac{C_{max} - C_s}{C_s}\right) + \beta C_s + \zeta\right) \tag{4.13}$$

where β and ζ can be taken as activity correction factors for non-ideal behavior, C_s as the surface concentration and C_{max} is the saturation concentration. This equation is just another form of the Nernst equation (4.12) and accounts for the concentration of the reaction species on the surface of the particles.

Eq. (4.12) or (4.13) can be used to calculate the potential difference or OCV of an electrode pair as a function of the lithium concentration and temperature using mathematical models that calculate the activities with the help of empirical parameters [111]. However, in practice, the OCP of the electrode material can be obtained by discharging the electrodes at very low rates (≤ C/30) and measuring the potential against a lithium reference electrode.

Generally, in a system, species react spontaneously to minimize the total Gibbs free energy. The ΔG of a reaction is usually given by the difference in the Gibbs free energy between the products and reactions.

$$\Delta G_{reaction} = G_p - G_r \tag{4.14}$$

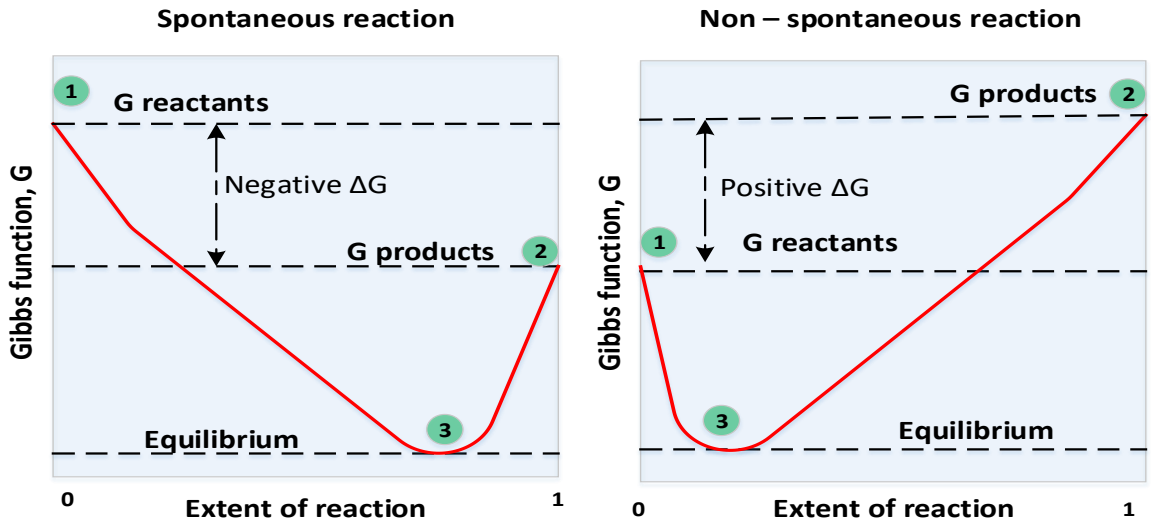

Figure 30: Gibbs free energy of reactions explained [112]

As given in Figure 30, if $\Delta G_{reaction}$ is negative, the reaction proceeds spontaneously to minimize the Gibbs free energy. Whereas, if it is positive, an application of external energy is needed to ensure the reaction proceeds in that particular direction. If $\Delta G_{reaction}$ is zero, then the reaction is at equilibrium. In the lithium ion battery, during the discharge process, the ΔG between the reactants and products at each electrode is negative thus, the battery discharges spontaneously when connected to an external load. However, when the battery is at the lowest SOC, the ΔG is positive and in order to charge the battery, an external potential has to be applied to overcome the ΔG barrier.

4.3.2 Kinetic Overpotential

The equilibrium OCV of the battery is determined by the OCP of the electrodes according to equation (4.8) which, in turn, depends on the concentration of lithium in the electrode, Eq. (4.13). However, when there is current flowing through the battery, equilibrium no longer exists and the electrode potentials depend on the rate of the electrochemical reaction happening at the surface of the particle. The rate of the reaction (mol/m^2-s) directly depends upon the reaction rate constant, k (m/s) and the concentration C_s (mol/m^3) of the reacting species at the reaction site (particle surface). Reactions at either electrode can proceed only after overcoming an energy barrier also known as the activation energy.

Generally, the reaction rate is expressed as

$$r_k = C_s k_{0,\mathrm{k}} \exp\left(\frac{\Delta G_{act,k}}{\bar{R}T}\right) \tag{4.14}$$

where *k* stands for anodic or cathodic, k_0 is the reaction rate constant, C_s is the concentration of the reacting species, and $\Delta G_{act,i}$ is the activation energy, which has to be overcome for the reaction to occur. The reacting species are the reduced species (R) which are oxidized by the anodic reaction (a) and the oxidized species (O) which are reduced by the cathodic reaction (c)

The relationship between the current density j_k and the reaction rate can be given by the expression

$$j_k = nFr_k \tag{4.15}$$

At each electrode, both the anodic and the cathodic reactions happen simultaneously and the overall reaction rate r can be given as a difference between the anodic and cathodic rates. Combining equations (4.10), (4.12), (4.14) and (4.15), an expression for j can be derived such that

$$j_i = nF\left(C_{s,R} k_{0,a} exp\left(\frac{nF(1-\alpha)\Delta\phi}{\bar{R}T}\right) - C_{s,O} k_{0,c} exp\left(\frac{-nF(\alpha)\Delta\phi}{\bar{R}T}\right)\right) \tag{4.16}$$

where α is a symmetry factor and is usually assumed to be 0.5. This equation is the well-known form of the Butler-Volmer equation and can be applied to both the positive and negative electrodes to obtain expressions for j_p and j_n. At equilibrium, when there is no net current flow, j_n and j_p are both zero, and an expression for $\Delta\phi_{\mathrm{eq}}$ can be obtained for each electrode from Eq. (4.16). However, during current flow, an additional potential is required to drive the reactions at each electrode. The direction of the reactions depends on the applied potential. This applied potential is also called the overpotential. The overpotential, η_i, can be stated as

$$\eta_i = \Delta\phi_i - \Delta\phi_{i,equilibrium} \tag{4.17}$$

Now, the expressions for j_p and j_n under non-equilibrium conditions can be obtained by combining Eq. (4.16) and Eq. (4.17) and also by equating the reaction rate constants for the anodic and cathodic reactions at each electrode $k_{0,c}$ and $k_{0,a}$ into one reaction rate constant (essentially considering the anodic and cathodic reactions to occur at similar rates at each electrode) specific to each electrode $k_{0,i}$.

$$j_p = nF\left(C_{s,R,p} k_{0,p} \exp\left(\frac{nF(1-\alpha)\eta_p}{\bar{R}T}\right) - C_{s,O,p} k_{0,p} \exp\left(\frac{-nF(\alpha)\eta_p}{\bar{R}T}\right)\right) \tag{4.18}$$

$$j_n = nF\left(C_{s,R,n}k_{0,n}\exp\left(\frac{nF(1-\alpha)\eta_n}{\bar{R}T}\right) - C_{s,O,pn}k_{0,n}\exp\left(\frac{-nF(\alpha)\eta_n}{\bar{R}T}\right)\right) \tag{4.19}$$

In the case of the lithium ion battery, the number of electrons participating in the reactions, *n*, is one. Also considering Eq. (4.13), Eq. (4.17), Eq. (4.18) and Eq. (4.19) and taking the value of α to be 0.5, the overpotential in the case of the SPM can be expressed in terms of the current density and concentration of lithium ions and is written as

$$\eta_i(t) = \frac{2\bar{R}T}{F}\sinh^{-1}\left(\frac{j_i(t)}{2j_0(t)}\right) \tag{4.20}$$

where j_0 is the combination of the concentration terms originating in Eq. (4.13) and is generally considered an exchange current density expressed as

$$j_{0,i}(t) = Fk_{0,\mathrm{i}}\sqrt{C_{s,i}(t)C_{e,i}(t)\left(C_{max,i} - C_{s,i}(t)\right)} \tag{4.21}$$

where C_e is the liquid phase concentration of lithium at the reaction site, $C_{s,i}$ is the concentration of intercalated lithium at the particle surface and $C_{max,i}$ is the saturation concentration of lithium in the electrode material [67], [86].

4.3.3 Lithium Concentration in the Electrode Particle

The potential of an electrode has a direct relation to the amount of lithium present in it. The model under consideration is based on spherical particles, and the assumption that the lithium diffuses through and is stored in the particles. Thus, the 1-D spherical diffusion equation is solved for the concentration of lithium in the electrodes. The governing equation for spherical 1-D diffusion is given by

$$\frac{\partial C_i}{\partial t} = \frac{D_i}{r^2}\frac{\partial}{\partial x}\left(r^2\frac{\partial C_i}{\partial r^2}\right) \tag{4.22}$$

where C (mol/m^3) is the concentration of lithium, D_i (m^2/s) is the diffusion coefficient and r (m) is the radius of the spherical particle. In addition, the boundary conditions are

$$\left.\frac{\partial C_i}{\partial r}\right|_{r=0} = 0 \tag{4.22a}$$

$$\left.\frac{\partial C_i}{\partial r}\right|_{r=R_i} = \pm\frac{j_i(t)}{D_i F} \qquad (4.22b)$$

where $j_i(t)$ is the current density in the electrode and R_i is the radius of the particle. These boundary conditions represent a flux condition at the external boundary and a symmetry condition at the center of the particle. An initial uniform concentration distribution C_0, can be assumed in the particle if there is a rest period before cycling. This type of equation usually results in concentration profiles similar to Figure 31, which shows the concentration profile for a particle under discharge at some constant C-rate (1C) at different times. The figure shows that the concentration at r=0 continuously decreases with time as the lithium diffuses out through the particle to the surface to participate in the reaction.

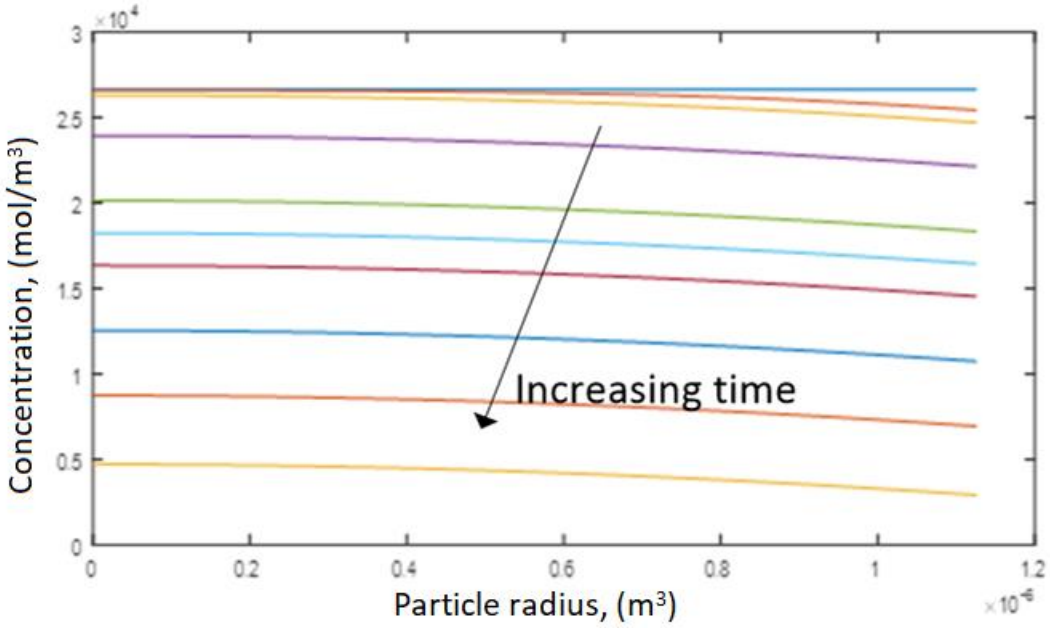

Figure 31: Graphical representation of lithium concentration in an electrode

4.3.4 Potential Drop across the Electrolyte

The charge in the lithium ion battery is carried by the electrons externally and lithium ions internally. This internal charge transport occurs through the electrolyte. This diffusion process in the SPM is assumed as one-dimensional and occurs only in the axial or x-direction. When there is a charge transfer, a potential drop can always be expected. In the case of lithium ion transport in the liquid phase of the battery, there are two components. An overpotential due to ionic current flowing through the electrolyte with a conductivity σ (regardless of the concentration gradient).

This term can be considered to be purely ohmic. The other component is the overpotential required to overcome a lithium concentration gradient in the electrolyte. During operation, there is usually an excess of lithium near the electrode where lithium is oxidized (negative electrode for discharge) and a lack of lithium near the reducing electrode (positive electrode for discharge), setting up a concentration gradient across the electrolyte. Therefore, any potential drop across the electrolyte is a combination of ohmic loss (due to conductivity σ) and loss due to the concentration gradient. According to concentrated solution theory [113], the expression for the potential drop across a concentrated electrolyte is given by

$$\frac{\partial \phi_e}{\partial x} = \frac{i_e(t)}{\sigma_e} + \frac{2\bar{R}T(1-t_0^+)}{F}(1+\gamma)\frac{\partial \ln(C_e)}{\partial x} \tag{4.23}$$

where, γ is a correction term to account for non-ideal behavior and σ_e (S/m) is the conductivity of the electrolyte. This equation when solved between the midpoint of the negative electrode and the midpoint of the positive electrode results in a voltage drop across the electrolyte, which is found from the expression;

$$\Delta V_e(t) = \frac{I(t)\left(\frac{1}{2}L_p + L_{sep} + \frac{1}{2}L_n\right)}{\sigma_e A} + \frac{2\bar{R}T(1-t_0^+)}{F}(1+\gamma)\ln\left(\frac{\bar{C}_{e,n}(t)}{\bar{C}_{e,p}(t)}\right) \tag{4.24}$$

where the first term on the right hand side is an ohmic loss term and the second term accounts for the concentration gradients and non-ideal behavior and $\bar{C}_{e,i}$ is the average concentration of lithium in the liquid phase in each electrode.

4.3.5 Lithium Transport in the Electrolyte

In order to solve Eq. (4.24), the concentration profile of lithium in the electrolyte has to be established. The electrolyte of a lithium ion battery is usually a lithium salt dissolved in a solvent ($LiPF_6$ in 1:1 ratio of EC:DMC). The expression for the concentration of lithium ions in the electrolyte as the battery cycles can be obtained by solving the one dimensional diffusion equation

$$\varepsilon_e \frac{\partial C_e}{\partial t} = D_e \frac{\partial^2 C_e}{\partial x^2} \pm \frac{3(1-t_0^+)}{FR_i} j_i(t) \tag{4.25}$$

with the boundary conditions:

$$\left.\frac{\partial C_e}{\partial x}\right|_{x=0} = 0 \tag{4.25a}$$

$$\left.\frac{\partial C_e}{\partial x}\right|_{x=L_{bat}} = 0 \qquad (4.25b)$$

where ε_e is an adjustment for the porosity of the electrodes and the separator, D_e is the average diffusion coefficient of lithium in the liquid phase and the term $\frac{3(1-t_0^+)}{FR_i} j_i(t)$ accounts for the insertion and removal of lithium ions from the electrodes. This expression, mathematically analogous to a source or sink term in 1-D diffusion or heat transfer, is zero in the separator region of the liquid phase and has a finite value in the electrode regions, dependent on the current density at the respective electrodes. The variable $t_0^+$is called the transference number and is a transport property of the electrolyte representing the fraction of current carried by the positive ion in the electrolyte [4], [67], [74], and [75]. Once the concentration profile across the electrode is known, the average concentration can be determined for use in Eq. (4.24).

4.3.6 Battery Voltage

Considering equations (4.8), (4.20), and (4.24), an expression for the cell voltage can be derived as

$$V(t) = \phi_p(t) - \phi_n(t) - \Delta V_e(t) - \Omega_i I(t) \qquad (4.26)$$

where $\phi_i(t)$is the electrode potential and is given by

$$\phi_i(t) = \mathrm{OCP}_i(t) \pm \eta_i(t) \qquad (4.27)$$

and the *OCP* is the concentration dependent open circuit potential of the electrode, η_i is the kinetic overpotential and Ω (ohm) is a time varying resistance term used to account for changes in the internal resistance of the cell. It obtained from the HPPC data and is adjusted to exclude the voltage drop $\Delta V_e(t)$ in the electrolyte.

4.4 Model Formulation and Solution

4.4.1 Spherical Diffusion

The 1-D diffusion in the spherical particle in the 'r' direction and the 1-D diffusion in the electrolyte in the 'x' can be solved by using either an analytical solution or a numerical method. Initially, an analytical solution to the spherical diffusion problem was considered. This solution is well established in heat transfer problems and is given in [83]. The concentration distribution of the lithium ion in the solid particle is given by the expression

$$C_i(r,t) = C_{0,i} \pm \frac{j_i R_i}{F D_i}\left[\frac{3}{10} - \frac{r^2}{2R_i^2}\frac{-3D_i t}{R_i^2} + 2\sum_{n=1}^{\infty}\frac{R_i^2 \sin\left(\lambda_n \frac{r}{R_i}\right)}{r^2 \lambda_n^2 \sin(\lambda_n)} \exp\left(\frac{-D_i \lambda_n^2 t}{R_i^2}\right)\right] \quad (4.28)$$

where λ_n is an eigenvalue in the analytical solution and is obtained by the solution to the equation

$$\lambda_n = \tan(\lambda_n) \quad (4.29)$$

The accuracy of this analytical solution depends on the number of terms included in the summation in Eq. (4.28). However, insignificant gain in accuracy was found for n>40. In order to eliminate any possible truncation error due to the summation terms, n was set to 100 in the model. At any time, t, the concentration of lithium on the particle surface can be calculated by setting r = R_i in equation (4.28) and the volume averaged bulk concentration of the particle can be calculated by integrating the expression for concentration, which is

$$\bar{C}_i(\mathrm{t}) = \int_0^{R_i} C_i(r,t)\frac{r^2}{R_i^3}\,dr \quad (4.30)$$

The concentration distribution of lithium in a particle during the anodic reaction, as a function of the current and particle radius generated from the model using the analytical solution, is given in Figure 32. As shown in the figure, the analytical solution captures the physics of the diffusion process, i.e., increasing current leads to a steeper gradient at the particle surface.

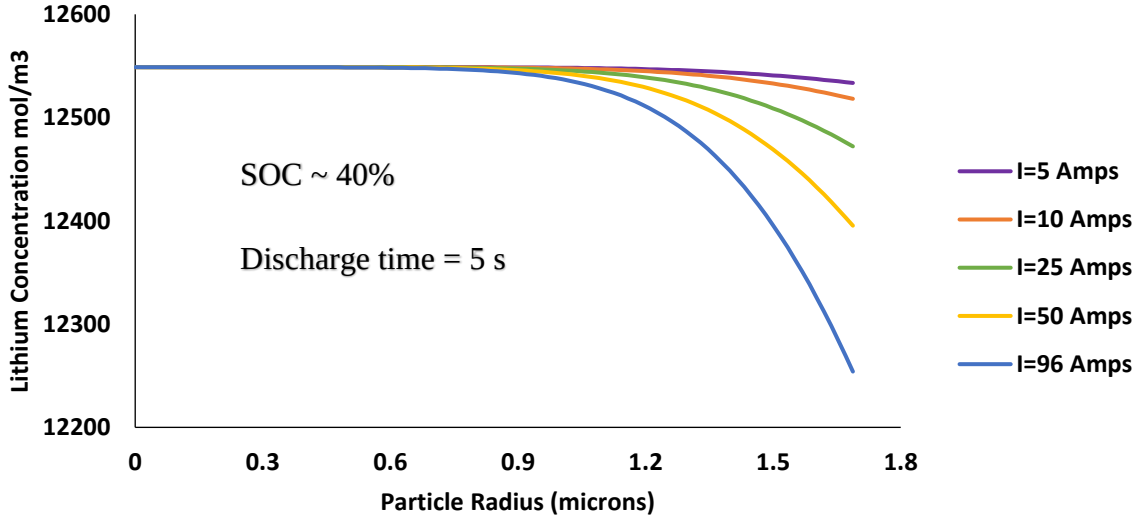

Figure 32: Concentration of lithium ions in a negative electrode particle as calculated with the analytical solution

This analytical solution is not without its limitations. The solution in Eq. (4.28) is applicable only when a steady boundary condition exists at $r=R_i$ (Eq. 4.22b), i.e., the applied current must remain steady. Unfortunately, in order to be considered useful for cycling studies, the solution approach used in the model must be able to predict the battery voltage not only during steady boundary conditions such as those for the 1C charge-discharge tests used during the RPTs but also for the time varying boundary conditions seen during cycling.

There are established analytical solution methods for transport problems that can accommodate time dependent boundary conditions such as, for example, Duhamel's superposition integral, Laplace or Fourier transforms, etc. [114]. However, these solutions usually require the time-dependent boundary condition to be some form of a known function in order to obtain an analytical solution. In the case of the pulse profile current signal, it is not easy to fit a known function to the profile for use as the boundary condition equation. Therefore, some other method has to be considered to solve the model and successfully predict the voltage response of the battery.

One other important assumption in the analytical solution is the presence of an initial uniform lithium distribution, C_o, inside the electrode particle. However, this assumption is valid only if the particle has been at rest prior to cycling. This is not the case during cycling since there is no time delay between consecutive current waveforms, which does not give the lithium any time to redistribute within the particle, thus, negating the assumption of a uniform initial condition. The method used to solve the model must accommodate this non-uniform initial condition in addition to the varying boundary conditions in order to be useful.

The solution to these problems (i.e. varying boundary conditions and non-uniform concentration profiles) can be obtained by using a numerical solution method rather than an analytical solution. The diffusion of lithium in the solid electrode particle can be solved using a finite difference, partial differential equation solver in Matlab called PDEPE [115]. This method is forward marching in the r-direction and backwards, i.e., explicit, in time. The use of a built-in function reduces computing complexity significantly and allows the use of an array of current values at discrete points in time as an input to the model, eliminating the need for a function to fit the pulse

profile current. This input array consists of 120 discrete values for current, which are then used to solve for the voltage response of the battery over a period of 5 seconds per array element, bringing the total cycle time to 600 seconds.

The resulting concentration distribution within each particle at the end of the cycle is saved for use as the initial condition for the subsequent time step, thus, accounting for the non-uniform initial condition associated with cycling studies. This method also captures the physics of the diffusion process as seen in Figure 33, which shows the concentration of lithium inside a negative electrode particle as a function of particle radius for different values of current.

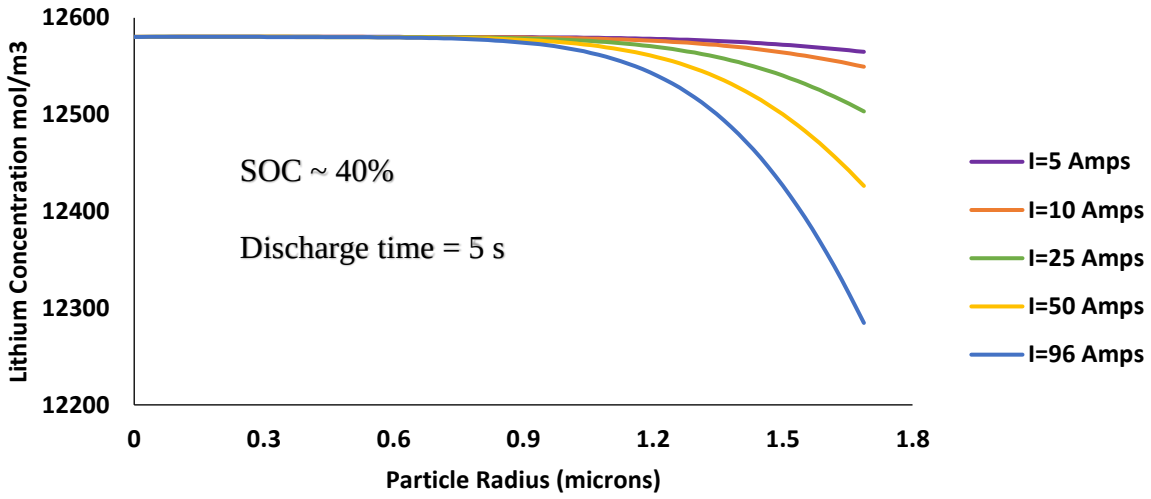

Figure 33: Concentration of lithium ions in a negative electrode particle as calculated by the PDEPE function

In the analytical solution, calculating the SOC of the battery during each time step was straightforward as it involved integrating an expression for the concentration (Eq. 4.30). When the finite difference solution is applied to the model, closed form integration is no longer possible due to discrete concentration values and a numerical approach has to be adopted. To do so, the electrode particles are split into concentric spherical shells as shown in Figure 34. The number of spherical

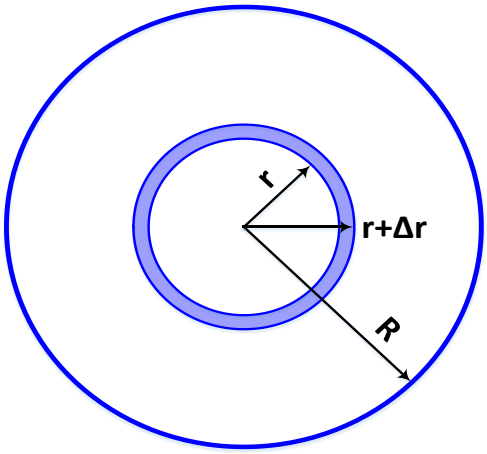

Figure 34: Illustration of concentric spheres considered for SOC calculation in the finite difference approach

shells depends on the r-direction resolution used in the model. The amount of lithium-stored in each shell can be calculated using

$$n_{Li}^{k} = \left(\frac{\left(C_{Li}^{r_{k+1}} + C_{Li}^{r_k}\right)}{2}\right) \times \left(\frac{4}{3}\pi[(r_{k+1})^3 - (r_k)^3]\right) \tag{4.31}$$

where r_k is the radius of the first shell, $r_{k+1} = r_k + \Delta r$ is the radius of the subsequent shell, n is the number of moles of lithium and C (mol/m^3) is the concentration of lithium. The total amount of lithium in the particle can now be calculated by summing up Eq. 4.31 over the entire sphere, i.e.

$$N_{Li} = \sum_{k=1}^{k=\left(\frac{R}{\Delta r}+1\right)} n_{Li}^{k} \tag{4.32}$$

From the total amount of lithium stored in an electrode particle, it is simple to calculate the state of charge, which is just a ratio of the total lithium stored to the theoretical maximum possible.

4.4.2 Diffusion in the Electrolyte

The diffusion process in the electrolyte is also solved using the built-in PDEPE function in Matlab. A representative solution generated by this function for the concentration of lithium ions in the electrolyte is shown in Figure 35. It can be observed that this program is able to capture the physics of the ion diffusion well. Initially, as soon as there is current flow (the discharge process), the lithium ion concentration in the electrolyte at the negative electrode of the battery increases due to diffusion of lithium ions from the electrode into the electrolyte. As time passes, the lithium ion

concentration slowly starts to reduce due to migration towards the positive electrode. At the positive electrode side, the concentration of the lithium ions in the electrolyte decreases sharply at the beginning of the discharge due to initial intercalation of the ions into the electrode. Subsequently, the concentration continues to reduce at a smaller rate as ions migrate from the negative electrode and diffuse into the electrode.

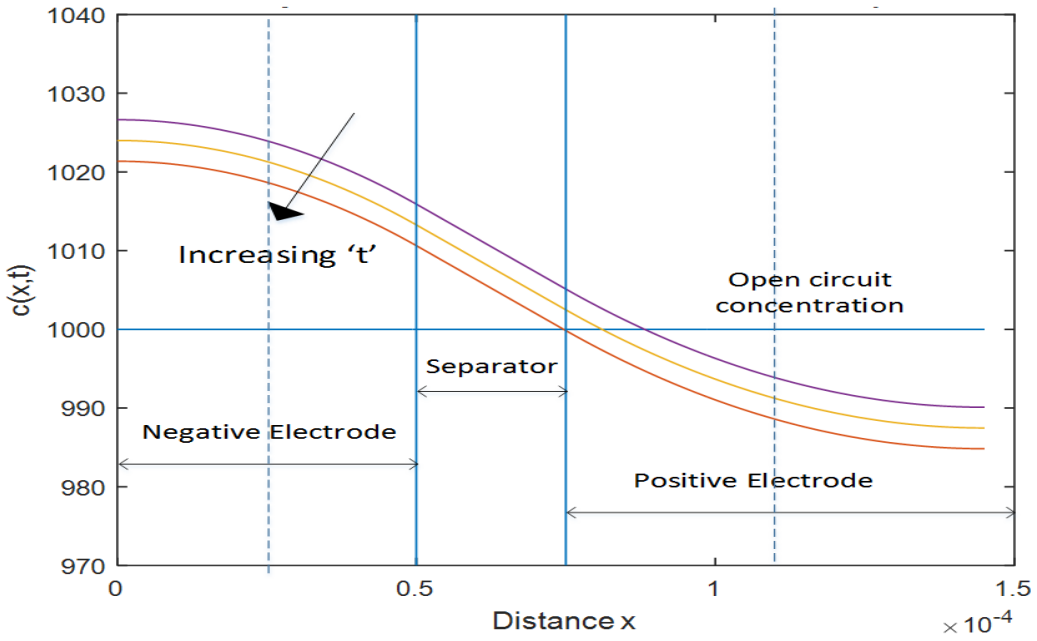

Figure 35: Concentration of lithium ions in the electrolyte as calculated by the PDEPE function

4.4.3 OCP vs. SOC Curves

The OCP vs. SOC information for most electrodes is an intrinsic material property. This information is established by discharging the electrode against a reference electrode (usually lithium) at very low rates (less than C/30) to minimize any overpotentials. The OCP vs. SOC for a graphite negative electrode from [4] and [86] is shown in Figure 36.

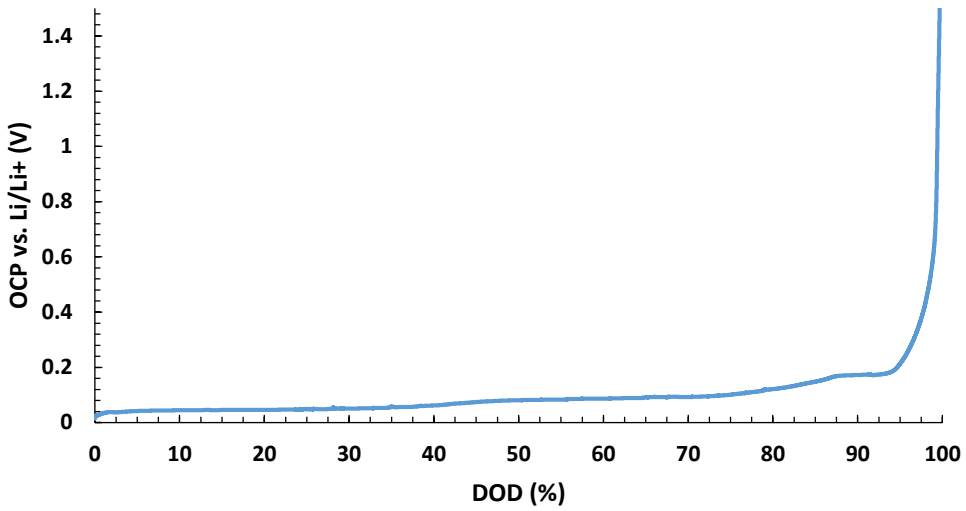

Figure 36: OCV vs. DOD data for a graphite negative electrode [4] and [86]

For the positive electrode, the half-cell data available in literature [116] was not an accurate match to the data observed. The best method to obtain this information would be to collect a sample of the positive electrode material from the batteries being tested and run half-cell capacity tests at very low C-rates. However, sponsor restrictions prevented the disassembling of the batteries to obtain electrode materials. In order to overcome this restriction, an experiment was designed to measure the OCP vs. SOC information of the battery. The batteries were cycled at extremely low rates (C/30) and the resulting voltage vs SOC information was collected. In addition, there was no hysteresis observed. The battery voltage is given by equation (4.26) and (4.27). However, at very low C-rates, the overpotential and resistance terms can be safely neglected. This in turn makes the battery voltage a function of electrode OCP only. Assuming that the negative electrode material is graphite, the OCP of the graphite from [4] and [86] can be added to the battery voltage to estimate the OCP vs SOC information for the positive electrode. This method can be expressed by the relation

$$OCP_p(t) = V(t) + OCP_n(t) \tag{4.33}$$

The resulting OCP vs SOC curve from this method is given in Figure 37.

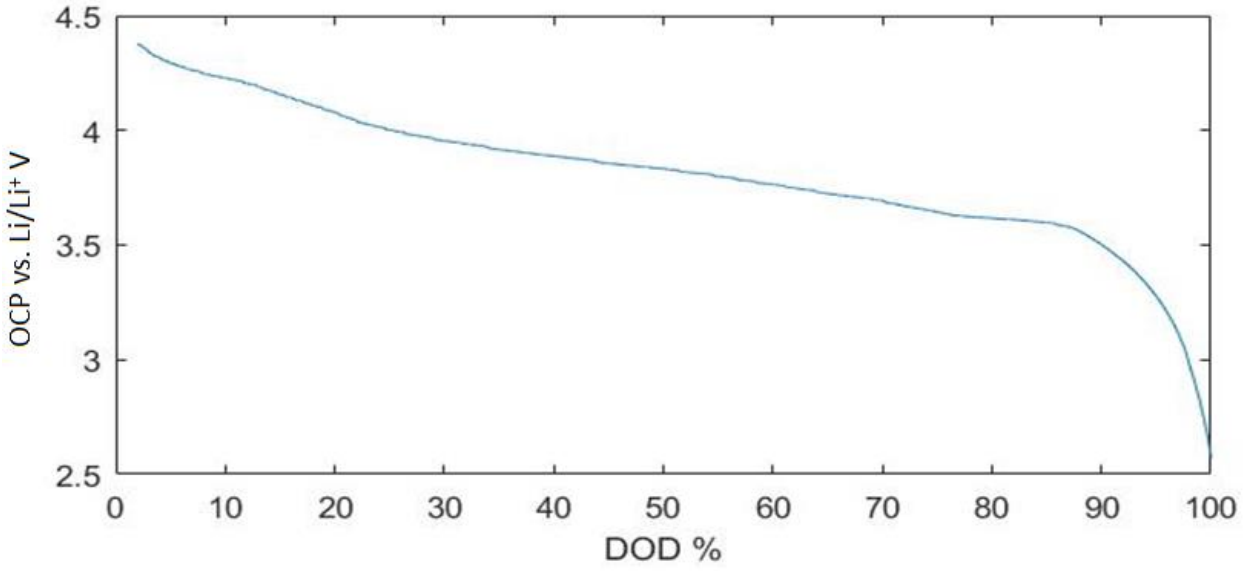

Figure 37: DOD vs OCV data for the positive electrode derived from experimental data for commercial NMC battery

Table 7: Summary of important equations used in the model

Current Density (A/m^2)	$j_i = \frac{IR_i}{3(L_i A)\varepsilon_i}$	(4.1)
Overpotential (V)	$\eta_i(t) = \frac{\bar{R}T}{2F} sinh^{-1}\left(\frac{j_i(t)}{2j_0(t)}\right)$	(4.20)
Exchange current density (A/m^2)	$j_{0,i}(t) = Fk_0\sqrt{C_{s,i}(t)C_{e,i}(t)\left(C_{max,i} - C_{s,i}(t)\right)}$	(4.21)
Lithium concentration in the electrode (mol/m^3)	$\frac{\partial C_i}{\partial t} = \frac{D_i}{r^2}\frac{\partial}{\partial r}\left(r^2\frac{\partial C_i}{\partial r}\right), \quad \left.\frac{\partial C_i}{\partial r}\right\|_{r=0} = 0, \quad \left.\frac{\partial C_i}{\partial r}\right\|_{r=R_i} = \pm\frac{j_i(t)}{D_i F}$	(4.22)
Lithium concentration in the electrolyte (mol/m^3)	$\varepsilon_e\frac{\partial C_e}{\partial t} = D_e\frac{\partial^2 C_e}{\partial x^2} \pm \frac{3(1-t_0^+)}{FR_i}j_i(t), \quad \left.\frac{\partial C_e}{\partial x}\right\|_{x=0} = 0, \quad \left.\frac{\partial C_e}{\partial x}\right\|_{x=L_{bat}} = 0$	(4.25)
Voltage drop across the electrolyte (V)	$\Delta V_e(t) = \frac{I(t)\left(\frac{1}{2}L_p + L_{sep} + \frac{1}{2}L_n\right)}{\sigma_e A} + \frac{2\bar{R}T(1-t_0^+)}{F}(1+\gamma)ln\left(\frac{\bar{C}_{e,n}(t)}{\bar{C}_{e,p}(t)}\right)$	(4.24)
Battery Voltage (V)	$V(t) = \phi_p(t) - \phi_n(t) - \Delta V_e(t) - \Omega I(t)$	(4.26)
Analytical expression for the lithium distribution in the electrode particle	$C_i(r,t) = C_{0,i} \pm \frac{j_i R_i}{FD_i}\left[\frac{3}{10} - \frac{r^2}{2R_i^2} - \frac{3D_i t}{R_i^2} + 2\sum_{n=1}^{\infty}\frac{R_i^2 sin\left(\lambda_n\frac{r}{R_i}\right)}{r^2\lambda_n^2 sin(\lambda_n)}e^{\left(\frac{-D_i\lambda_n^2 t}{R_i^2}\right)}\right]$	(4.28)
Amount of lithium in each shell – numerical solution approach	$n_{Li}^k = \left(\frac{\left(C_{Li}^{r_{k+1}} + C_{Li}^{r_k}\right)}{2}\right) \times \left(\frac{4}{3}\pi[(r_{k+1})^3 - (r_k)^3]\right)$	(4.31)
Total lithium in particle – numerical solution approach	$N_{Li} = \sum_{k=1}^{k=\left(\frac{R}{\Delta r}+1\right)} n_{Li}^k$	(4.32)

4.5 Parameters Affecting the Model

The model discussed in the previous sections is summarized in Table 7 and has a number of adjustable parameters that determine how accurately the model describes the real world behavior

of the battery. The parameters used in this study are listed in Table 8. Some of these parameters were obtained from the literature and some were adjusted after comparing the results of the model to the experimental results.

Table 8: Key parameters used in the model

Parameter	Unit	Description	Value	Common Range	Variable/Literature
$R_{s,n}$	μm	Graphite particle radius	1.7	1 – 20	Variable parameter
$R_{s,p}$	μm	NMC particle radius	1.0	10^{-3} – 10	Variable parameter
ε_n	-	Active material fraction, graphite	0.65	0.5 – 0.7	Variable parameter
ε_p	-	Active material fraction, NMC	0.90	0.4 – 0.8	Variable parameter
A	m^2	Current collector area	1	Based on battery size	Variable parameter
L_n	μm	Graphite thickness	15	10 – 100	Variable parameter
L_p	μm	NMC thickness	7.5	10 – 100	Variable parameter
L_{sep}	μm	Separator thickness	25	20 – 30	[27], [76]
σ	S/m	Electrolyte conductivity	12.34	10 – 14	[6], [117]
γ	-	Electrolyte activity coefficient	1.75	-	
t_0^+	-	Ion transference number	0.39	0.37 – 0.41	[117]
$C_{max,n}$	mol/m^3	Lithium saturation concentration in graphite	30540	30000 – 33000	[67], [86]
$C_{max,p}$	mol/m^3	Lithium saturation concentration in NMC	35340	35000 – 35550	[67]
k_n	$m^{2.5}/mol^{0.5}/s$	Kinetic rate constant, graphite	2.0×10^{-9}	10^{-8} – 10^{-10}	Variable parameter [86]
k_p	$m^{2.5}/mol^{0.5}/s$	Kinetic rate constant, NMC	1.85×10^{-10}	10^{-8} – 10^{-10}	Variable parameter [86]
D_n	m^2/s	Diffusion coefficient, graphite	7.5×10^{-14}	10^{-16} – 10^{-14}	Variable parameter
D_p	m^2/s	Diffusion coefficient, NMC	2.85×10^{-15}	10^{-15} – 10^{-13}	Variable parameter
D_l	m^2/s	Diffusion coefficient, electrolyte	4.5×10^{-10}	10^{-12} – 10^{-10}	Variable parameter
Brugg	-	Bruggeman coefficient	2	1.5 – 4	[118], [119]

4.5.1 Battery Capacity

As indicated by the literature reviewed in Chapter 2, the positive electrode determines the capacity of the battery. The negative graphite electrode is usually designed to accommodate more lithium than can be provided by the positive electrode. In general, the negative material can accommodate one and a half to two times the amount of lithium released by the positive material during the charging process [4], [67], [76], and [86]. In this study, the capacity of the negative electrode is taken to be 1.5 times that of the positive electrode. The capacity of an electrode is given by

$$C_i = c_{i,th} A L_i \varepsilon_i \rho_i \tag{4.34}$$

where $c_{i,th}$ (Ah/kg) is the theoretical capacity of the material, A (m^2) is the area of the current collector, L_i (m) is the electrode thickness, ε_i is the active material volume fraction, and ρ_i (kg/m^3) is the density of the material. Usually, when an electrode is fabricated, the electrode active material is combined with a binder such as Polyvinylidene fluoride (PVDF) to ensure the physical cohesiveness of the electrode. This reduces the fraction of the electrode that participates in the electrochemical reactions. In addition, the electrode structure is porous to allow penetration of the electrolyte. The active material volume fraction accounts for the discrepancy between the overall electrode volume and the volume of just the active materials. This fraction is an important parameter for calculating properties of the battery such as the capacity and the current density in the electrode. The theoretical capacity and density are material properties that were obtained from literature. For this project, the thickness of the electrode, the active material volume fraction and the current collector area are not directly measureable due to sponsor restrictions. However, the overall capacity of the battery (5 Ah) is known and it can be used to establish reasonable estimates of the three parameters which, when put together, satisfy equation (4.34).

4.5.2 Mass Balance between Electrodes

During the operation of the lithium ion battery, lithium ions travel between the electrodes and the electrons travel through an external circuit. However, the SOC differential or the ΔSOC is not equal between the two electrodes. This stems from the negative electrode's larger capacity compared to the positive electrode. In the model, this discrepancy between the ΔSOC can be addressed by realizing that the total number of lithium ions in the system is constant and any ions that leave one electrode must enter the other. The number of lithium ions leaving an electrode (i = n for negative or p for positive) for a particular ΔSOC is given by the expression:

$$N_{Li,i} = \Delta SOC_i . C_{i,max} \frac{4}{3} \pi R_i^3 \left(\frac{n_{p,i}}{A}\right) A \tag{4.35}$$

where, $C_{i,max}$ is the saturation concentration of lithium in the electrode and R_i is the particle radius[8]. Due to sponsor restrictions that preclude dismantling the cell, the particle radius is also not measurable and it is considered an adjustable parameter. The term, (np^i/A), is the number of active particles per unit area in the electrode and is obtained from the expression

$$\varepsilon_i L_i A C_{i,max} = \left(\frac{n_{p,i}}{A}\right) A \frac{4}{3} \pi R_i^3 C_{i,max} \tag{4.36}$$

Combining (4.35) and (4.36), a ratio between the ΔSOC for each electrode during cycling can be incorporated into the model as

$$\frac{\Delta SOC_n}{\Delta SOC_p} = \frac{C_{max}^p \varepsilon_p L_p}{C_{max}^n \varepsilon_n L_n} \tag{4.37}$$

4.5.3 Diffusion Coefficients and Kinetic Constants

The diffusion coefficient D_i (m^2/s) from Fick's law, i.e., the proportionality constant between the molar flux and the concentration gradient that drives the diffusion, is a parameter that is used to model the one-dimensional diffusion of lithium in the spherical particles. The values of the diffusion coefficients for the electrode materials have been identified in the literature using techniques such as impedance analysis and low temperature cycling [74], [75], [107], and [120]. However, these methods are currently beyond the scope of this work and values from the literature [67] were used as a starting point after which, the model output was studied and compared with the experimental data to ascertain the ideal diffusion coefficient values that provide the best agreement with the data. The values for the kinetic-rate constants that directly affect the exchange current density were also obtained from literature initially [67] and then, similar to the diffusion coefficients, the ideal values were established for the best agreement with experimental data.

4.5.4 Electrolyte Transport Parameters

The diffusion of lithium in the liquid phase plays a vital role in determining the behavior of the battery. Once the lithium ions leave an electrode particle, they diffuse through the electrolyte, and the separator to reach the reaction site on the surface of the other electrode. The diffusion

[8] In this model, all electrode particles are considered spherical and the single particle model averages the behavior of one particle as the average electrode behavior.

coefficient determines the diffusion behavior of the ions and, consequently, the concentration profile of lithium in the liquid phase. The diffusion coefficient also contributes to both the voltage drop across the electrolyte (Eq. 4.21, 4.23) and the exchange current density (Indirectly through the liquid phase concentration at the reaction site, *Ce*, in Eq. 4.18). The diffusion coefficient is a physical property of a particular ion and solvent combination that depends on both temperature and the concentration of the ion in the solvent. Usually, an increase in the salt concentration leads to a decrease in the diffusion coefficient [6], [117], [121], and an increase in temperature leads to increased diffusion coefficients [121] and [122]. Studies measuring diffusion coefficients by using either electrochemical methods or other techniques such as nuclear magnetic resonance (NMR) [6], [123], [124], [125] report values on the order of 10^{-12} – 10^{-10} (m^2/s). The value chosen in this study is well within the published range in the literature (Table 8).

When considering systems with porous media, as in the case of battery electrodes and separator, the diffusion coefficient is usually expressed as an "effective" diffusion coefficient. This "effective" diffusion coefficient accounts for the geometry of the porous media in which the electrolyte solvent is dispersed. When measuring the diffusion coefficient by techniques such as NMR, only the solvent and the ion are taken into consideration. However, the ion rarely travels in a straight path from one electrode to the other. Usually, the ion has to navigate around obstacles in its path such as active material particles and or binder particles, or it has to travel a specific physical path as in the case of a polymer separator. This is usually referred to as tortuosity. This is shown in Figure 38 where the electrode and binder particles prevent the straightforward path of an ion. This tortuous path effectively decreases the diffusion coefficient by restricting the movement of the ion.

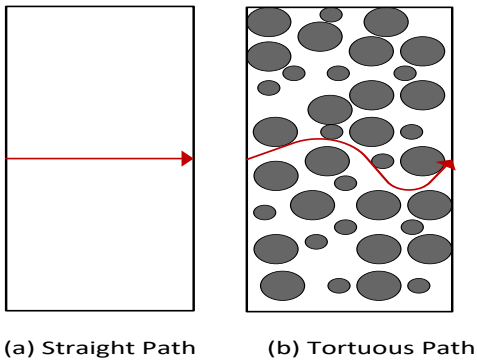

Figure 38: Straight and tortuous path of a particle

The concept of an effective diffusion coefficient based on the geometry of the porous media originates from the work of Bruggeman [118]. A correction factor named in honor of Bruggeman is used to obtain the effective diffusion coefficient. The Bruggeman model effectively relates the porosity of the medium to the tortuosity. This relation expresses the effective diffusion coefficient as a function of the porosity and is given by the relation,

$$D_{eff} = D_l \times \varepsilon^{\frac{(1+n)}{n}} \tag{4.36}$$

where D_l is the diffusion coefficient of the ion in the solvent alone, ε is the porosity of the medium, and n the Bruggeman coefficient which is 2 for spherical particles and 1 for cylindrical particles and accounts for the tortuosity effects.

In addition to the diffusion coefficient, the voltage drop across the electrolyte also depends on the physical dimensions of the battery, the transference number t_0^+ of the electrolyte and the effective activity coefficient γ. The transference number or the ion transference number accounts for the differences in the charge carrying capacities of various species in the electrolyte. The activity coefficient is used correct for the deviation of the electrolyte from ideal to non-ideal behavior. In this study, these parameters were obtained from the literature [6], [67]. The conductivity of the electrolyte σ (S/m) also plays an important role in deciding the voltage drop. While the diffusion coefficient is inversely proportional to the salt concentration, the conductivity is directly dependent (i.e., as the salt concentration goes up, so does the conductivity). The salt concentration has to be carefully chosen to balance the effect on both the diffusion coefficient and the conductivity.

Chapter 5 - Results

Results from Commercial Cell Cycling

5.1 Beginning of Life Testing

Reference performance tests were performed on the batteries initially to establish a baseline against which all future tests would be compared. Results from these tests include the capacity and the HPPC power data. It can be noted from Figure 39, which compares the discharge capacities between the two battery packs at the beginning of life (BOL), that there were no significant differences in the capacity of the batteries with respect to each other. The average capacity of the batteries was 4.96 Ah, (represented by the dashed black line) with a standard deviation of ± 0.12 Ah. Batteries 1 through 11 were allocated for the simple square profile and batteries 12 through 22 were allocated for the pulse profile.

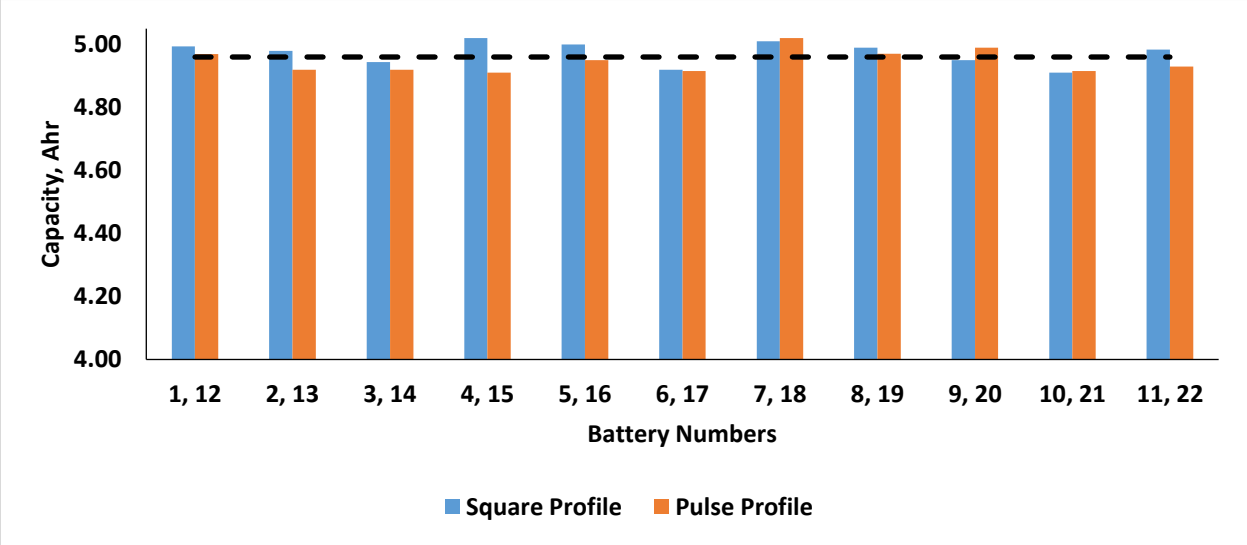

Figure 39: Beginning of life discharge capacities of 22 batteries

5.2 Cycling at 40 Percent SOC

5.2.1 Capacity Results for Batteries Cycled at 40 percent SOC

As discussed in earlier sections, eleven batteries were initially cycled at 40 percent SOC until 40 kAh of charge throughput[9]. After 40 kAh, four batteries from each pack were removed for higher voltage cycling and increased SOC differential tests, while the remaining seven batteries were cycled until they reached 100 kAh of charge throughput, which is considered end of testing (EOT). In order to identify capacity and power fade rates, RPTs were performed after the first 10 kAh of

[9] One Ah of throughput is defined as one Ah of charge transfer to or from the battery.

cycling and every 10 kAh until 40 kAh after which, the RPTs were done every 20 kAh until 100 kAh of throughput was achieved. As noted previously, the RPTs consist of both capacity measurement tests at a 1C-rate and HPPC tests.

Both packs show capacity loss relative to the beginning of life value. As shown in Figure 40, which illustrates the average pack capacity, the rate of capacity loss is slightly higher during the first 20 kAh of cycling and then it gradually decreases as the batteries reach EOT. Figure 41 and Figure 42 compare the discharge capacities (normalized to BOL values) of the individual batteries measured during various RPTs to the BOL values.

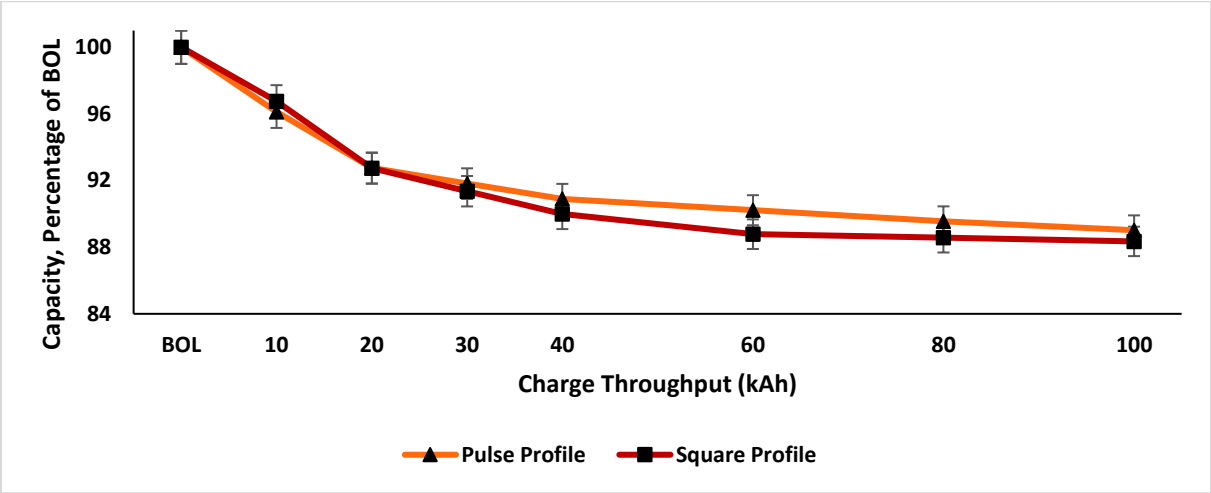

Figure 40: Normalized average pack capacities after cycling

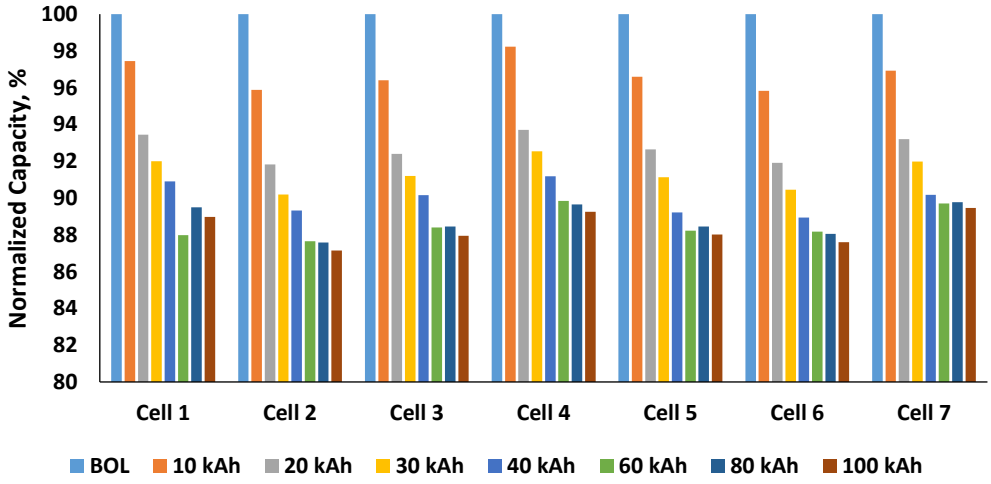

Figure 41: Capacity comparison – Square pack

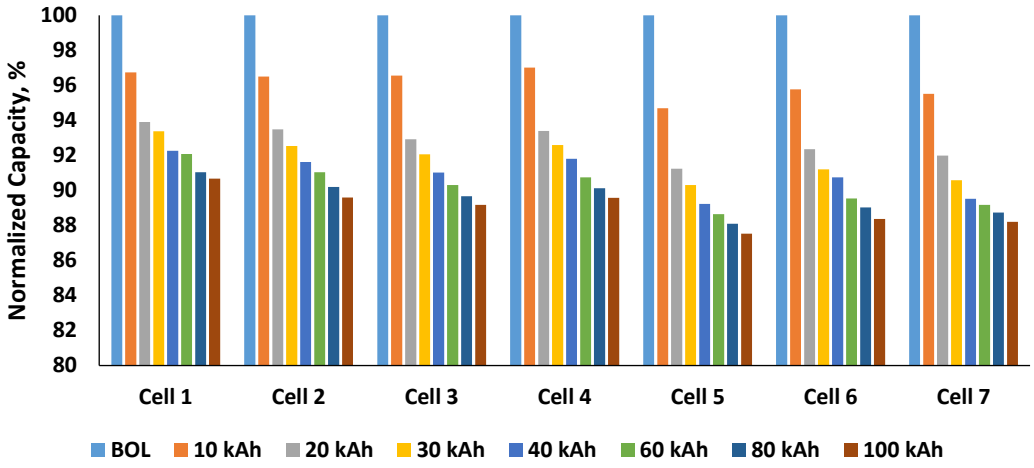

Figure 42: Capacity comparison – Pulse profile

It is clear from the capacity data and the above figures that both packs (square profile and pulse profile) experienced similar amounts of capacity loss between each RPT. At the end of testing, there is less than 1 percent difference in the average capacity between the two packs. We can conclude that for the conditions tested here, the amount of capacity lost by either pack does not depend on the current profile used to cycle them. Though the current profiles are very different in the operational voltage windows and the SOC differential experienced by the batteries (given in Table 2), the amount of charge passing through the two battery packs is the same. **This observation suggests that the charge throughput is the dominant factor that dictates how much capacity is lost and not the profile used. This result also suggests that crude approximations of complex drive cycles can estimate capacity fade successfully.**

5.2.2 HPPC Test Results for Batteries Cycled at 40 percent SOC

The HPPC tests identify any loss in power the batteries experience and provide data for the assessment of the internal resistance of the battery. Figure 43 and Figure 44 compare battery power during the discharge and charge pulse of the HPPC test at BOL and EOT. The HPPC tests show no decrease in the power capability of the batteries as they age. All power values were normalized to the 80 percent SOC 1 second discharge value[10]. This data also predicts that these batteries when

[10] This is the maximum power produced by the batteries during the HPPC test as specified by the test. It is not the maximum power the battery.

used in vehicle applications, can meet the power demand of the vehicle throughout the test period even as the driving range is diminished due to capacity fade.

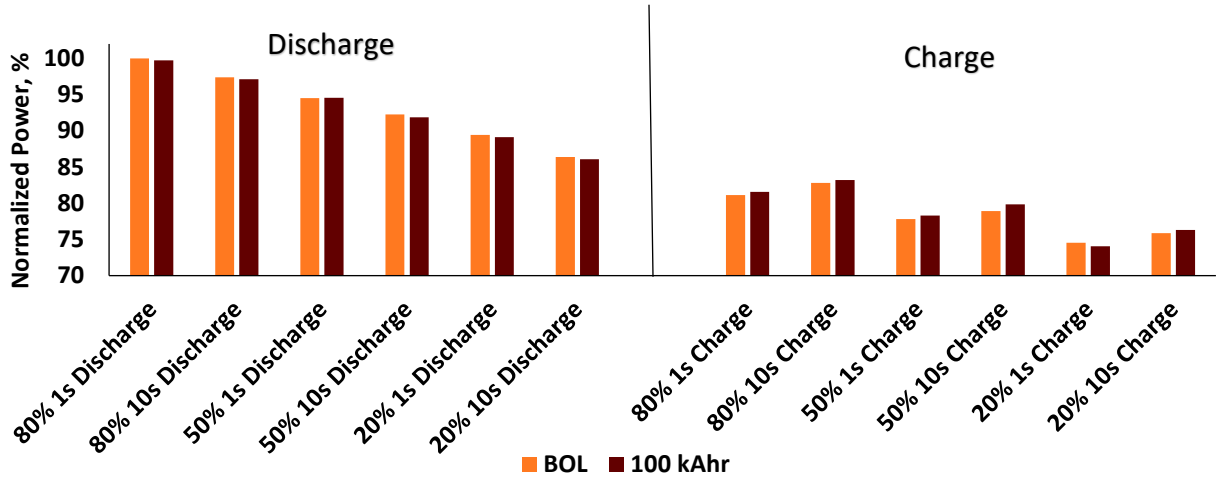

Figure 43: HPPC power comparison – Square profile. Data normalized to 80 percent SOC 1 second discharge = 350W

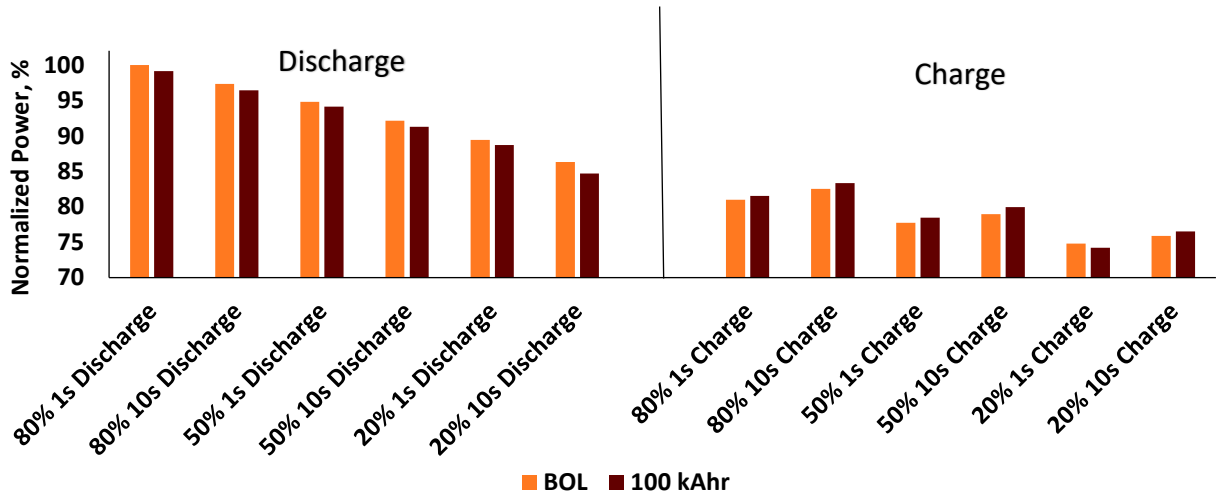

Figure 44: HPPC power comparison – Pulse profile. Data normalized to BOL 80 percent SOC 1 second discharge = 350W

5.2.3 Internal Resistance Change in Batteries Cycled at 40 percent SOC

The internal resistance assessed from the HPPC data is shown in Figure 45. In a lithium ion battery, the SEI on the negative electrode continues to grow continuously through the life of the battery, and this phenomenon is discussed in Chapter 2. However, the growth of the interfacial layer is not

restricted to just the negative electrode and some of the reaction products deposit on the positive electrode as well [90], [126], [31], [33]. These deposits have been identified as a major contributor to the increase in internal resistance of the battery and thus the power fade. Studies, [52], [62] and [91] have identified that high cycling rates tend to increase the internal resistance of the batteries. This trend can be observed in Figure 45. While both packs do show increased internal resistance at the end of cycling, the batteries that were cycled with the pulse profile, i.e., higher rates, show higher internal resistance values compared to the batteries in the other pack, which were exposed to much lower rates and voltages.

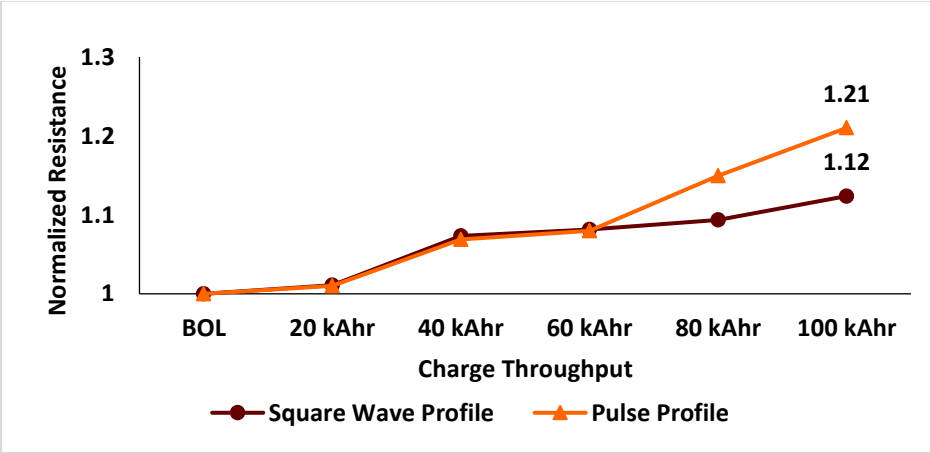

Figure 45: Internal resistance of the battery packs. Data normalized to BOL resistance = 1.8 mΩ

Increasing resistance is typically attributable to increases in the thickness of the SEI as lithium is consumed by side reactions. Likewise, the loss of capacity is frequently attributed to the consumption of cyclable lithium due to these reactions. If lithium consumption were the primary mechanism for both increasing resistance and capacity fade, these two effects should show similar trends. However, here, resistance increases at a greater rate than capacity fades and is accelerated by the pulse profile while capacity fade is slower and is unaffected by profile. This discrepancy suggests other effects beyond simple lithium consumption at the anode may be occurring. Studies have also suggested that there is a layer of reaction products on the positive electrode (similar to the SEI on the negative electrode) that grows continuously over the life of the battery. This layer though less resistive compared to the SEI at BOL grows at a faster rate than the SEI during long term cycling and could potentially exceed the SEI in terms of contribution to the resistance of the

battery [65], [90], and [105]. Additionally, the change in the resistance of a lithium ion battery can also depend on the temperature and the charge/discharge rate used [69], [127], and [128].

Usually, an increase in the internal resistance adversely affects the power capability of the battery. However, the HPPC data does not indicate a significant change in the power capability of the batteries between BOL and EOT. Figure 46 shows the ohmic losses in the batteries as a percentage of the reference power. The results show that, for the power cells tested in this study, the BOL resistance of 1.8 mΩ is so small that even a relatively large increase in the resistance does not lead to a significant change in the charge or discharge power of the battery. For example, the power dissipated as heat due to the battery resistance is 4.70 percent of the reference power at BOL for batteries cycled using the pulse profile. This loss increases marginally to 5.73 percent of reference power at EOT.

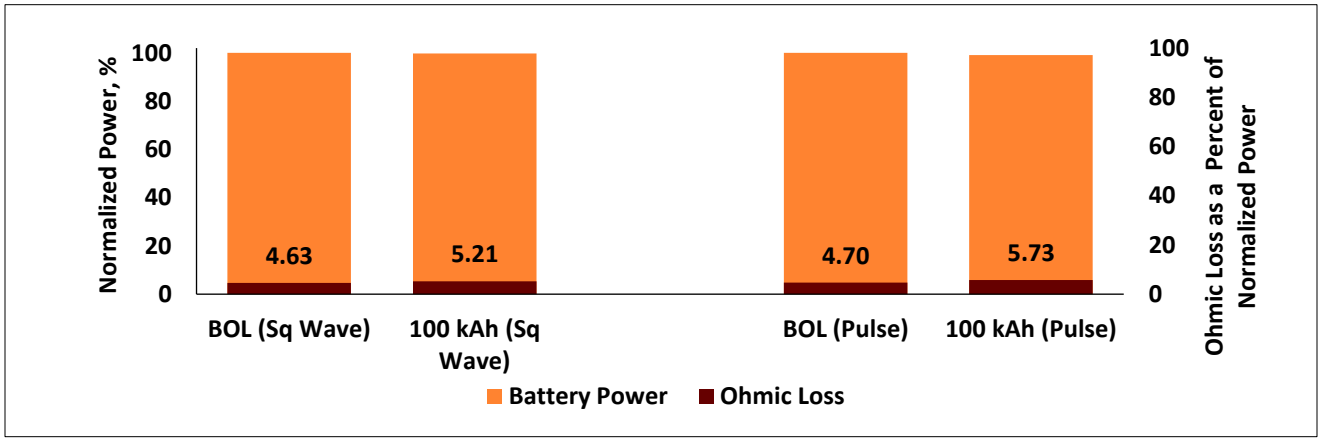

Figure 46: Ohmic losses as a percentage of reference power. Data normalized to 80 percent SOC 1 second discharge = 350W

5.3 Cycling at 60 Percent SOC

5.3.1 Capacity Data from Batteries Cycled at 60 percent SOC

As noted in the experimental methods chapter, four batteries from each pack were removed from the battery pack to undergo cycling under different conditions. Two batteries from each pack were cycled at 60 percent SOC, which shifted the operational voltage window of the batteries higher (Table 2). The capacity fade observed for these batteries is shown in Figure 47. There is an increase in the capacity of the batteries between the time they were removed from the battery pack and the

time they began cycling at 60 percent SOC. Once cycling resumes, the capacity fade follows a trend similar to that as observed in the batteries cycled at 40 percent SOC. The capacity fade values observed at the end of testing for the batteries cycled at 60 percent SOC (with both square and pulse profiles) are identical to each other, as well as being within 2 percent of the capacity fade values obtained for the batteries cycled at 40 percent SOC. This result suggests, again, that the capacity fade is dependent on the charge throughput and not the profile used. This result also confirms that the capacity fade is not dependent on the voltage window within which the batteries cycle during the test period, provided the voltage window remains within the manufacturer's recommendation.

The slight increase in capacity during storage can occur due to relaxation effects [129], [130]. Lithium ions previously trapped in structural defects can slowly undergo non-preferential diffusion to increase the capacity. Considering the similar capacity fade values at the end of testing, we can conclude that the relaxation effects are temporary and have no impact on the long-term capacity fade.

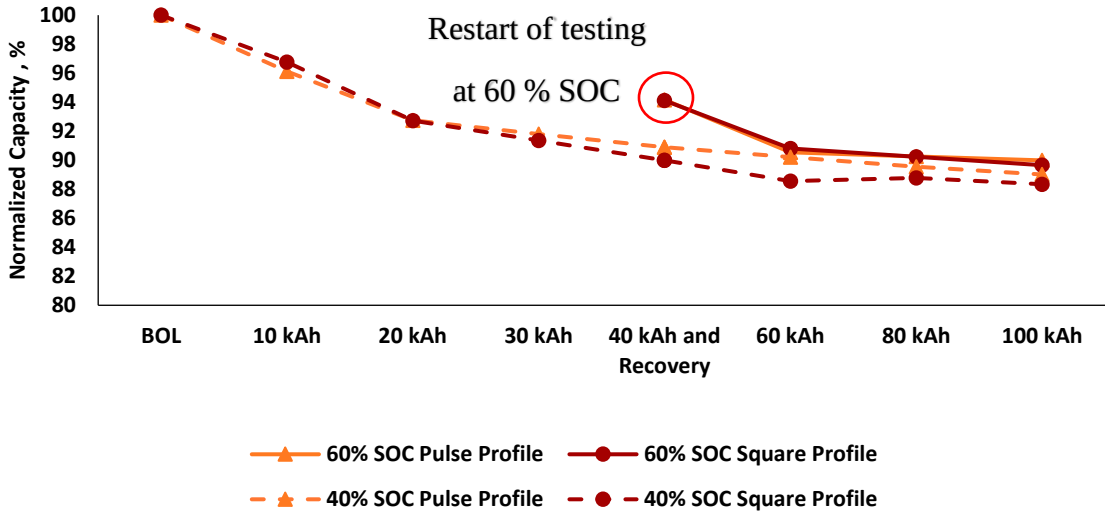

Figure 47: Capacity fade for batteries cycled at 60 percent SOC. Data normalized to average BOL capacity = 4.96 Ah

5.3.2 HPPC Data for Batteries Cycled at 60 percent SOC

The batteries cycled at a higher 60 percent SOC (and correspondingly higher voltage window) exhibited the same power capability from BOL to EOT. Figure 48 and Figure 49 show the HPPC power capability observed for the batteries cycled at 60 percent SOC.

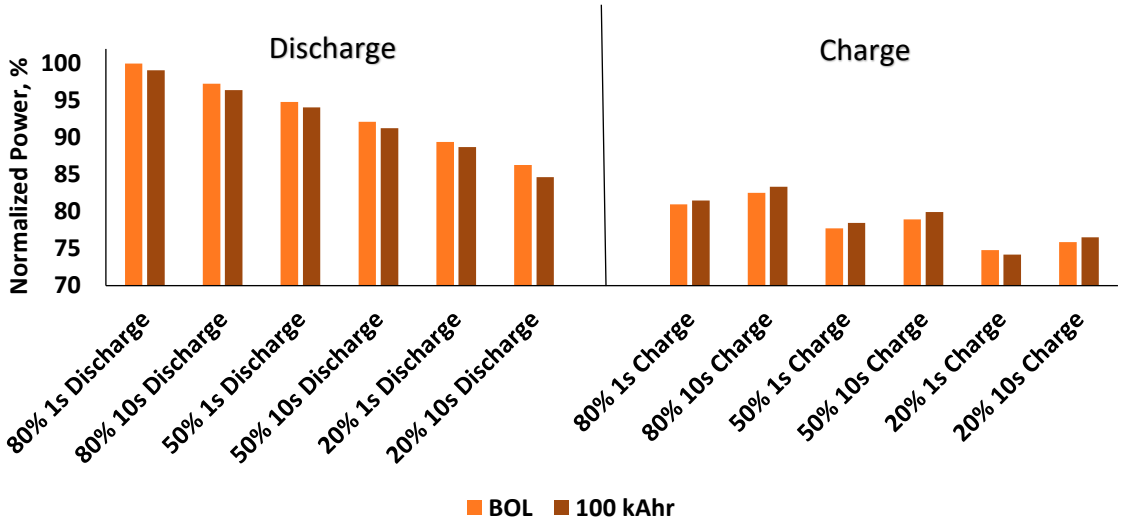

Figure 48: HPPC power data for batteries cycled at 60 percent SOC – Pulse profile. Data normalized to BOL 80 percent SOC 1 second discharge = 350W

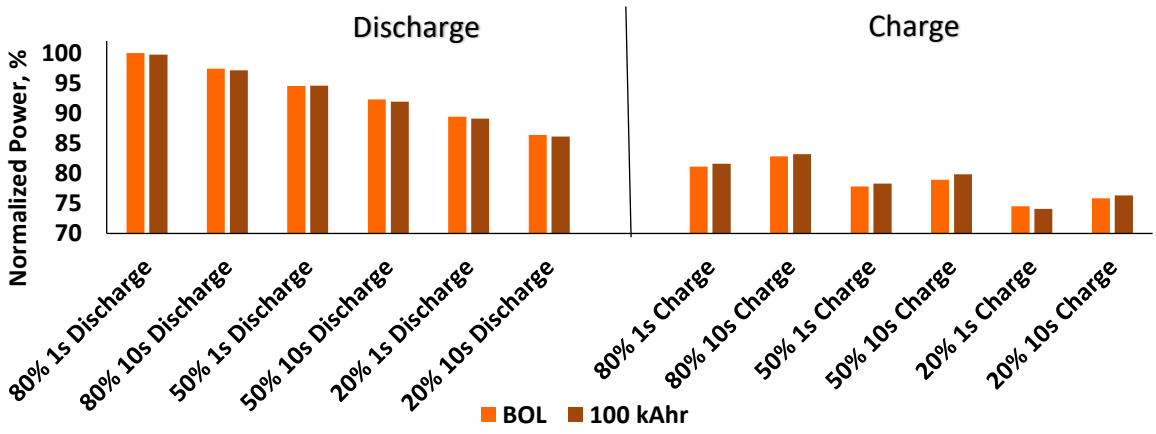

Figure 49: HPPC power data for batteries cycled at 60 percent SOC – Square profile. Data normalized to BOL 80 percent SOC 1 second discharge = 350W

5.3.3 Internal Resistance for Batteries Cycled at 60 percent SOC

The internal resistance change in the batteries cycled at 60 percent SOC is given in Figure 50. The batteries show an increase in the internal resistance when compared to the batteries cycled at 40 percent SOC. However, this increase is more noticeable with the batteries cycled using the square profile than the pulse profile.

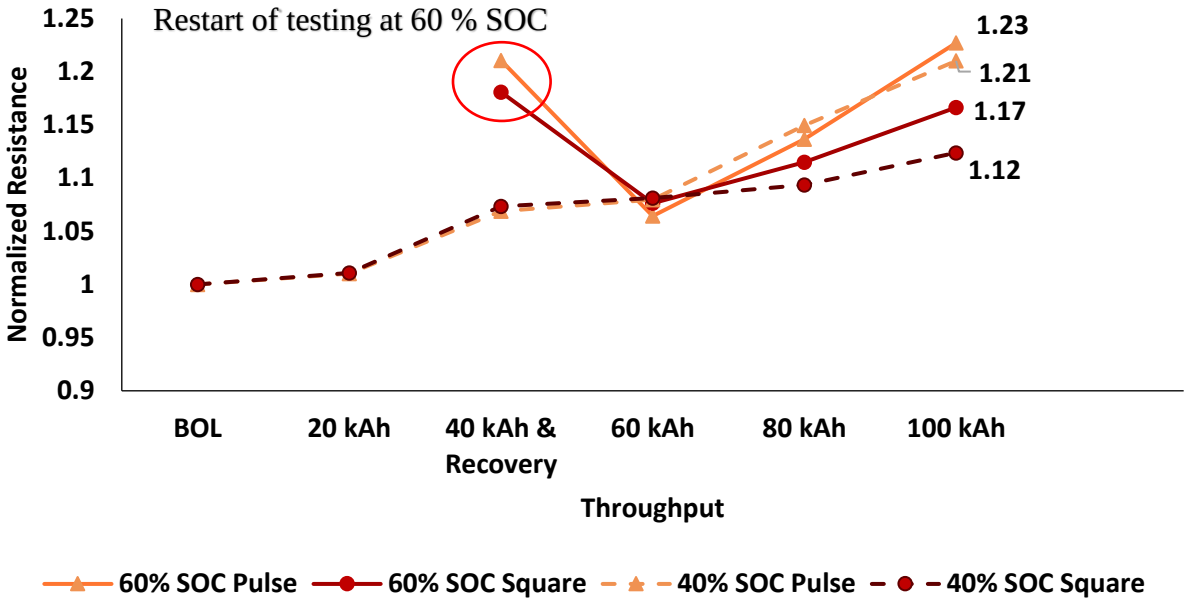

Figure 50: Internal resistance changes for batteries cycled at 60 percent SOC. Data normalized to BOL resistance =1.8 mΩ

Although there was an overall increase in the internal resistance of the batteries as shown in Figure 50, the corresponding increase in the ohmic losses remain negligible. Consequently, this increase in resistance does not have a noticeable impact on the power capability of the batteries as observed during the HPPC tests.

5.4 Cycling with Increased SOC Differential

5.4.1 Capacity data from Batteries Cycled with Increased SOC Differential

Four of the remaining batteries were cycled with increased SOC differential, which exposed the batteries to higher voltages as well as a bigger SOC differential compared to the base case (Table 2). Following the storage period, these batteries exhibit a temporary increase in capacity similar to the batteries cycled at 60 percent SOC, and this is once again attributable to relaxation effects. **The capacity fade experienced by the batteries is similar to the results obtained with the other**

two cycling conditions with the capacity fade remaining within 1.5 percent of the baseline case, thus, reaffirming the conclusion that the capacity fade depends on the total charge throughput and not on the profile used. The capacity fade for the batteries cycled with increased SOC differential is shown in Figure 51.

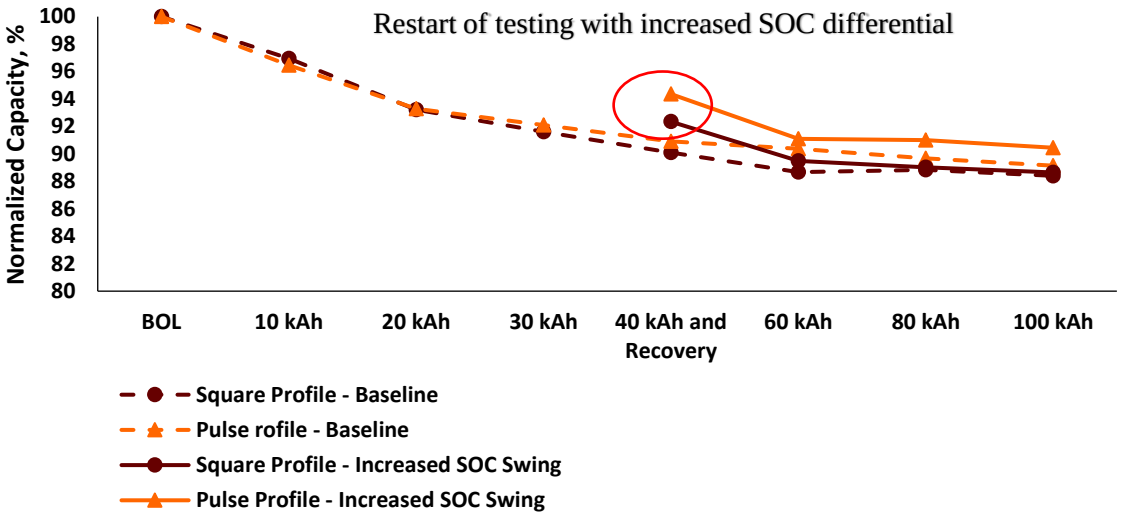

Figure 51: Capacity fade for batteries cycled with increased SOC differential. Data normalized to average BOL capacity = 5 Ah

5.4.2 HPPC Data for Batteries Cycled with Increased SOC Differential

The HPPC power capability results for the batteries cycled with increased SOC differential at EOT (shown in Figure 52 and Figure 53) do not show any significant changes compared to the BOL values, matching the trend that has been observed in the batteries cycled with the other two conditions.

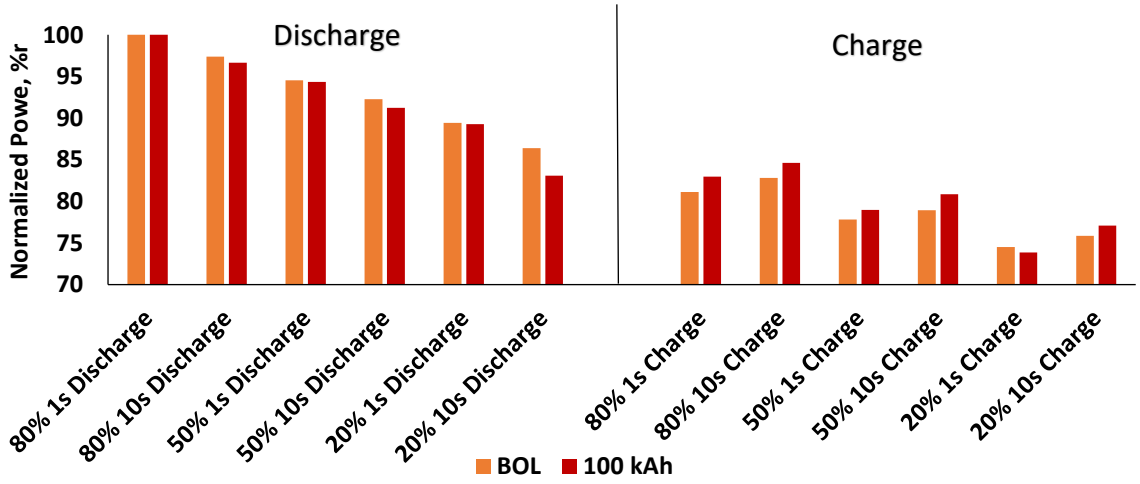

Figure 52: HPPC power data for batteries cycled with increased SOC differential – Square profile. Data normalized to BOL 80 percent SOC 1 second discharge = 350W

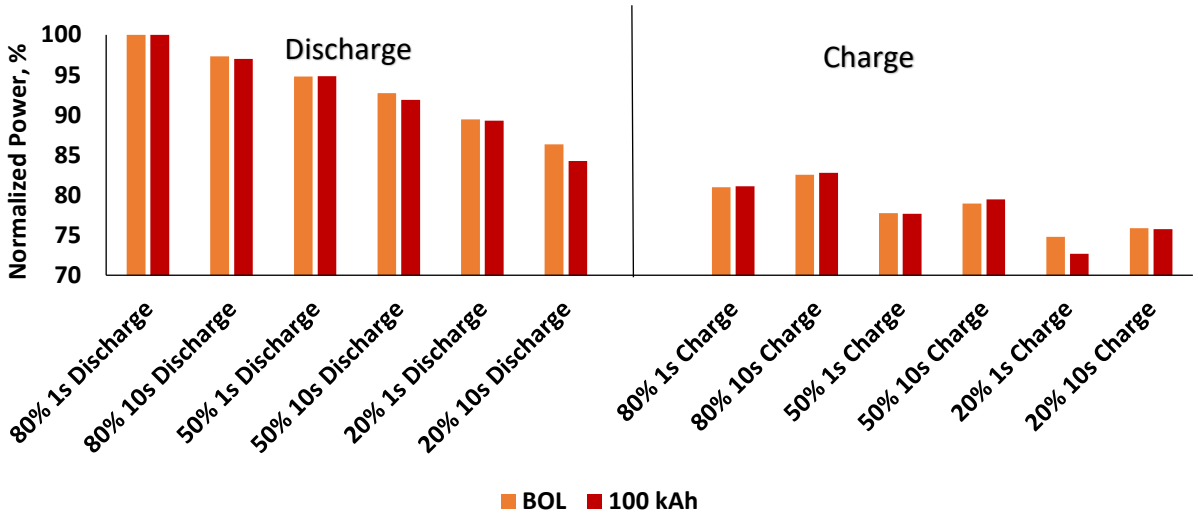

Figure 53: HPPC power data for batteries cycled with increased SOC differential – Pulse profile. Data normalized to BOL 80 percent SOC 1 second discharge = 350W

5.4.3 Internal Resistance for Batteries Cycled with Increased SOC Differential

The internal resistance changes in the batteries cycled with the increased SOC differential profile are shown in Figure 54. The batteries cycled with the pulse profile show the largest increase in resistance, which is similar to the previous cases and the change in in internal resistance for both profiles is almost identical to the previous cases. This suggests that similar processes are contributing to the increase in internal resistance. The absence of noticeable changes in the power capability of the batteries can once again be explained by the relatively small magnitude of the ohmic losses for this battery design.

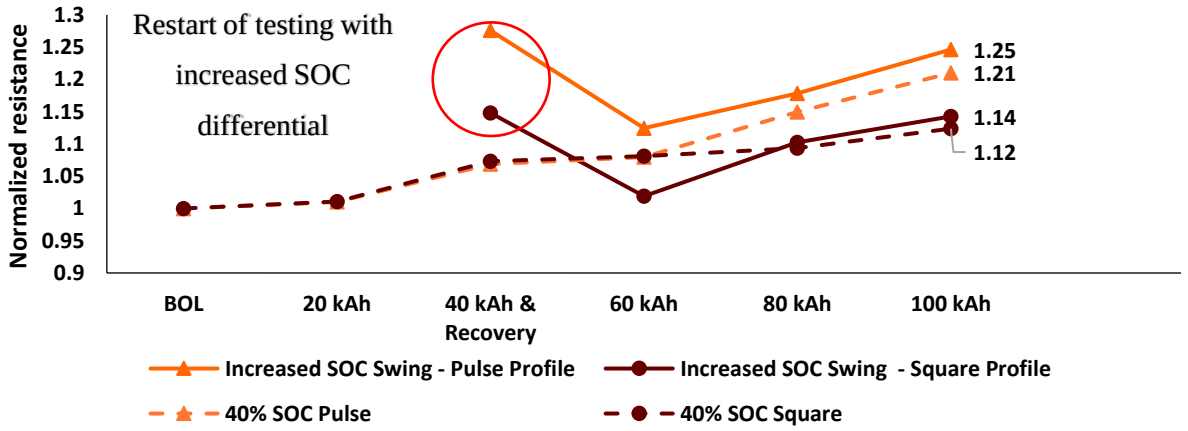

Figure 54: Internal resistance for batteries cycled with increased SOC differential. Data normalized to BOL resistance = 1.8 mΩ

Of the six profiles tested, all exhibit similar capacity fade (~12 percent) and similar power fade (< 2.5 percent). The pulse profile cycles, all of which have voltage excursions above 3.80 V, exhibit noticeably higher increases in internal resistance than the square profile cycles, which stay below 3.80 V. However, for these cells, which are designed for high power and, thus, low resistance, the impact of the resistance increase on power and capacity is negligible.

5.5 Cycling beyond 100 kAh

Cells that underwent cycling with the increased SOC differential were chosen to continue cycling until a combined throughput of 200 kAh was achieved in order to observe the effects of continued cycling on battery fade. The profiles that involved an increased SOC differential were particularly chosen since they had the potential to be the most damaging considering the increased SOC differential as well as the voltages experienced by the batteries.

5.5.1 Capacity Fade from Batteries Cycled until 200 kAh

The capacity fade for the batteries cycled until 200 kAh is given in Figure 55. As shown in this figure, the cells continue to follow a rate of degradation comparable to that observed in the 40 – 100 kAh period from 100 kAh until 200 kAh of throughput. There is once again no significant difference between the pulse and square profiles in terms of capacity fade. This result continues to reaffirm the earlier statement made about the dependence of capacity fade on the charge throughput and not the profile used.

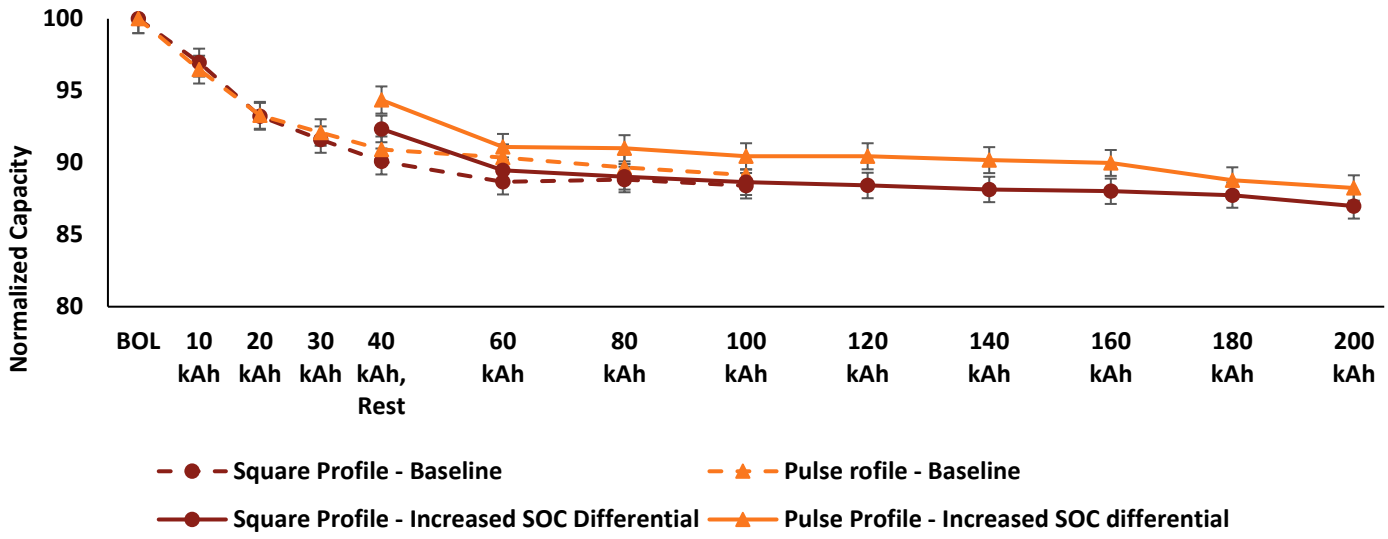

Figure 55: Capacity fade for batteries cycled with increased SOC differential until 200 kAh

5.6 Impact of Calendar Ageing

The average temperature of the cells during cycling was 40 °C. The profiles used in this study have 11.67 Ah of combined throughput per cycle. Considering that the cells cycled for 100 kAh and if the cycling tests were conducted continuously with no breaks for RPTs, operator fatigue, maintenance etc., the time spent by the cells above ambient temperature at 40 percent SOC is ~60 days. Measurements show that the batteries spent the cycling time (60 days) at elevated temperatures close to 40 °C. Lithium ion cells are known to lose capacity at temperatures above ambient and these effects are exacerbated when stored at high SOCs. Some studies report the effects of temperature and SOC on batteries of similar chemistry as this study. For example, [63], [131], [132], [133] all study the effect of SOC and calendar ageing on cells containing NMC. Table 9 shows the capacity fade observed in calendar aging studies with an estimate of capacity lost around the 60-day mark. It can be observed that cells with similar temperature and SOC lost about 2 – 3 percent capacity due to calendar ageing in a similar timeframe as the cycling time in this study. If 2 or 3 percent loss is attributed to calendar ageing effects, there is still 8 or 9 percent of the total loss (out of twelve percent) taken into account. The only other process that has an impact on the battery is the cycling. Consequently, it appears that the cycling process has the most significant impact on the capacity fade of these cells and that calendar ageing has a somewhat smaller impact on the capacity fade.

Table 9: Calendar aging studies with a summary of results

Reference	Cell chemistry	Cell capacity (Ah)	Test SOC (%)	Test duration (weeks)	Test temperature (°C)	Capacity loss reported at EOT (%)	Approximate capacity loss after 60 days (%)
[61]	LCO	0.68	N/A	3	50	6	N/A
[132]	NMC	0.5	60	65	45	20	5
					35	7.5	2.5
					50	10	4
					30	4	1.5
					40	10	2.5
					50	21	5.5
					60	45	17
			95			7.5	3.5
			80			6.5	2.5
			60			5.6	3
			40			3.6	1.3

Results from Coin-Cells

5.7 results from Cycled Cells

5.7.1 Capacity Fade

Reference performance tests were conducted on the coin cells before start of cycling as well as regularly throughput the cycling process. The RPTs consisted of a capacity test, and an EIS test to identify any changes to the cell resistance. The RPTs were repeated every 100 cycles starting from BOL until EOT (1000 cycles). Sixteen cells with similar capacities (average capacity of 1.2 mAh and a standard deviation of ±0.1 mAh) were chosen at random for cycling, and four cells were randomly assigned to each of the test profiles (described in Chapter 3; 3.3.3 Cycling tests). Figure 56 shows the average capacity for cells in each profile as a percentage of the BOL capacity over the duration of testing. Regardless of the profile used, the cells exhibit a similar trend in capacity fade. A higher rate of loss is observed during the first few hundred cycles followed by a gradual decrease in capacity to around 70 percent of BOL after 1000 cycles. The trend observed with the coin cells is similar to what was observed in the commerical cells (an intial rapid decline followed by a gradual decrease in capacity). The results observed in the coin cells confirm that the profile used did not have a significant impact on the capacity fade. Once again, the results suggest that charge throughput is more significant factor than cycle profile in determining the capacity loss. Though the trend in the capacity fade shares similarities with the commercial cells, the capacity

loss observed in the relativley short test period with the coin cells is almost three times what was observed in the commerical cells. However, the coin cells were not expected to mirror the specific behaviour of the commercial cells and the observed difference in the capacity fade between the two types of cells is a reflection of the material selection and the build quality of the commercials cells.

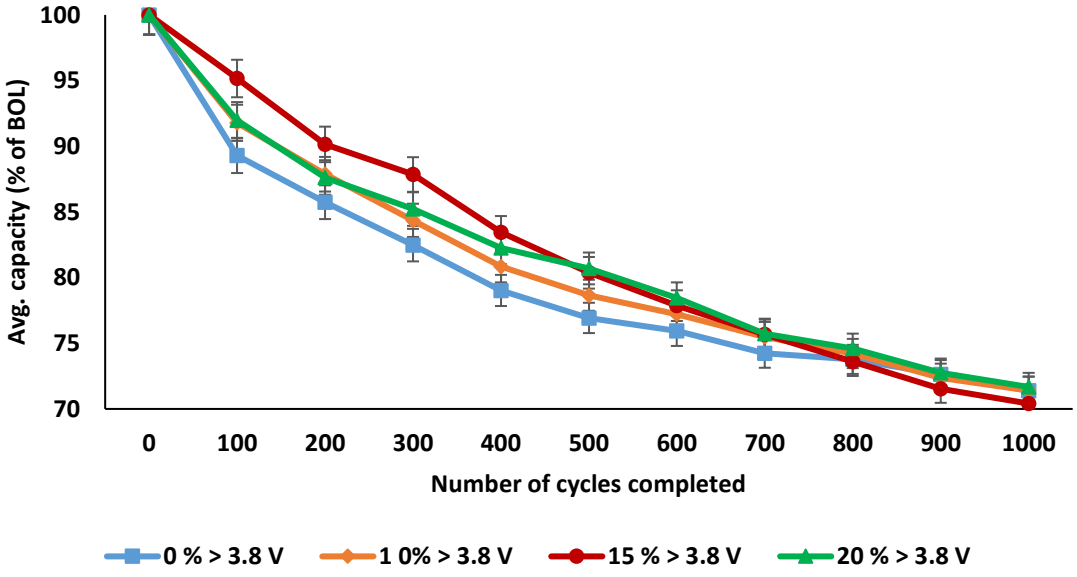

Figure 56: Capacity loss of coin cells compared to the number of cycles

5.7.2 Changes in Resistance

As noted earlier, the RPTs also include an EIS test. Usually in an EIS test, the voltage response of a cell is studied when subjected to an AC current signal with varying frequencies. Figure 57 shows a typical Nyquist plot derived from EIS tests. Generally, the resistance of a cell (Ω) is the x- axis intercept of the semi-circle near the origin obtained by fitting a circle in the Nyquist plot as shown. The difference between the points where the circle intercepts the *x*-axis is considered the polarization resistance of the cell. It is often convenient to consider the area specific resistance ASR in Ωcm^2; when comparing results from different batteries. In this study, the positive electrode area was used to normalize all EIS obtained resistance data.

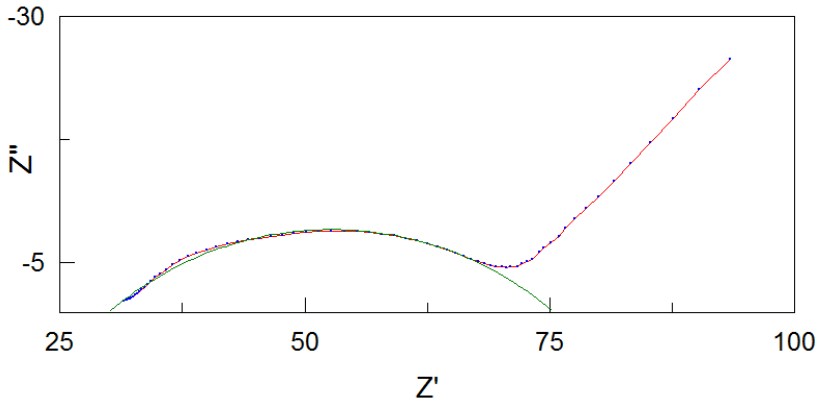

Figure 57: Nyquist plot obtained from the EIS test of a coin cell and a circle fit to the data

Figure 58 shows the relative change in the resistance for all profiles over the duration of cycling. All the coin-cells exhibit a minimal increase in the resistance over the course of cycling. However, as the cells progress to EOT, it can be noted that the cells cycled with a profile that expose the batteries to voltages in excess of 3.8 V display a slightly higher increase in the resistance compared the baseline case.

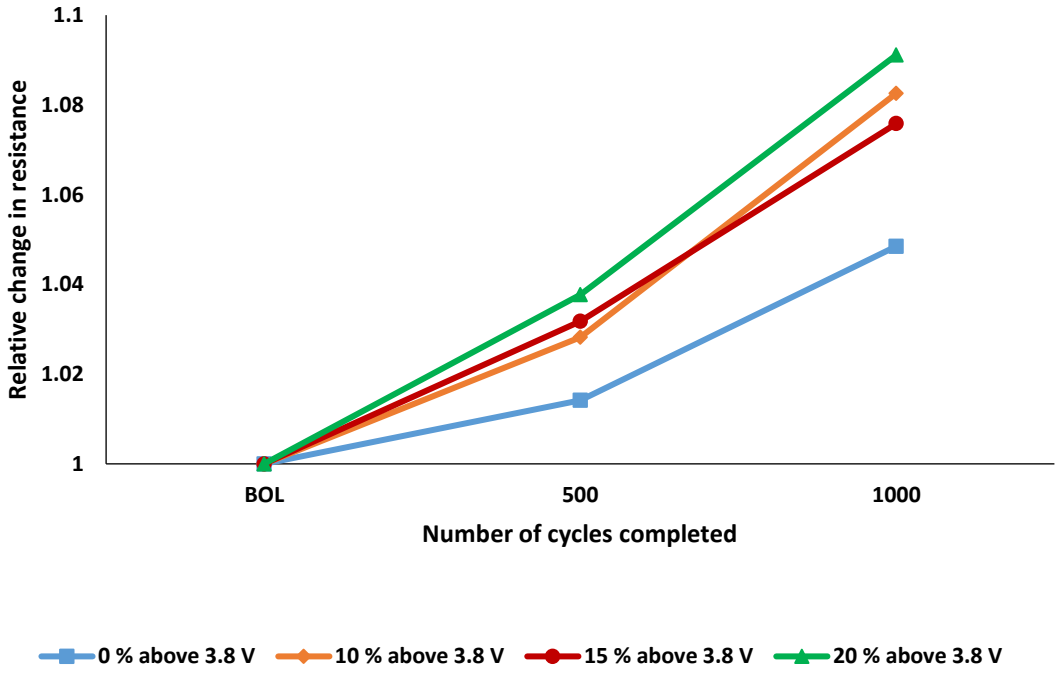

Figure 58: Change in resistance of the coin cells as determined by EIS tests

The profiles that exercise the batteries in excess of 3.8 V exhibit an increase in resistance between 5.8 and 6.5 percent while the baseline case exhibits an increase of only 3.2 percent. This result also mirrors the results noted in the commercial cells (Figure 45) wherein, the cells exposed to higher voltages displayed slightly higher increases in resistance.

5.7.3 Analysis Plots

Figure 59 shows the differential voltage curves and Figure 60 shows the incremental capacity curves for the coin cells tested with all four profiles. It can be seen that all the cells exhibit similar changes to the analysis curves as they age, indicating similar degradation mechanisms.

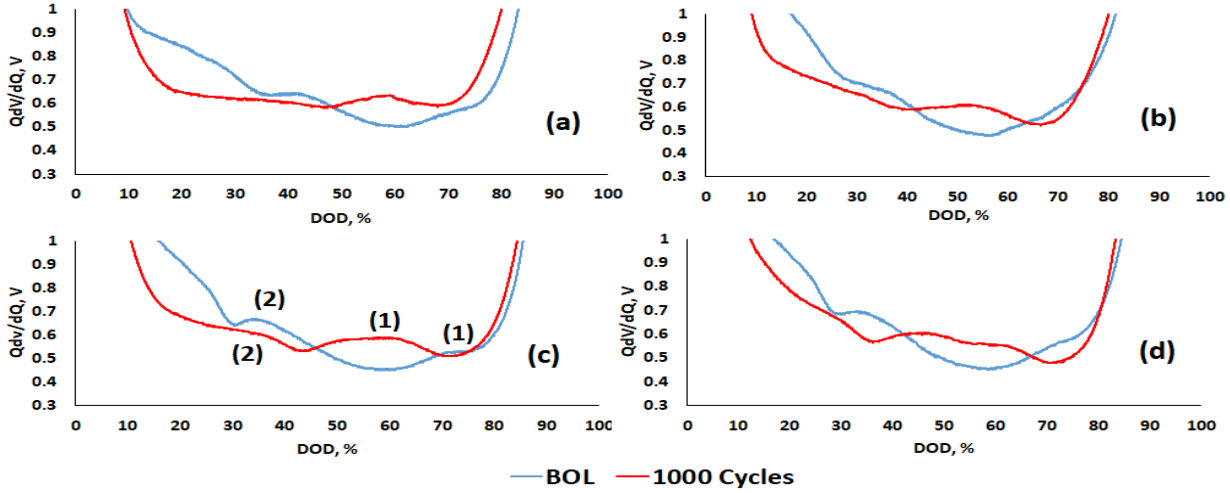

Figure 59: Differential voltage curves for cell that spent, (a) 0 % time above 3.8 V, (b) 10 % time above 3.8 V, (c) 15 % time above 3.8 V and (d) 20 % time above 3.8 V

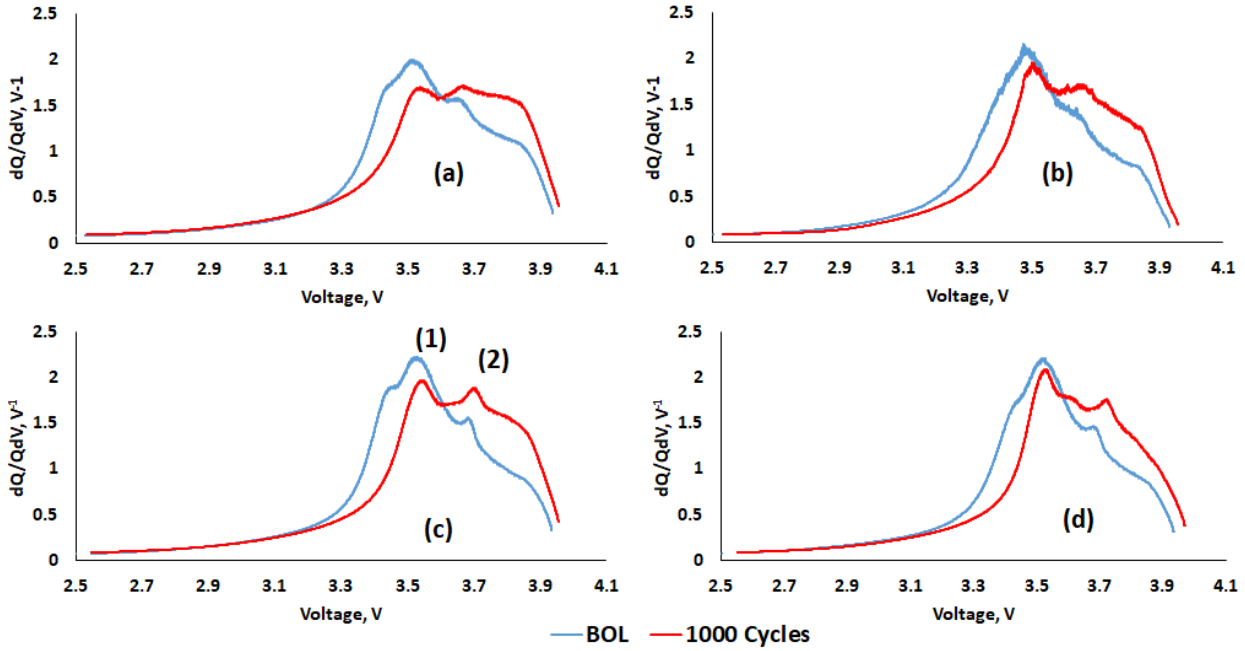

Figure 60: Incremental capacity curves for cell that spent, (a) 0 % time above 3.8 V, (b) 10 % time above 3.8 V, (c) 15 % time above 3.8 V and (d) 20 % time above 3.8 V

The changes observed in the analysis curves shown in Figure 59 and Figure 60 can give clues as to what degradation mechanisms affect the batteries. From the differential voltage curves, it can be seen that the small peak near 70 percent DOD (peak 1) has shifted to lower DOD ~60 percent and the peak near 35 percent (peak 2) has changed in magnitude and shifted slightly to towards lower depths of discharge. Generally, a shift in peak locations and change in magnitude can be due to loss of lithium (LLI) and loss of active material (LAM) respectively [106], [132], and [134]. From the incremental capacity curves, it can be seen that for all cases, there is a broadening of the entire dQ/dV curve and both peaks (peak 1 and peak 2) have changed in intensity. Literature suggests that the broadening of the entire spectrum can be attributable to changes in the electrodes (LAM). It can also be noted that the peaks have shifted to higher voltages indicating loss of lithium (this can arise from the shift in the working SOC range of the electrodes due to loss of lithium). The changes observed to both the differential voltage and incremental capacity curves (changes to peak magnitudes and shift in peak locations) suggest that loss of active material and loss of lithium to side reactions to be the degradation mechanisms. However, these curves do not indicate a dominant mechanism or in other words, do not suggest the extent to which each mechanism contributes to the loss observed. On an interesting note, the difference between the analysis curves

generated from the coin cells (Figure 60) and ones obtained from the commercial cells (Figure 26 and Figure 27) confirm that though both types of cells have an "NMC" electrode, the actual ratios of the nickel, cobalt, and manganese maybe different and thus, the chemistry of these electrodes are different.

5.7.4 Microscopy Analysis of Cycled Cells

The use of coin cells also allows for other post-mortem analysis including microscopy and spectroscopy techniques such as SEM-EDS, ion beam milling, TEM etc. The electrodes from coin cells were carefully disassembled in a glove box and washed with DMC to remove surface contaminants and then were studied using spectroscopy techniques. Imaging of the electrodes via SEM (Figure 61) did not yield useful information regarding loss of active materials. However, the loss of active material is not restricted to changes in particle size[11] due to repeated insertion and de-insertion of lithium. Even small shifts in particles or growth of surface layers can disconnect an electrode particle from the electrical pathway to the current collector. Without this pathway, the particle is rendered useless as an active reaction site due to the inability of an electron to travel to it in order to take part in the electrochemical reaction. The loss of active material noted in the half-cell tests combined with the analysis of the SEM images indicates the loss of electrical contact in the cycled electrodes.

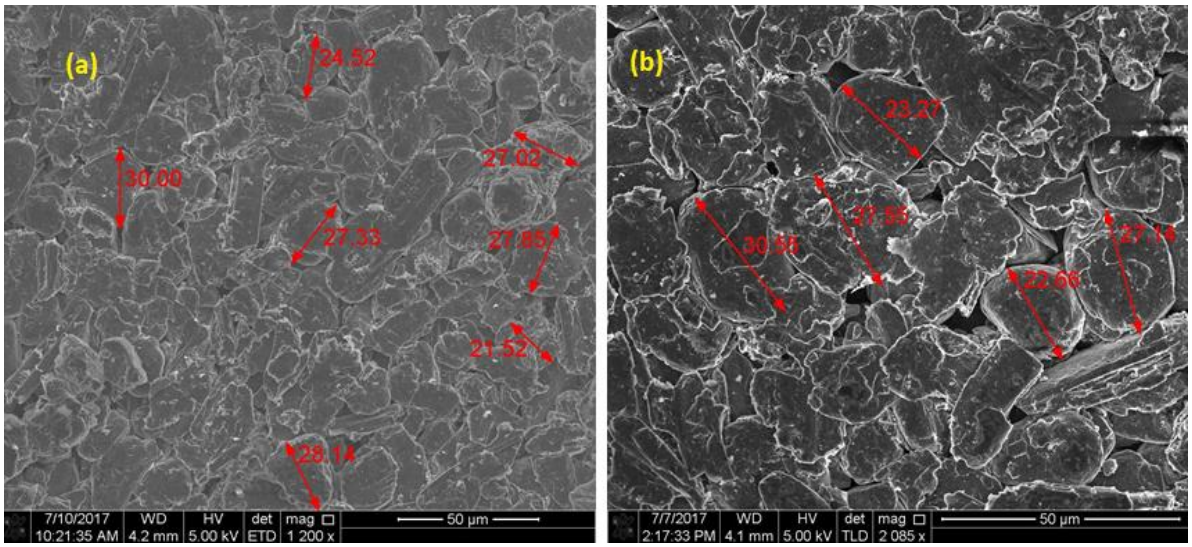

Figure 61: Particle size using SEM for (a) formed but uncycled negative electrode, and (b) cycled negative electrode

[11] Particle size was measured using an open source image processing software ImageJ/Fiji [141]

A focused gallium ion beam was also used to mill away the surface of the electrode particles in order to study the SEI. The results indicate the presence of not one but two separate layers on top of the graphite particle (Figure 62). The layer closest to the bulk carbon is around 100 nm in thickness suggesting that it is the SEI resulting from the formation cycles. The second layer on top is around 35 nm in size and is observed on the negative electrodes of the cells cycled with all the profiles. This layer is thought to be formed due to deposition of reaction products of lithium consuming side reactions. The similarity in thickness of this layer confirms similar degradation mechanisms between these two profiles once again suggesting that the profile is not as important to capacity fade as the charge throughput. SEM-EDS was also used in order to assess the presence of manganese on the surface of the cycled negative electrodes, which could be indicative of manganese dissolution from the positive electrode. However, the data was deemed too noisy and there was interference from the signal characteristic of the element fluorine, which is present in both the electrolyte salt and the PVDF binder used in the electrode fabrication.

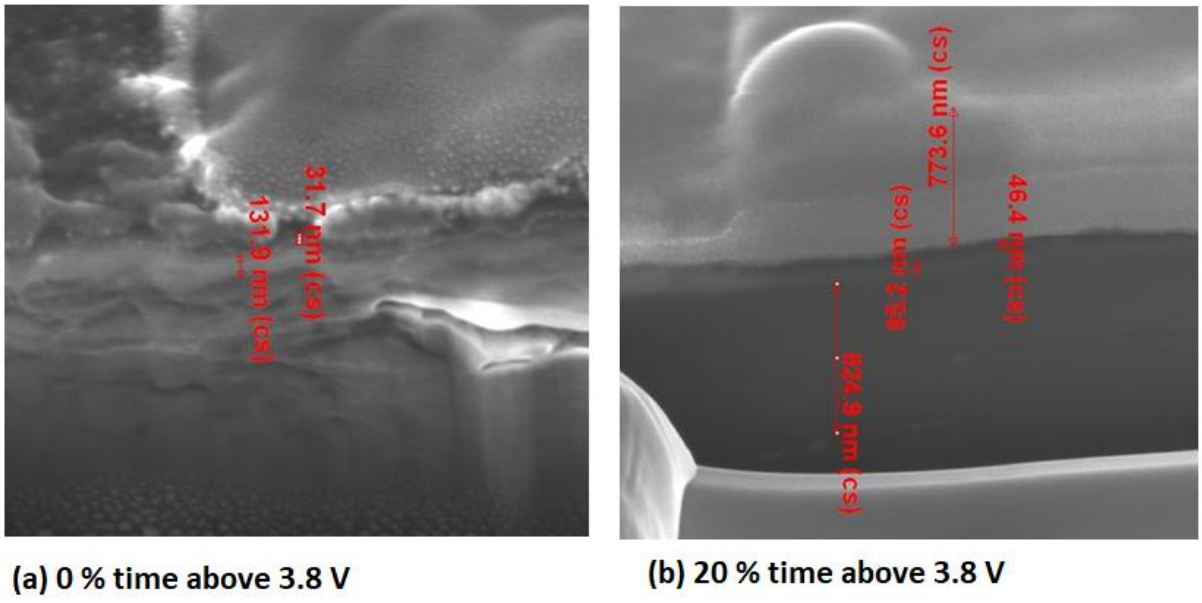

Figure 62: FIB analysis images for (a) 0 percent time above 3.8 V, and (b) 20 percent time above 3.8 V

5.8 Results from Cells Held at High Voltage

5.8.1 Capacity fade

The average capacity fade for the cells that underwent ageing at high voltages without any cycling is given in Figure 63. It can be observed that the cells lost an average of 20 percent of the BOL capacity after 30 days of continuous exposure to voltages in excess of 3.8 V. This is less than the

capacity fade that was observed with the coin cells that were cycled using profiles that exercised the batteries to voltages above 3.8 V.

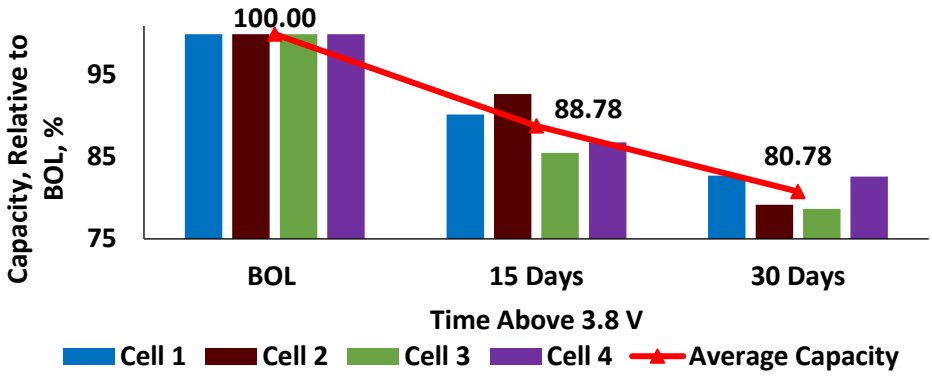

Figure 63: Capacity of coin cells held above 3.8 V over a period of 30 days

5.8.2 Resistance Change in Cells Held at High Voltage

The resistance of the coin cells held at high voltage is given in Figure 64. In just a month, when held at room temperature and at voltages in excess of 3.8 V, these coin cells exhibit increases to resistance on the order of 25 percent.

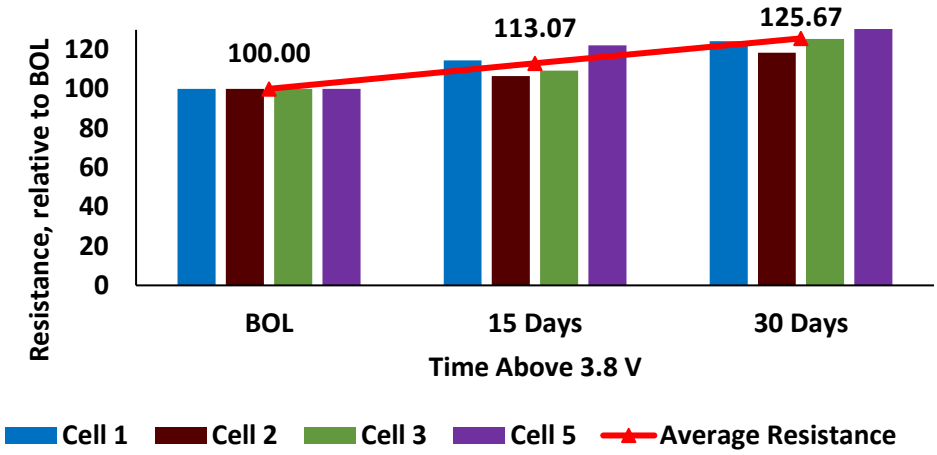

Figure 64: Resistance of coin cells held above 3.8 V over a period of 30 days

Additionally, these cells were exposed to high voltages (that promote lithium-consuming reactions) only for a fraction of the overall test time. Consider the case with the maximum time spent at high voltages i.e. the profile that exercises the batteries to voltages above 3.8 V for 20

percent of the cycle time. This cycle exposes the batteries to no more than 1.4 days[12] during which voltages are beyond the before mentioned 3.8 V threshold. Figure 65 shows the capacity fade as a function of time spent above 3.8 V. It can be observed that the cells that were cycled exhibit a 28 percent loss in capacity after 1000 cycles, which includes 1.39 days spent above 3.8 V. over a similar time-period, the cells held at high voltage lost only about 2 percent of their BOL capacity. Even over a 30-day hold at high voltages, the uncycled cells lost only 20 percent of their capacity compared to a 28 percent loss in only 1.4 days for the cycled cells. Thus, the contributions to degradation from high voltages during cycling appear to be minimal while the losses due to charge throughput are dominant. This observation supports the loss of active material as the dominant degradation mechanism.

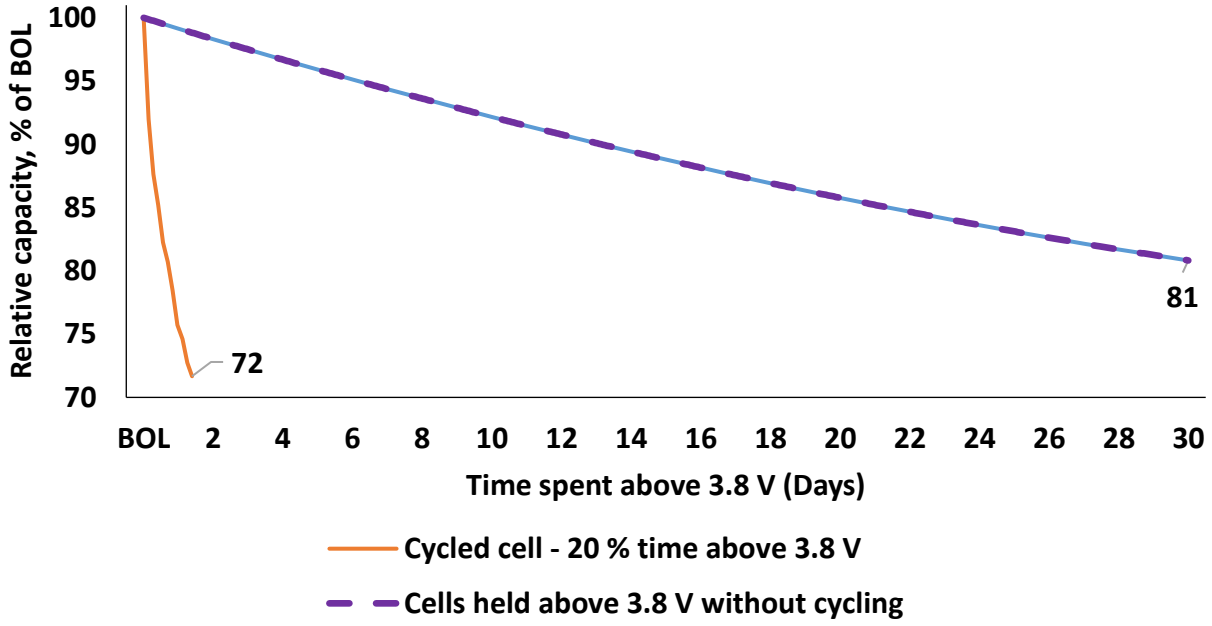

Figure 65: Capacity loss comparison between cycled cells and cells held at high voltage without cycling, based on number of days spent above 3.8 V

5.9 Results from Half-Cells

The differences in the capacity fade can be further explored by studying half-cells made from the tested cells. Pristine electrode samples and electrodes obtained from the tested cells were cycled

[12] Twenty percent of thousand cycles with once cycle lasting ten minutes
Cycling time does not include RPT time

against a reference electrode (lithium metal) in order to study changes to the individual electrodes. It can be assumed that while cycling the electrodes against a reference lithium metal counter electrode, loss of lithium due to side reactions (LLI) is negligible as pure lithium metal can be considered a pseudo-infinite source of lithium ions. Therefore, it is reasonable to assume that any losses observed in the capacities of the half-cells has to originate predominantly from changes to the electrodes themselves, i.e. degradation of active material. When testing with lithium counter electrodes, under certain conditions such as high current densities (greater than 1 mA/cm^2), a shift in the potential of the lithium metal can occur over time due to the formation of the SEI and solvated electrons [135], [136]. This can occur with two electrode or with three electrode setups. In this study, the current used to cycle the half-cells resulted in a current density of around 0.15 mA/cm^2 (calculated based on lithium electrode diameter), which is an order of magnitude smaller than the current density observed to cause a noticeable change in the potential [136]. Thus, any shift in the lithium potential that may have occurred during the testing of half-cells due to the SEI formation can be considered negligible and can be safely ignored.

Figure 66 shows the capacities of the individual electrodes before and after cycling. Both the graphite and NMC electrodes of cycled cells have lost similar relative amounts of capacity after 1000 cycles. The amount of capacity lost by individual electrodes is also similar with the overall capacity fade observed for the full cell (dashed line). Comparing the electrodes from the cells held at high voltage, it is seen that graphite has lost around 11 percent of the original capacity and the NMC has lost around 5 percent. In contrast, the full cell lost close to twenty percent at EOT.

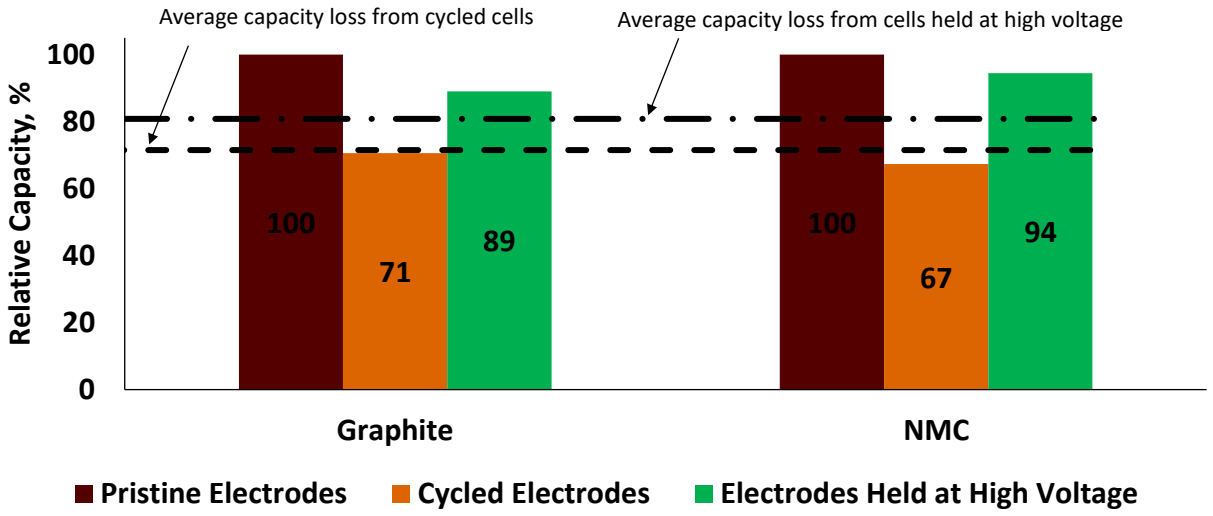

Figure 66: Electrode capacities before and after cycling

Comparing the capacity lost by full cells held above 3.8 V and the corresponding loss in the individual electrodes (20 percent vs. 11 and 5 percent), it can be concluded that the loss in the capacity of the full cell is due to side reactions consuming lithium. The discrepancy between the capacities of the full cell and individual electrodes indicates that the lithium is being consumed in side reactions without extensive changes to the electrodes, i.e., the electrodes still retain the active areas/sites for the reactions to occur but, the lithium is no longer present in a cyclable form leading to capacity loss.

In the case of the cycled cells, both the half-cells and the full cell exhibit similar amount of capacity loss (~30 %). The similarity in the observed capacity loss indicates that the active areas/sites have sustained damage that results in loss of capacity. Though there could have been some loss of lithium inventory, the data suggest the primary degradation mechanism when cycling is present is the loss of active material.

Results from the Model

5.10 Commercial Cell Degradation based on Model

There are some situations where the dismantling of the batteries in order to conduct any type of post-mortem analysis is not feasible. For example, manufacturing techniques, components used etc. may be covered under intellectual property, trade secrets etc., which are at risk of exposure during the dismantling process. Though post-mortem analysis could provide more accurate measurements for some physical parameters and properties needed for the model, reasonable

assumptions about these parameters can be made either from observing the behavior of the battery or by reviewing literature data. During the development of this model, the latter approach was used with the commercial cells, since explicit permission for post-mortem analysis was not available. The primary purpose of the model as discussed in chapter 4 is, to identify the capacity fade mechanisms by comparing analysis curves generated by the model with experimental data. In order to accomplish this purpose, the model must be capable of successfully capturing the voltage response of the battery to a wide range of currents and must do so over the life of the battery with only a few parameters requiring modification. The model was initially developed by using parameters found in literature [4], [67], [75], and [86], in order to establish a rudimentary working model. The analytical solution to the model was then used to predict the voltage response to a range of discharge currents from 1C to 15C. This effort led to the development and validation of the sub-program that calculates the concentration gradient across the electrolyte (as shown in Figure 35, Chapter 4), and the resulting voltage drop.

Figure 67 shows low rate (C/33, 1C, and 2C) discharge curves as predicted by the model using the analytical solution. This study was key in establishing the SOC differential of each electrode during operation as well as identifying reasonable estimates of capacity related parameters such as current collector area and BOL active material fractions for each electrode. Considering that these batteries were designed to operate under very high cycling rates (48C during discharge and 36C during charge), it is reasonable to assume that values for diffusion coefficients and reaction rate constants for each electrode obtained from literature will have very little effect on the results generated by the model under very low cycling rates. With this assumption, estimates for capacity related parameters as well as the SOC differential of each electrode were studied and changed until the model-generated data agreed with the experimental data.

Once the capacity related parameters and the SOC differential for each electrode was established, a study was conducted to evaluate reasonable values for the diffusion coefficients and reaction rate constants for each electrode. At higher C-rates, these parameters play a key role in establishing the overpotentials and thus the battery voltage. Though the battery is capable of C-rates of up to 36C (discharge), discharge rates of 5C, 10C and 15C were chosen to establish the parameter values since the majority of the cycling is at rates at or below 20C.

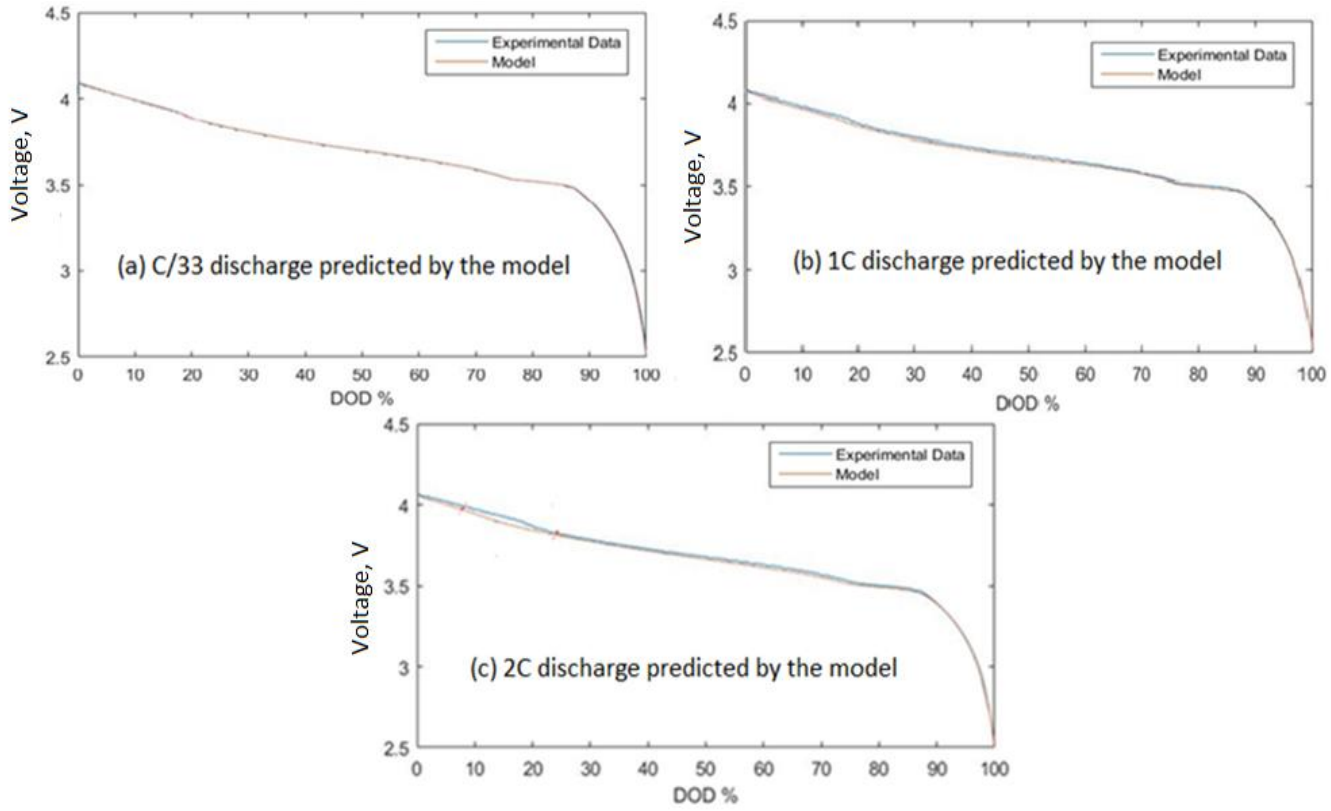

Figure 67: Relatively low rate discharge curves predicted by the model using the analytical solution

Additionally, this parametric study involved discharging the battery at these high C-rates for different SOCs. The kinetic overpotential of the electrode particle is directly related to the concentration of lithium on the surface. At high C-rates, and high SOCs the excess of lithium on the surface of the electrode particles can shut down the reactions and cause the battery to reach the limiting voltage. By studying the diffusion coefficients and kinetic-rate constants at different SOCs, the effect of lithium concentration in the particle on the model behavior was studied and the model output was matched with experimental data in order to obtain reasonable estimates of the diffusion coefficient and kinetic-rate constants that work well across a range of C-rates and SOCs. The model predictions and the experimental data for different C-rates and SOCs are shown in Figure 68 and Figure 69 .

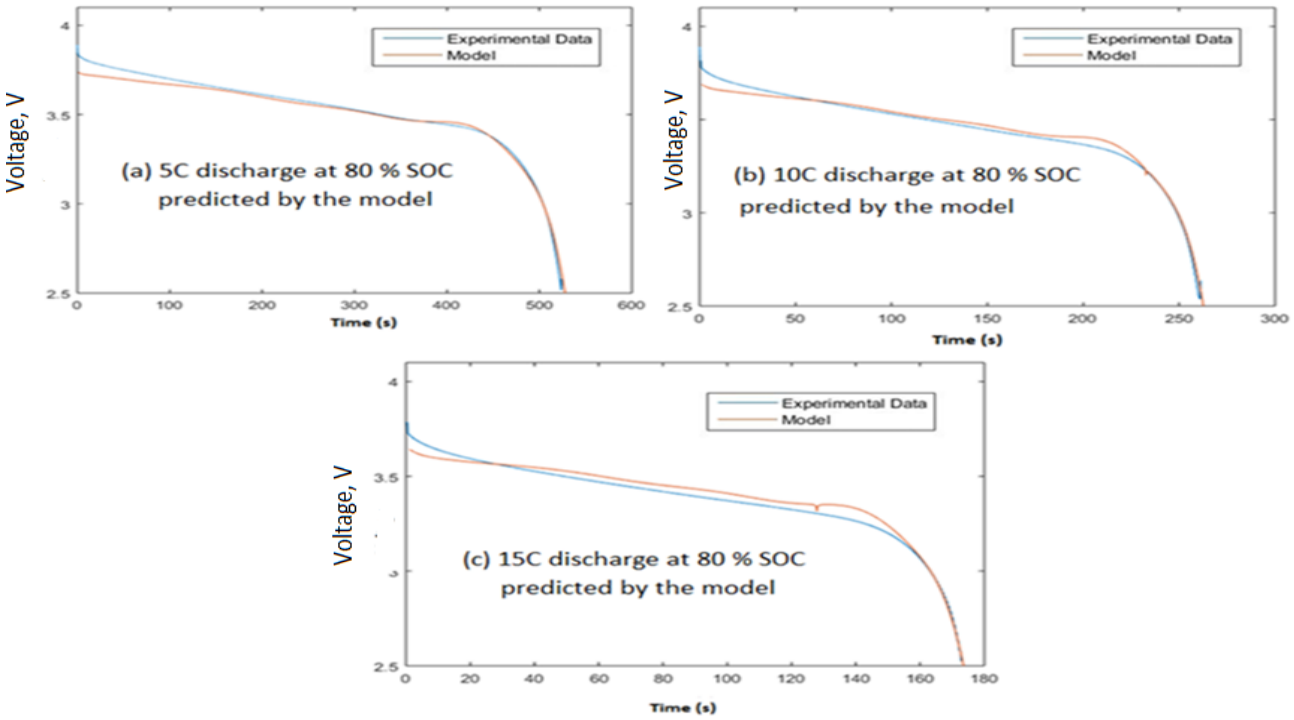

Figure 68: Comparison of model predictions and experimental data for high rate discharge at 80 percent SOC using the analytical solution

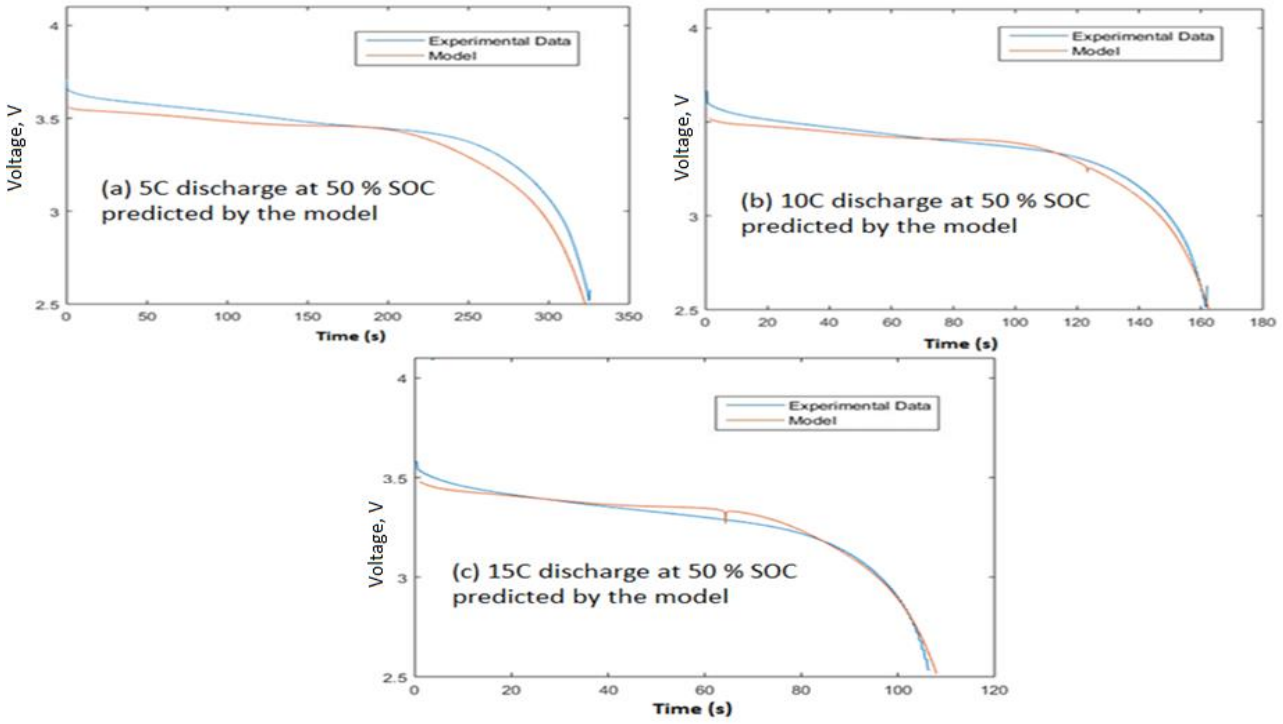

Figure 69: Comparison of model predictions and experimental data for high rate discharge at 50 percent SOC using the analytical solution

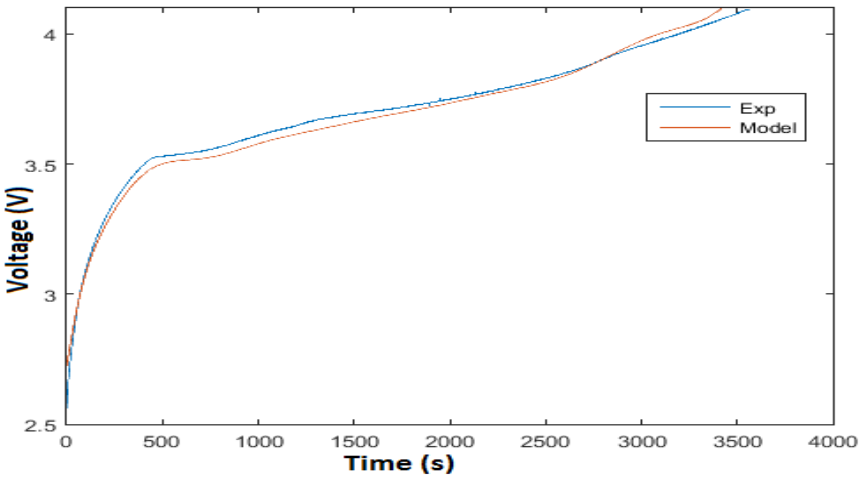

Figure 70: 1C charge data predicted by the model using analytical solution

The model, in addition to predicting the discharge behavior, must predict the charge response of the battery. This ensures that the parameters used in the model are valid for all operational conditions and consequently that the model can be used to predict the battery response to complete cycles. The voltage response predicted by the model for a 1C charge is shown in Figure 70.

Over the course of development of the model (based on the analytical approach), certain parameters were found to have a significant impact on the model output. For example, the active material fractions had a major impact regardless of the C-rate used. This behavior is to be expected as the active material fraction directly contributes to the capacity as well as other derived values such as current density, interfacial area etc. The solid phase diffusion coefficient, another major parameter has very little impact at low C-rates. However, at higher rates, it acts as one of the reaction limiting parameters and thus its value was carefully studied and selected.

In addition to the solid phase diffusion coefficient, the liquid phase diffusion coefficient was also carefully selected in the model in order to get accurate predictions of battery behavior. The concentration gradient in the liquid phase has a significant impact on the voltage response of the battery. An observation made during the development of the model was, the accuracy of the voltage change observed immediately following an applied current is sensitive to the liquid phase diffusion coefficient used. This observation can be explained by studying (Eq. 4.23) where, the first term on the right side of the equation is an ohmic loss term and depends only on the physical dimensions of the battery (which remain constant) and the applied current. However, the concentration term in the latter part of the equation is directly dependent on the diffusion

coefficient used. Thus, the resulting voltage drop across the electrolyte due to the concentration gradient can be significantly affected by the diffusion coefficient value.

During a constant current charge or discharge process, the initial concentration distribution in an electrode particle can be taken as uniform. However, in reality, the operational mode of the battery can randomly change between charge and discharge and the lithium distribution inside the electrode particle can no longer be considered uniform. In addition, the boundary condition at the electrode particle surface can also change with the operational mode. Thus, as noted in section 4.4, the analytical solution was superseded by a finite difference approach that accounts for varying boundary conditions and non-uniform initial conditions. The various parameters studied in the analytical approach were used as a starting point for the finite difference model.

Any finite difference approach requires the discretization of the spatial and time variables used in the problem and the accuracy of the method is dependent on the quality of the mesh used. In other words, the number of grid points used to discretize the spatial variable (r in this case) and time (t) affects the accuracy of the predictions. This indicates that the use of a large number of grid points (a fine mesh) would produce the best result possible. However, increasing the number of grid points also increases the computing time. There is a point where further increases in the number of grid points leads to minimal improvement in accuracy and unacceptable computing time. In order to identify an optimized grid resolution in the spatial variable and in time, a grid resolution study was conducted. Figure 71 shows the voltage response to a C-rate of 36 predicted by the model using different grid resolutions.

The number of grid points in the r direction has no significant impact on the accuracy of the model for the range of values indicated in Figure 71. However, for $\Delta t = 0.2$ s, a Δr value below 0.033 μm leads to instability in the PDEPE solution method. Therefore, the final Δr value was fixed at 0.066 μm. The number of time steps per second has a more noticeable effect on the accuracy of the model. However, minimal gains in accuracy were found after five time steps per second or $\Delta t = 0.2$ s, which was adopted for the model.

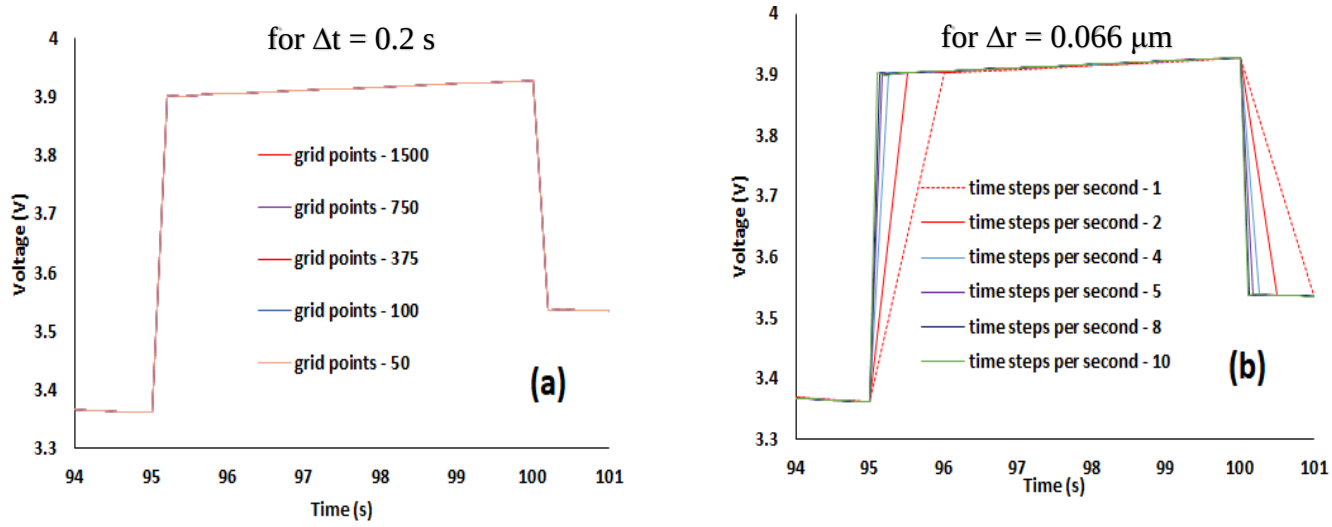

Figure 71: Grid independence study for (a) "r" - direction and (b) time

In order to verify the accuracy of the finite difference approach, the 1C discharge prediction was compared to the experimental data after the grid-resolution study as illustrated in Figure 72. It can be observed that the experimental data agrees well with the prediction from the finite difference approach.

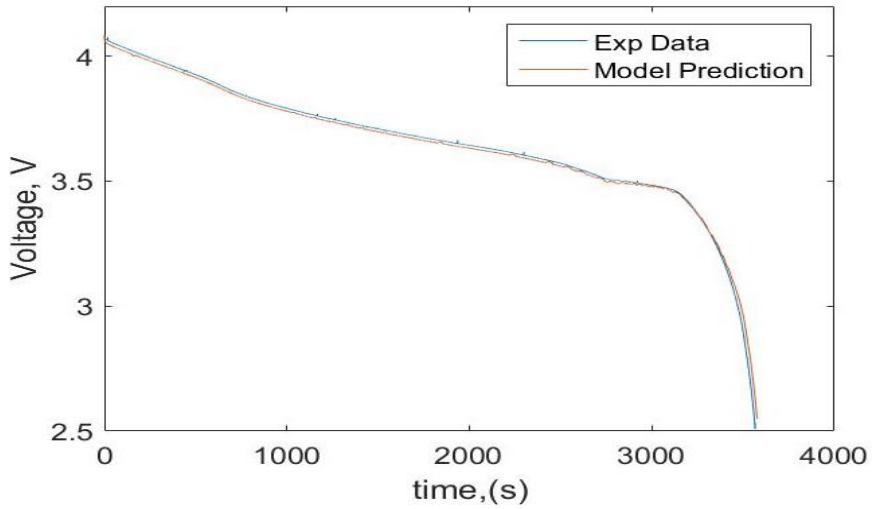

Figure 72: Model predicted 1C discharge behavior using finite difference method

Once the constant C-rate behavior was predicted, the finite difference approach was used to predict the battery response to the pulse profile used to cycle the cells as shown in Figure 73. As this figure illustrates, there is good agreement with the experimental data except at extremely high C-rates

(greater than 30C). At such high rates, the model under predicts the charge behavior and over predicts the discharge behavior by a small margin.

The extent of the variation between the model and experimental data was also studied to establish the accuracy of the model. The difference between the measured voltage response of the battery and the model prediction is shown in Figure 74. At all points during the cycle, the difference in voltage is less than 80 mV and majority of the voltage predictions (96 percent) lie within 15 mV of the experimental data. Such small differences in the prediction of the battery behavior can be considered negligible and the parameter values (Table 8) estimated by methods discussed in earlier sections and implemented in the finite difference model allow it to predict the battery behavior in an accurate manner.

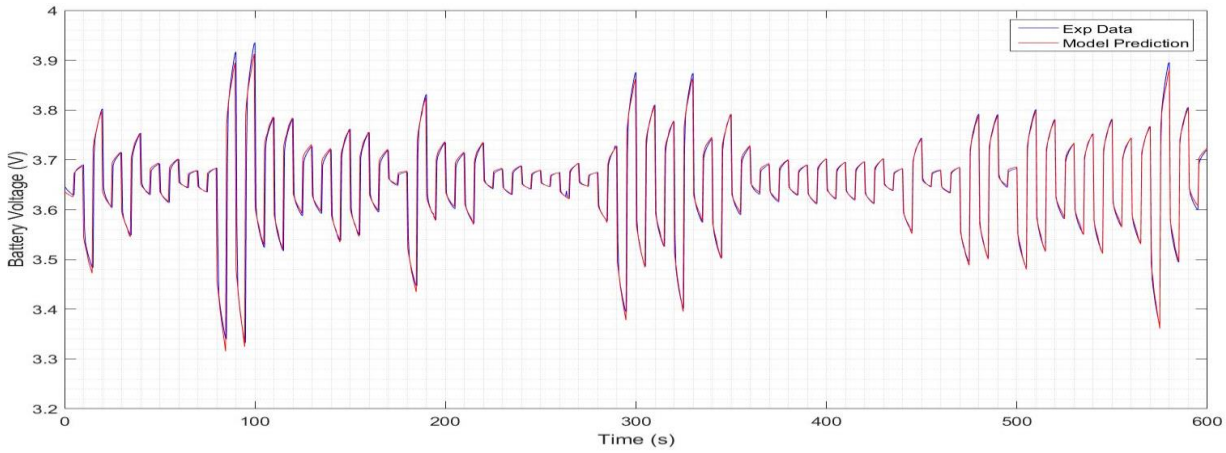

Figure 73: Pulse profile voltage prediction using PDEPE approach

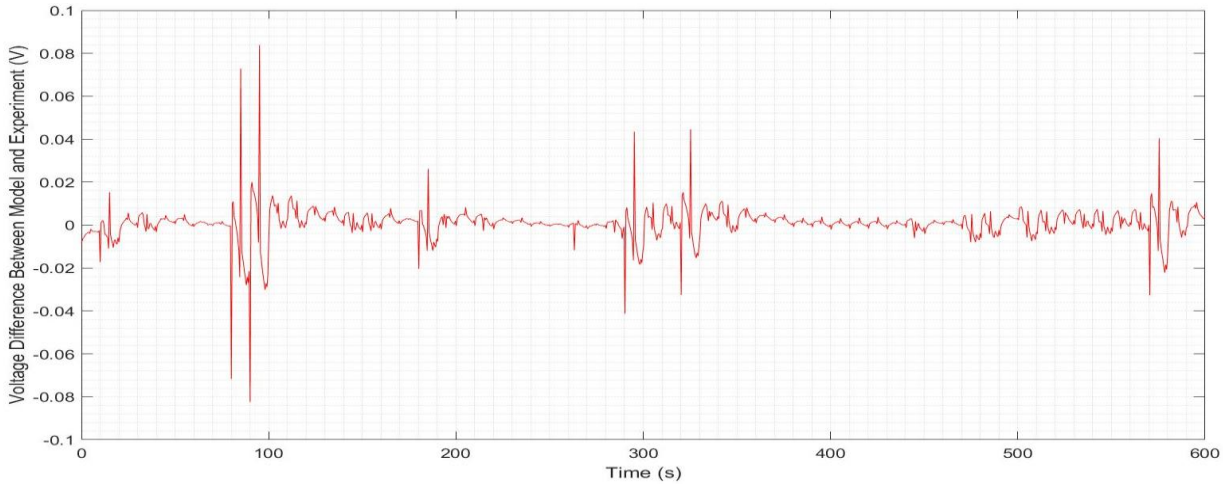

Figure 74: Difference between the voltages predicted by the model and experimental results

The differential voltage and incremental capacity analysis methods (discussed in section 4.1.3) can be used with the data generated by the model to analyze the key capacity fade mechanisms. Chapter 2 discussed the details of various degradation mechanisms observed in lithium ion batteries. In this work, two mechanisms are under consideration for the commercial cells.

(1) *Loss of cyclable lithium* often referred to as the loss of lithium inventory (LLI). This mechanism includes the lithium ions (hence capacity) lost due to consumption in decomposition reactions and continued SEI growth. These ions are subsequently not available for cycling between the electrodes, leading to a loss in capacity. Usually, the loss of lithium due to continued SEI growth and side reactions can be observed as a shift in the working range of the electrodes towards less lithiated states [106], [132], and [137]. An example is illustrated in Figure 75 where, the OCP of the electrodes are plotted against the relative concentration of lithium in them. The operating ranges of both electrodes shift towards a less lithiated state compared to beginning of life. Considering that the battery voltage limits remain the same during the life of the battery, a loss in lithium due to side reactions will result in a shift in the operating range of the electrodes and consequently each electrode will continue to cycle through a progressively smaller ΔSOC window as the battery ages.

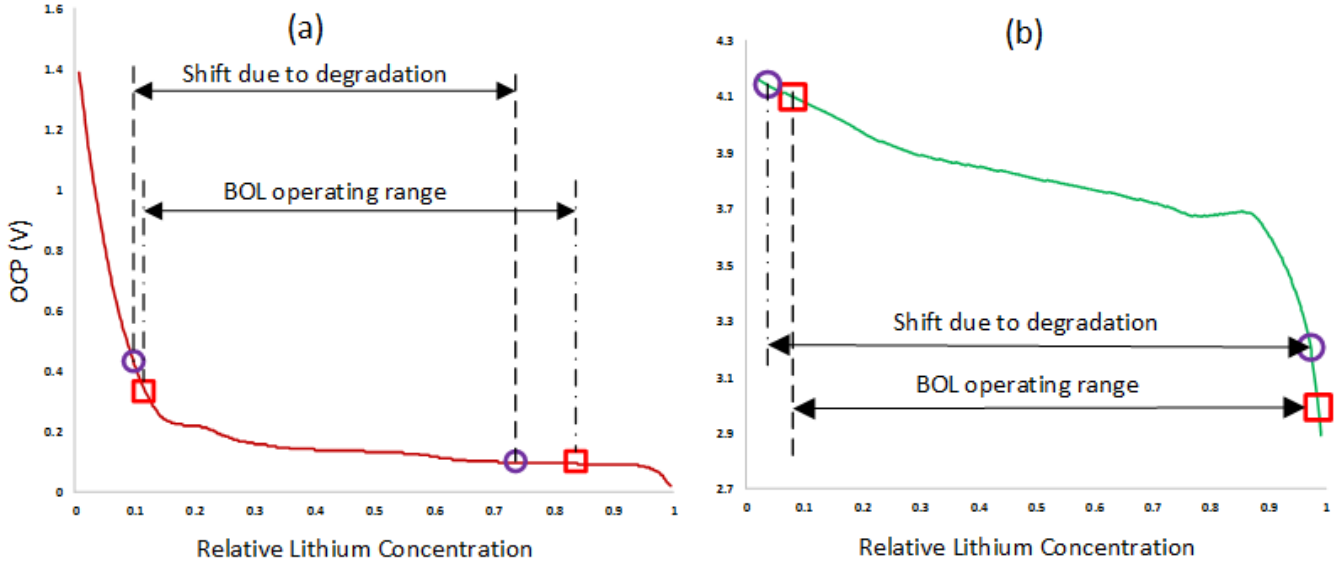

Figure 75: Shift in electrode working range (a) negative electrode, (b) positive electrode

Consider case ‘a’ in Figure 76, the lithium (visualized in blue) goes from the graphite to the NMC during discharge. When the cell is fully charged the cell voltage is given by the difference in the OCP of the electrodes; in this case it is 4.2 – 0.1 = 4.1 V. Similarly, when the cell is fully discharged, the cell voltage is given by 3.3 V – 0.6 = 2.5 V. Now consider that some of the lithium is consumed in side reactions and deposits around the negative electrode particle visualized by the orange shaded area in Figure 76 b. Now, when the cell is being discharged, the positive electrode has not reached the same SOC as in case (a) when the negative electrode reaches the same SOC as case (a). Considering that the limiting voltages of the cell remain the same over time, discharge will now have to be extended in order to reach the limiting voltages. This leads the graphite to be discharged to even lower SOCs and the positive electrode increases in SOC until the limiting voltage is detected. This phenomenon is applicable to the charge process also and this leads to the observed shift in the operating range of the electrodes when lithium is consumed in side reactions.

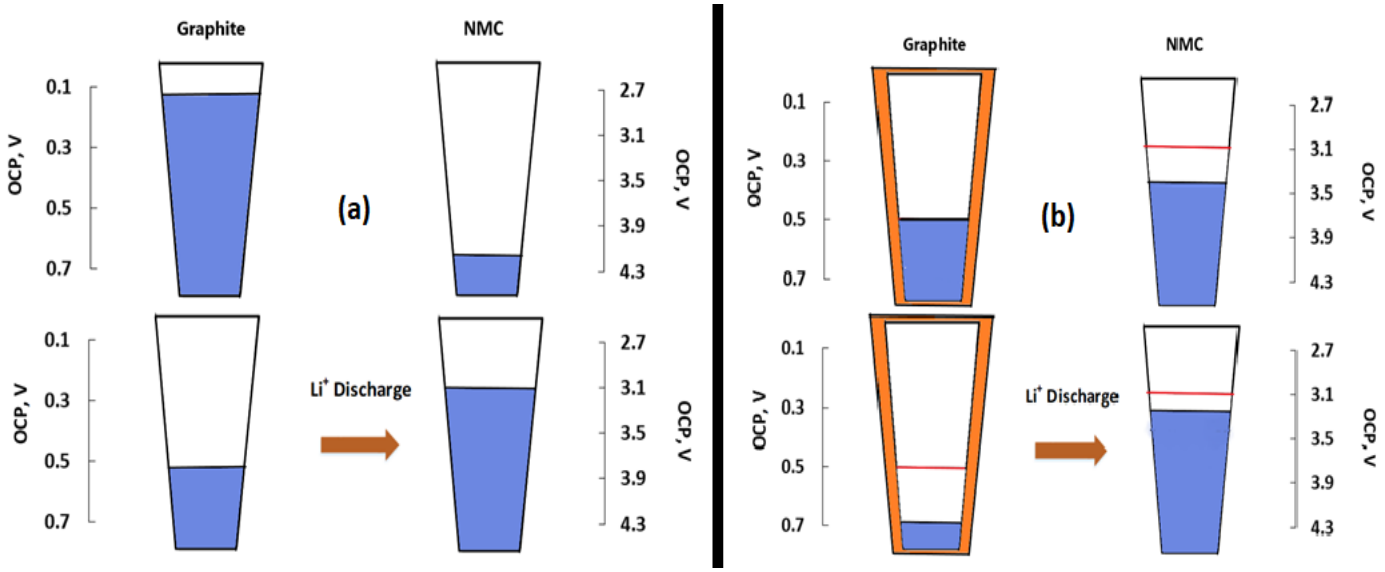

Figure 76: Visualizing shift in the SOC range for LLI

(2) *Loss of active material* (LAM) from either of the two electrodes. In case of the graphite negative electrode, as the battery ages, the active material may no longer available for lithium insertion due to loss of electrical contact, cracking, binder decomposition or blockage of active sites by side reaction products. In the case of the positive electrode, the LAM mechanism can occur due to transition metal dissolution into the electrolyte solvent (a common occurrence in electrodes containing manganese), structural reordering of planes, binder decomposition and loss of electrical contact between the material and the current collector. Consider the discharge process of a fully

charged battery and consider that the positive electrode has lost a certain percentage of the available active areas due some combination of the previously mentioned mechanisms. The lithium ions now travel from the negative electrode to the positive. Now, the overall rate of flow of lithium ions into the positive electrode remains the same as before the degradation. However, there are fewer active electrode particles capable of receiving the lithium. This essentially means that the ratio of electrode particles to the charge transfer has been reduced, which results in an increase in the change in the SOC of the positive electrode. Thus, the limiting voltage is reached earlier, resulting in capacity loss.

The two mechanisms stated here both contribute to the capacity loss. The capacity of the battery, Q (Ah) can be given by,

$$Q = \frac{\Delta SOC_n}{100}\frac{C_{max,n}FAL_n\varepsilon_n}{3600} \tag{5.1a}$$

$$Q = \frac{\Delta SOC_p}{100}\frac{C_{max,p}FAL_p\varepsilon_p}{3600} \tag{5.1b}$$

here, ΔSOC_i is the range through which the electrodes cycle, $C_{max,i}$ (mol/m^3) is the theoretical saturation concentration of each electrode material, F (C/mol) is Faradays' constant, A (m^2) is the current collector area, L_i (m) is the electrode thickness, and ε_i is the active material volume fraction. Eq. 5.1a and 5.1b show that the two variables representing the mechanisms under consideration, ΔSOC (LLI) and changes to the electrode active material fraction ε_i, (LAM) are not mutually exclusive and contribute to the capacity and thus the capacity fade. These equations indicate four unknown parameters to be studied. Namely, the ΔSOC operating range of the two electrodes and the active material fractions of the two electrodes. In this model, these four parameters were varied in order to get the best agreement between the experimental and model generated 1C discharge curves as the battery aged. This data was later used to derive the incremental capacity and differential voltage analysis curves in order to verify that the degradation mechanisms chosen were accurate. The 1C discharge prediction data after 40 and 100 kAh is shown in Figure 77. It can be noted that the model predictions have good agreement with the experimental data.

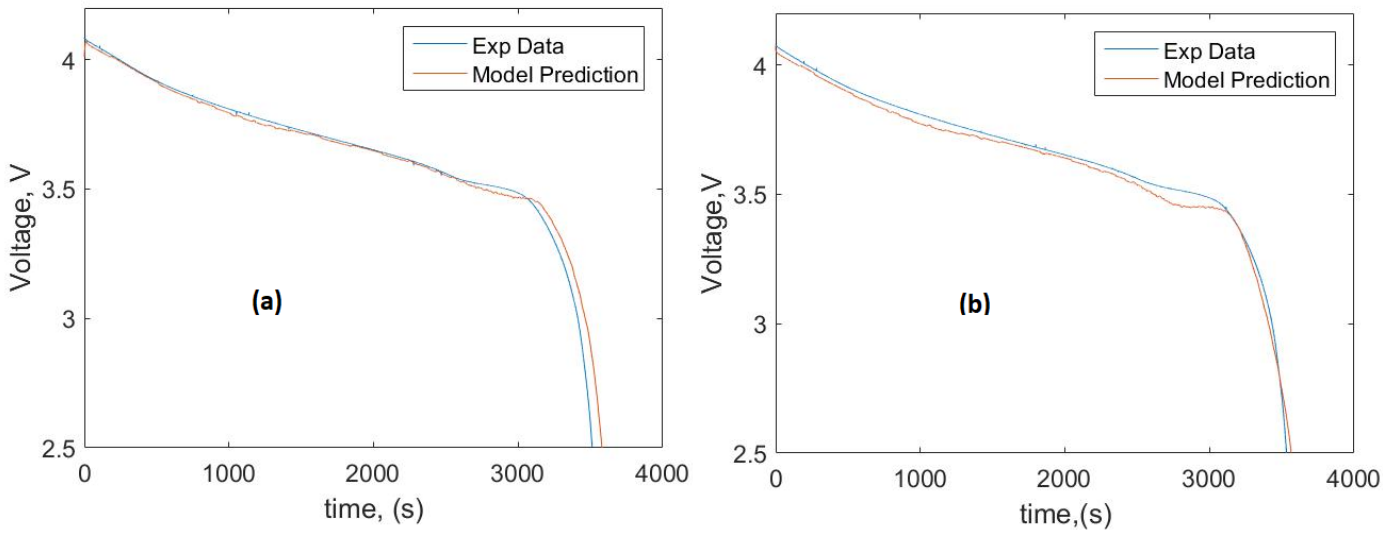

Figure 77: 1C prediction after (a) 40 kAh and (b) 100 kAh using the finite difference approach

Of the four parameters mentioned, the starting SOC of the positive electrode is essentially constrained when the cell is fully charged due to the voltage limits of the battery. The optimal value for the other three parameters (i.e., the active material fractions of the negative and positive electrodes and the starting SOC of the negative electrode when the cell is fully charged (ε_n, ε_p, and $\Delta SOC_{n,fc}$) were chosen after conducting a parameter optimization study. In this study, the optimal combination of these parameters that minimized the total error associated with the model predictions was determined at specific points in the life of the battery (i.e., 40 kAh and 100 kAh). The error in the model can be given as: $error = \sum \frac{|V_{exp} - V_{model}|}{V_{model}}$. The range of values for which the parametric study was done is given in Table 10.

Table 10: range of parameters for parametric study

Parameter	Range in parametric study
ε_n	0.5 – 1.0
ε_p	0.5 – 1.0
$\Delta SOC_{n,\text{fully charged}}$	30 % – 100 %

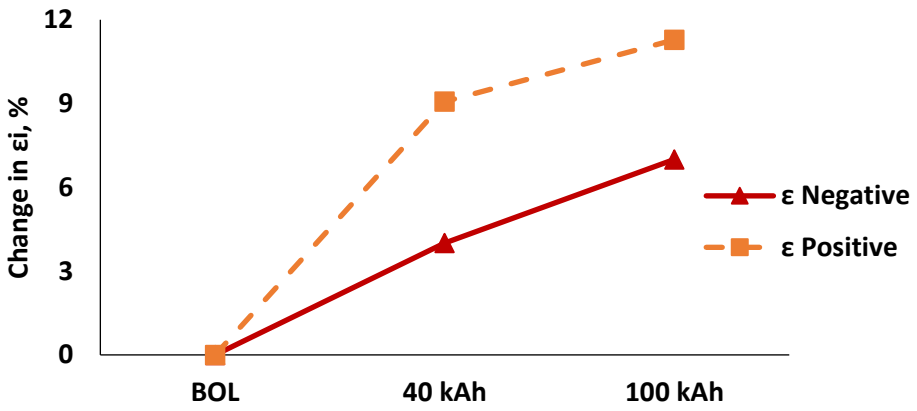

Figure 78: Active material fraction change relative to BOL

The loss of active material from both electrodes as a percentage of BOL values as identified by the parameter optimization study are shown in Figure 78. It can be noted that the model suggests that the positive electrode lost a higher percentage of its active material compared to the negative electrode.

Figure 79, shows the shift in the SOC ranges of the electrodes as they age. In the case of graphite, the SOC differential went from 74.9 percent at BOL to 70.16 percent at EOT and for the positive electrode, the SOC differential was 97.18 percent at BOL and that changed to 95.45 percent at EOT. The shifts in the operating rages of both the electrodes is indicative of the loss in lithium inventory due to side reactions.

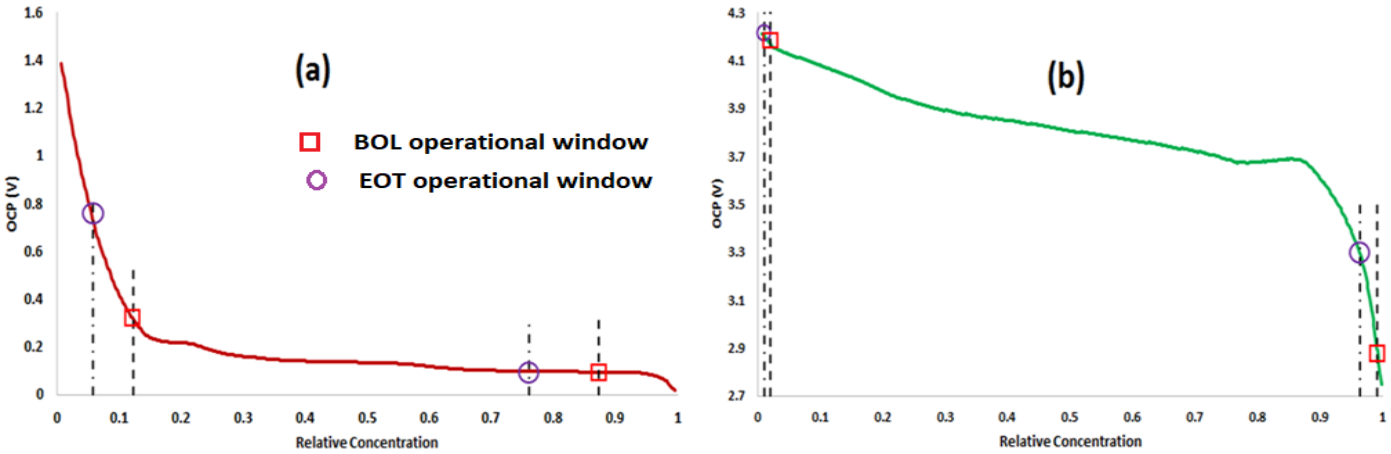

Figure 79: Operating range change made in model (a) negative electrode, and (b) positive electrode

From the 1C discharge data derived from the model, incremental capacity and differential voltage curves were obtained. By studying these analysis curves and the curves obtained experimentally, the validity of the choice of degradation mechanisms can be explored. Figure 80 and Figure 81 show the analysis curves obtained by experiments and model respectively.

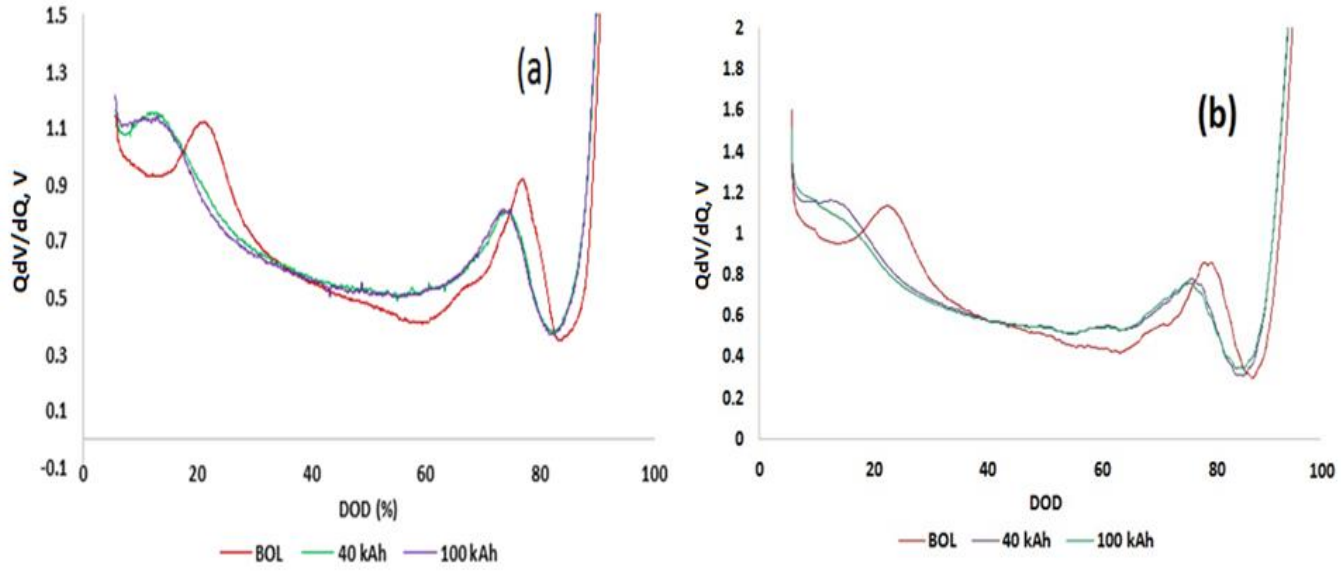

Figure 80: Differential voltage curves from (a) experiments (b) model

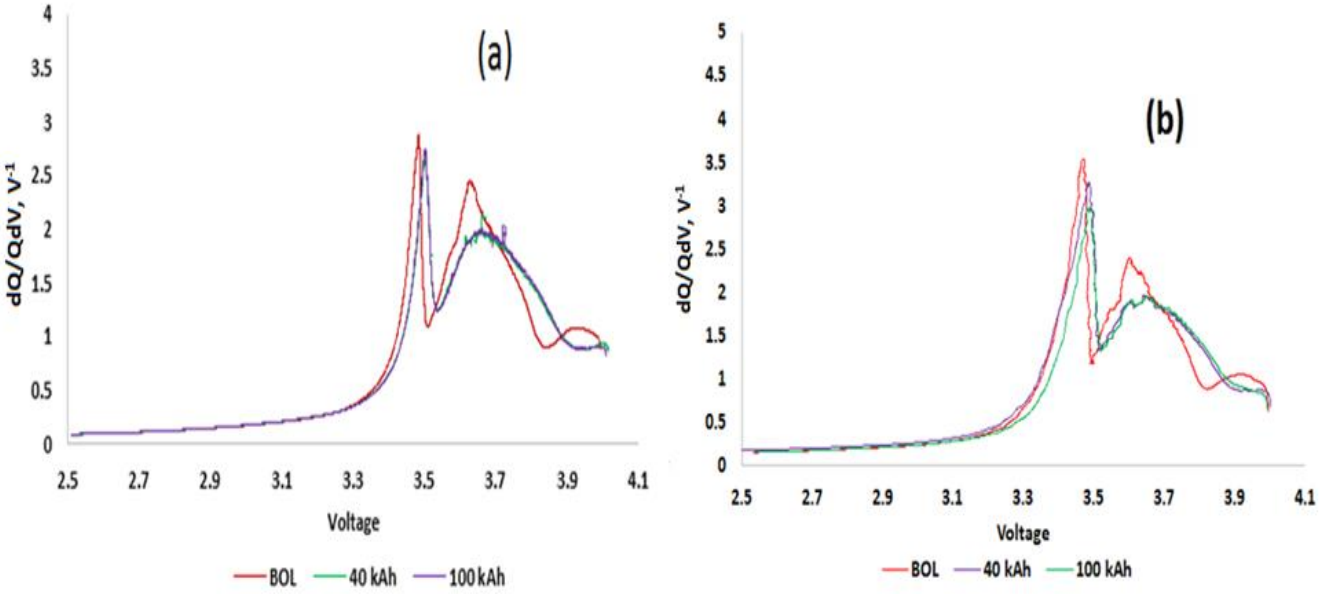

Figure 81: Incremental capacity curves from (a) experiments (b) model

Comparing Figure 80a and Figure 80b, it can be seen, that by incorporating the LAM and LLI degradation mechanisms in the model, the analysis curves generated from the model data exhibit changes similar to the experimental data. The peak near 80 percent DOD has shifted slightly to the left towards a lower DOD, and has reduced in magnitude, similar to the experimental curves. Similarly, the peak near 20 percent DOD has also shifted to lower DOD. Changes in peak magnitude and shifts in peak locations correspond to loss of active material and loss of lithium respectively [132], [134], and [138]. Comparing the incremental capacity curves (Figure 81a and Figure 81b), similar changes to the characteristic peaks can be observed. The peak between 3.3 V and 3.5 V has shifted slightly towards higher voltages with a small change in magnitude. At the same time, the second peak centered on 3.7 V has broadened, reduced in magnitude with a minor shift towards higher voltages. These changes are once again indicative of loss of lithium and loss of active material [70], [139] and [140]. Minor differences in the locations and shapes of the peaks between the experimental and model derived analysis curves can be noted and these are to be expected considering some parameters had to be either assumed or taken from literature data possibly leading to the observed differences. However, these differences are negligible and the evolution of the characteristic peaks between the model and experimental data as well as between the two profiles suggest the presence of the same degradation mechanisms. An argument can be made for the validity of the model parameters as well as the choice of degradation mechanisms considered in order to emulate the changes to the battery i.e. loss of cyclable lithium and loss of active material from the electrodes.

During the RPT tests, the changes to the resistance of the battery were studied using the PNGV model and a resistance term was incorporated into the model. However, the resistance term used proved to have a negligible effect on the analysis curves. Usually, in addition to LAM and LLI, the contribution to the degradation (power fade) by changes in resistance can also be observed as a shift in the characteristic peaks towards higher voltages (albeit to a lesser degree when compared to the shift due to active material loss). However, in the case of these high power batteries, changing the resistance did not produce any noticeable changes to the incremental capacity curves. This is illustrated in Figure 82, which compares the incremental capacity curves generated at 100 kAh for different resistance values ranging from BOL (1.8 mΩ) to EOT (2.18 mΩ).

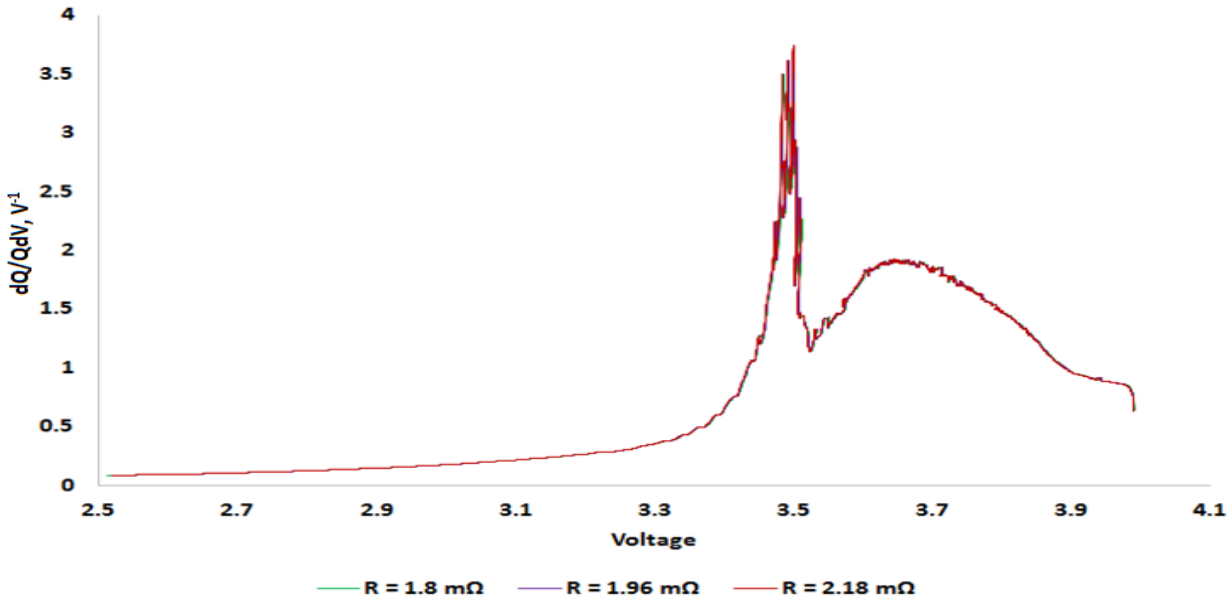

Figure 82: Incremental capacity curves for different resistance values

5.11 Coin Cell Degradation

For the coin cells, parameters such as electrode thickness, particle size, current collector and electrode area are either known or designed and were incorporated into the model. Positive electrodes for the coin cells and the commercial cells were nominally NMC, but slight variations can occur in terms of chemistry. Therefore, some of the properties (e.g. diffusion coefficient) related to the NMC electrode were changed accordingly. The change in these properties can be justified by noting that slight variations can occur between the electrodes based on the ratios of Ni, Mn, and Co. In addition to the electrode related properties, some transport parameters for the electrolyte and solvent also changed between the commercial and coin cells. Additives are a popular method to control the behavior of the cell and any that may have been used in the commercial cells are also currently unknown and could contribute to slightly varied transport properties in the liquid phase. The parameters that vary between the coin cell and the commercial cells are listed in Table 11. Parameters not listed in Table 11 were the same as for the commercial cells. The parameters used for the coin cells are well within the ranges established in Table 8.

Table 11: Values of parameters that differ between the commercial and coin cells

Parameter	Coin cell	Commercial
$k_{0,p}$	1.08e-11	1.80e-11
D_n (m^2/s)	4.10e-15	2.80e-15
D_l (m^2/s)	6.30e-10	4.52e-10
L_n (m)	40e-06	15e-06
L_p (m)	45e-06	7.5e-06
A_n (m^2)	1.60e-04	1.05
A_p (m^2)	9.70e-05	1.05

5.11.1 Model Prediction of Coin Cell Voltage Response

Figure 83 shows the BOL discharge voltage prediction by the model compared to the experimental data for the cells that were cycled using the two extreme profiles namely, zero percent above 3.8 V and twenty percent greater than 3.8 V. It can be seen that the coin cell model with the updated parameter values predicts the voltage response well.

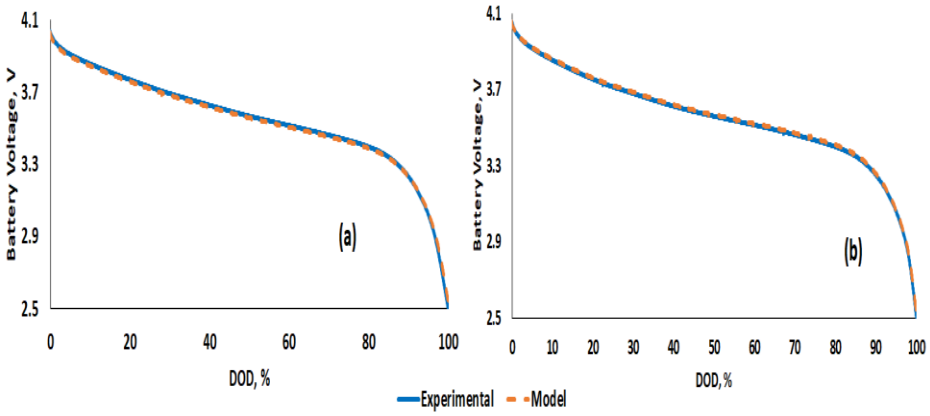

Figure 83: Discharge voltage prediction for coin cells, (a) 0 % time spent above 3.8 V, (b) 20 % time spent above 3.8 V

In addition to the discharge predictions, the model was also used to predict the transient response of the coin cells during cycling. The two model predictions for the two extreme profiles are shown in Figure 84. It can be seen that the model predicts the transient behavior accurately.

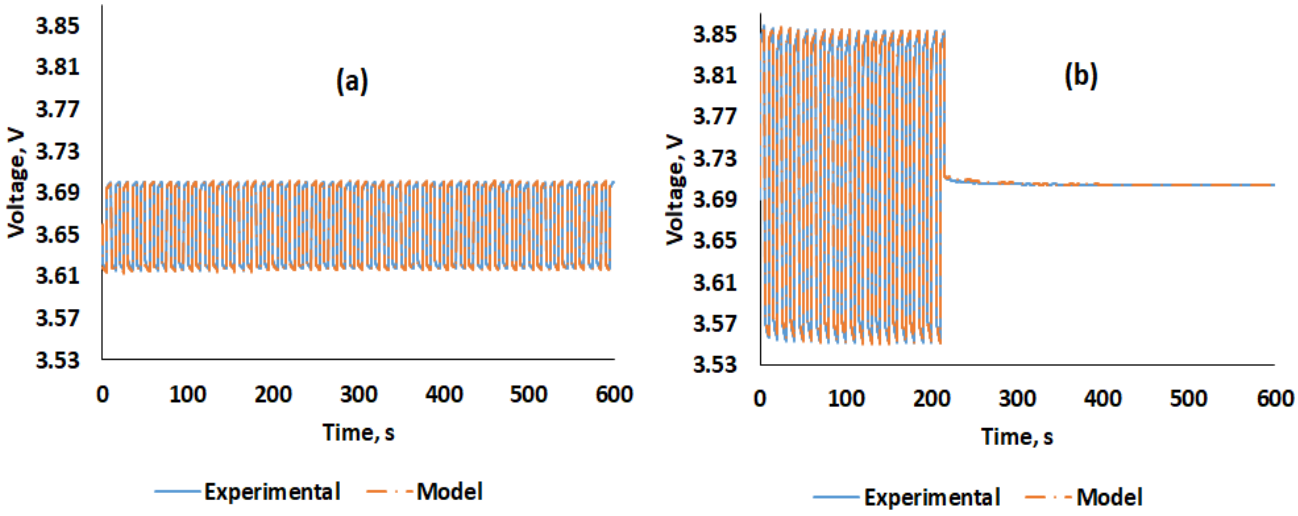

Figure 84: Model prediction of coin-cell cycling behavior, (a) 0% time spent above 3.8 V, (b) 20 % time spent above 3.8 V

5.11.2 Ageing in Cycled Coin Cells

Similar to the commercial cells, as the cells cycled, the active material fractions and the SOC differential for individual electrodes were changed in order to match the experimental and model data. It is to be noted that the manufacturer specifies an active material mass fraction for the powders used in the electrode. However, the useable/actual active material volume fraction in the fabricated electrodes can change depending on fabrication procedure and the quality control. These two steps can determine how successful a particle is at having an electrical pathway to the current collector. The voltage predictions from the model after 500 and 1000 cycles for the two extreme profiles are shown in Figure 85 and Figure 86. The model-generated data agrees well with the experimental data validating the changes made to the parameters to simulate the two degradation mechanisms.

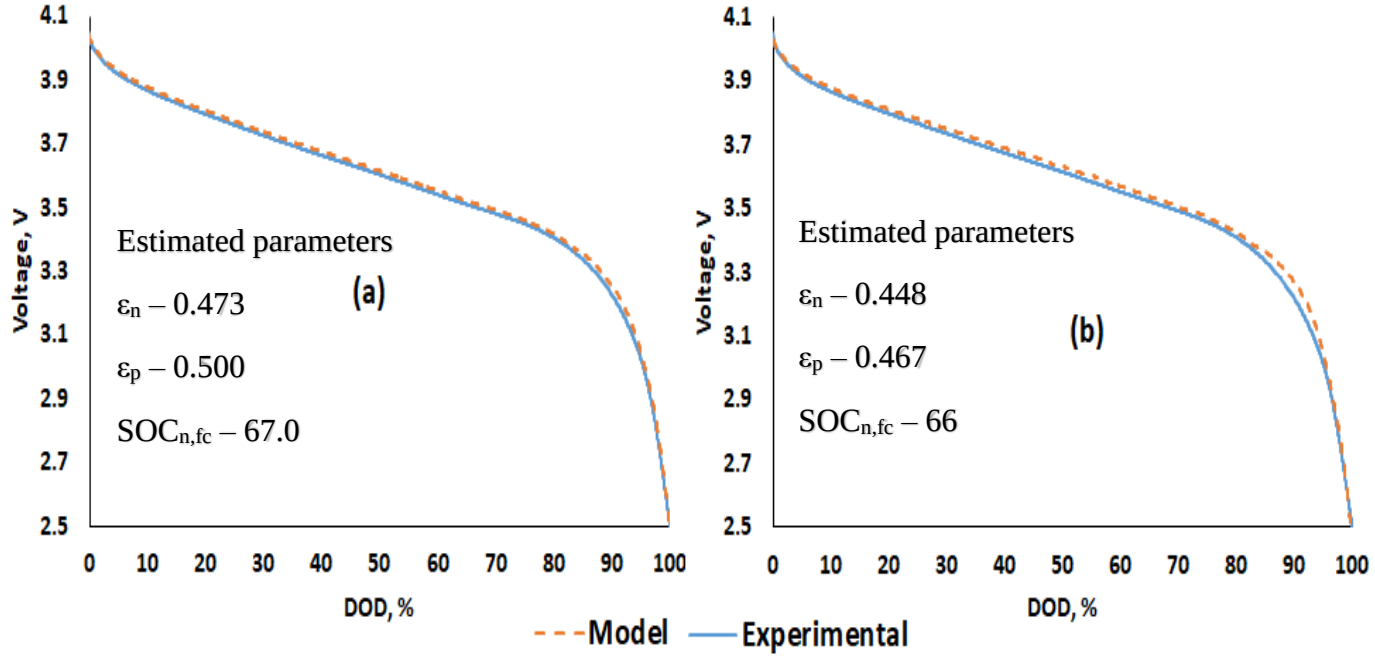

Figure 85: Model voltage prediction vs experimental data for batteries cycled with the 0 % above 3.8 V profile, (a) after 500 cycles, and (b) after 1000 cycles

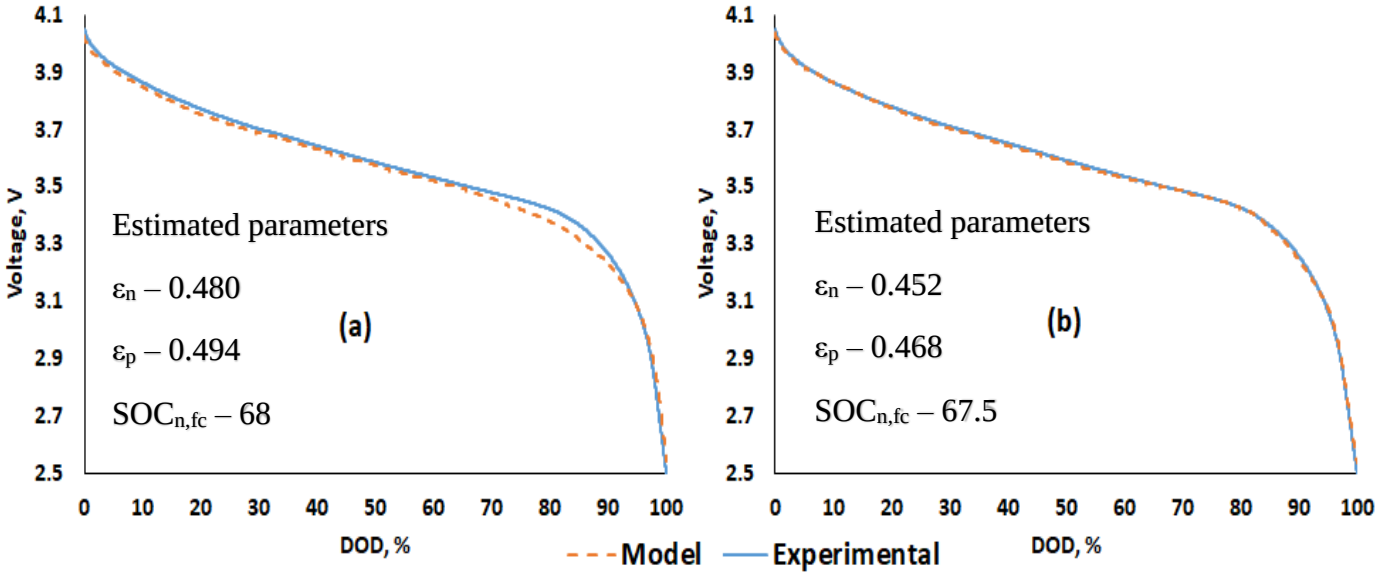

Figure 86: Model voltage prediction vs experimental data for batteries cycled with the 20 % above 3.8 V profile, (a) after 500 cycles, and (b) after 1000 cycles

The change in the active material volume fraction as a percentage of BOL in the model is given in Figure 87. It can be observed that in both profiles, the model predicted similar changes to the active material fractions. The active volume fraction of NMC reduced by ~28 percent at EOT while the

change for graphite was around 26 percent. These values are similar to the capacity fade (active material fraction) noted for each electrode from the half-cell data. The changes to this parameter in the model also indicate similar degradation mechanisms in the two profiles.

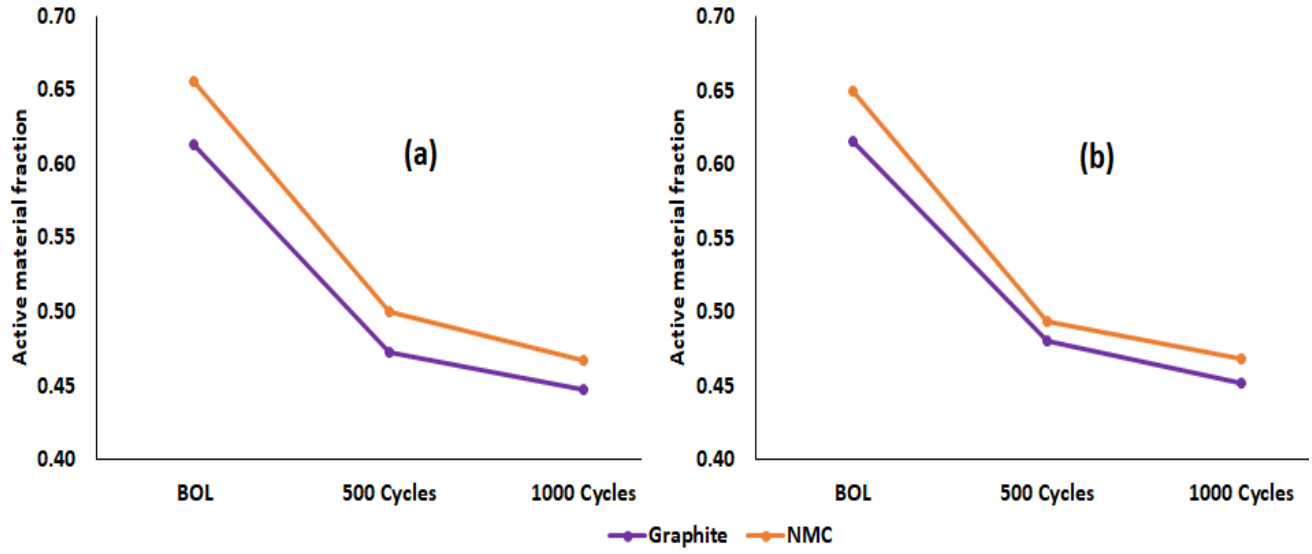

Figure 87: Change in active material fraction for batteries cycled using (a) 0 % time spent above 3.8 V, and (b) 20 % time spent above 3.8 V

The shift in the operating SOC range for both profiles, which is a measure of the loss in lithium due to side reactions, is shown in Figure 88 and Figure 89. The changes observed in the ΔSOC range of the individual electrodes for both type of profiles is similar. This indicates that similar quantities of lithium inventory are consumed in side reactions regardless of the profile used. In addition, the relatively small change in the ΔSOC range also indicates that the loss of lithium due to side reactions is minimal. The changes to the ΔSOC ranges due to ageing, when converted to the actual amount of lithium ions lost due to side reactions, indicate a loss of around 1.5 percent.

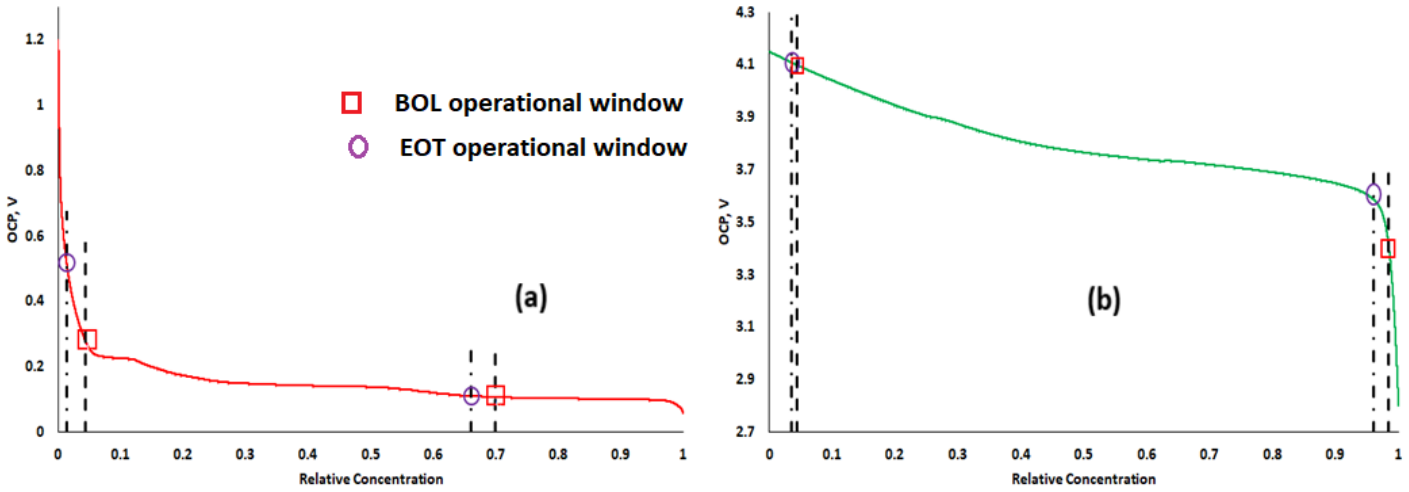

Figure 88: Shift in operational SOC window for (a) graphite, and (b) NMC for cells cycled with the profile that spends 0 % time above 3.8 V

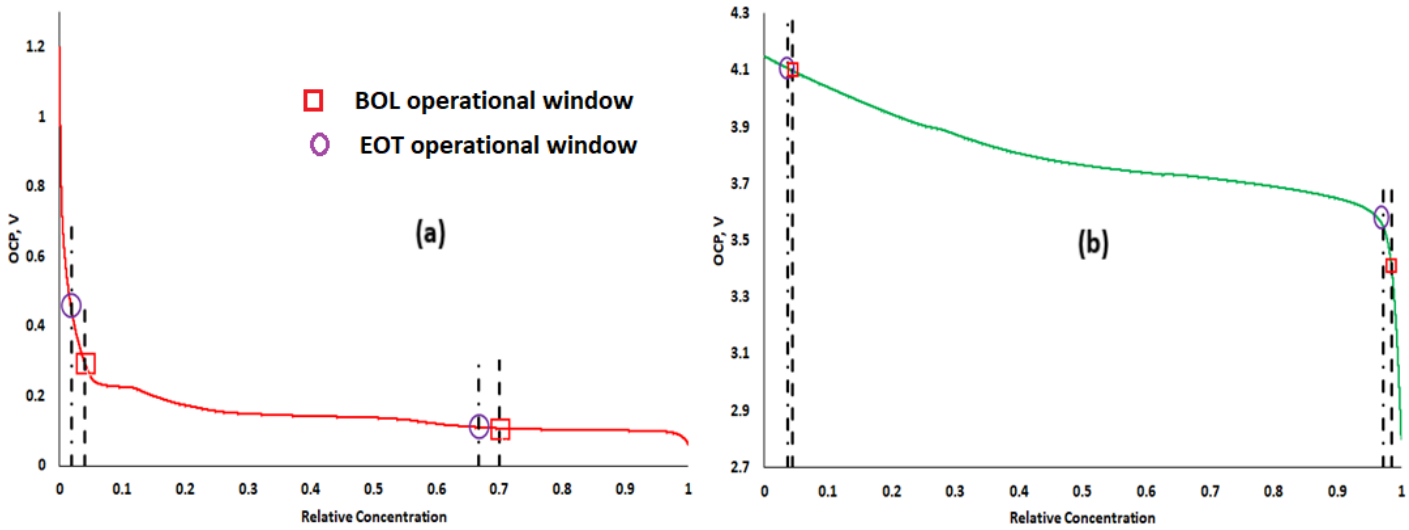

Figure 89: Shift in operational SOC window for (a) graphite, and (b) NMC for cells cycled with the profile that spends 20 % time above 3.8 V

The experimental observation that the degradation is unaffected by the cycle profile are supported by the model predictions as well. The model predicts similar changes to the active material fractions and operational SOC range for both profiles indicating similar degradation mechanisms. Additionally, the percentage change in the active material fractions are similar to the experimental results.

The differential voltage and incremental capacity curves were generated with the model predicted voltage data in order to confirm the validity of the degradation mechanisms chosen. These plots shown in Figure 90, also display similar changes (as the batteries continue to age) as seen in the

experimental data. The broadening of peaks and the small shifts in peak locations observed in the experimental curves can be noted in Figure 90 b and Figure 90 d as well

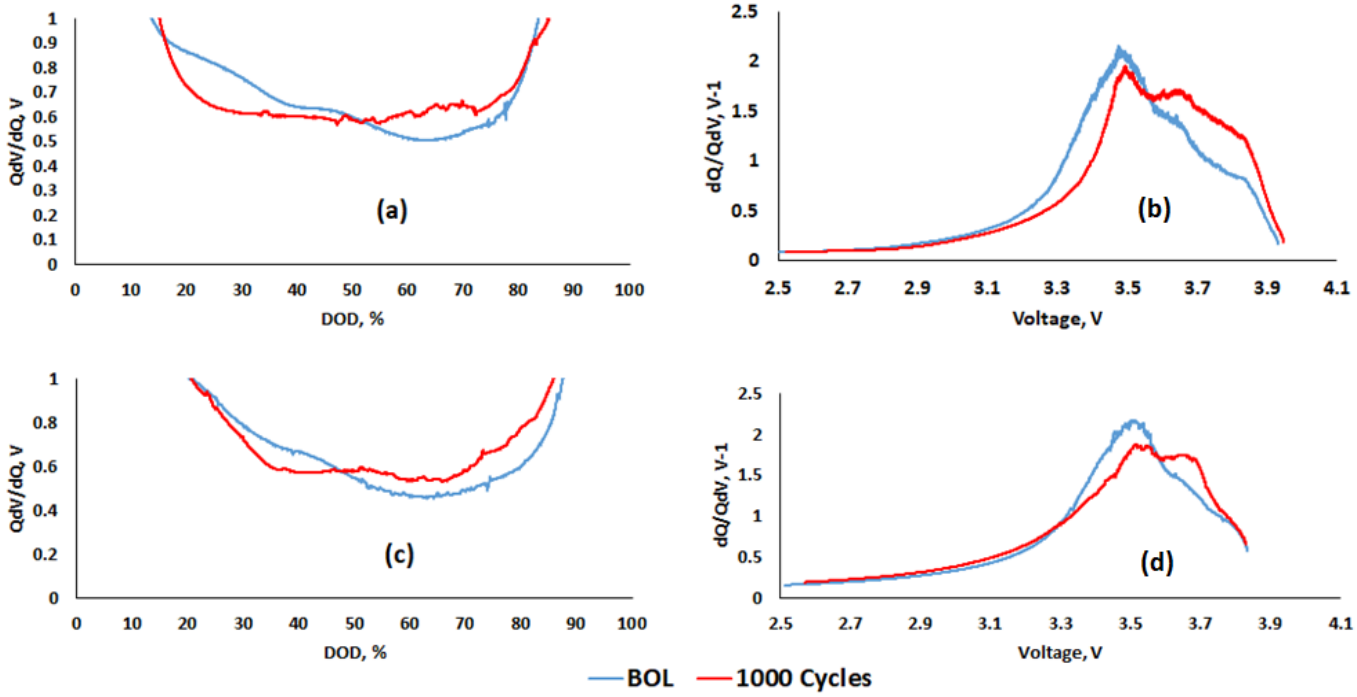

Figure 90: model derived analysis curves for coin cells; (a) differential voltage and (b) incremental capacity for cells cycled with 0 % time above 3.8 V, (c) differential voltage and (d) incremental capacity for cells cycled with 20 % time above 3.8 V

Summary of coin cell testing

The coin cells cycled with four different profiles exhibit a capacity loss of ~ 29 percent after 1000 cycles and the profile used did not have a significant impact on the amount of capacity fade. The resistance change in the cells indicate that the exposure to voltages greater than 3.8 V results in minor increases in resistance compared to the batteries cycled below 3.8 V. The cells held at high voltages without cycling exhibit capacity loss of ~ 20 percent over a much longer time-period. However, comparing the capacity loss normalized to the time spent above 3.8 V, the effect of exposure to higher voltages on the capacity fade was minimal and it was shown that the cycling was primarily responsible for the noted capacity fade. Additionally, the results from FIB milling and imaging of the SEI layers also indicate similar degradation mechanism between the two extreme profiles i.e. cycle profile did not have an impact on the capacity loss.

Results from half-cell studies show a similar amount of capacity loss in the electrodes of the cycled cells as for the full cell. Whereas, in the case of the cells held at high voltage, smaller values of

capacity loss were noted in the individual electrodes compared to the full cell indicate that the capacity was lost due to the loss of cyclable lithium to side reactions. These results indicate that the cause of degradation for the cells held at higher voltages is the loss of lithium due to side reactions and in the case of the cycled cells, the primary contributing mechanism is the degradation to the electrodes or loss of active material associated with charge throughput. However, there can be minor contribution to the capacity fade from the loss of cyclable lithium.

The differential voltage and incremental capacity analysis curves exhibit changes to the magnitude of the observed peaks as well as minor shifts in peak locations. These changes compared to work in the literature suggest the presence of both loss of active material and loss of lithium. The analysis curves support the choice of the degradation mechanisms considered in this work however, these methods do not directly indicate which of the mechanisms is more prominent which we obtain from the half-cell testing. Additionally, similar changes to the analysis curves between different profiles indicates similar degradation mechanisms, which was also noted in the capacity loss analysis.

Comparing the voltage predictions as well as the analysis curves between the model and experimental data shows that the changes made to the parameters to simulate degradation are valid. Changes noted to the analysis curves experimentally were also noted in the model-generated data further supporting the result that the capacity fade is predominantly dependent on the charge throughput. Additionally, the changes made to the active material fraction (~28 percent) in the model to study the degradation mirrors the observations noted experimentally about the capacity loss noted in individual electrodes from half-cell tests. The small changes in the model predictions for the operational SOC ranges of the coin cells as they age also support the claim that LLI only plays a minor role in the observed capacity fade in the coin cells. In addition to the analysis curves, the similarities in the changes to the active material fraction as well as the changes in the lithium inventory between the two profiles add support to the argument that the capacity fade is primarily driven by charge throughput.

Extending Coin Cell Results to Understand Commercial Cell Degradation

The insights gained from testing coin cells can be applied to explain the degradation observed in the commercial cells. The coin cells, similar to the commercial cells, did not exhibit a dependence of capacity fade on the profile used and the charge transfer was responsible for the capacity fade.

Profiles that expose batteries to higher voltages result in slightly higher increases in resistance for both type of cells. Results from half-cells made from the coin cells indicate that loss of active material is the primary cause of degradation in the coin cells and effects from loss of lithium due to reactions at higher voltages is minimal. This result cannot be directly extended to the commercial cells. However, both types of cells exhibit similar changes to the analysis curves leading to the conclusion that both loss of active material and loss of lithium contribute to the observed fade in the commercial cells. For both the coin cells and the commercial cells, the model results suggest loss of active material as the primary mechanism regardless of the cycling profile. This result was confirmed by half-cell studies for the coin cells. However, the actual contributions of the two mechanisms to the observed fade cannot be confirmed for the commercial cells without testing coin cells made from cycled commercial cell electrodes.

Chapter 6 - Summary and Future Work

Summary of Results

The primary objective of this study was to understand how cycle profile affects the degradation in commercial NMC batteries. In order to evaluate the relation between the profiles and degradation, commercial batteries with nominal beginning of life capacities of 5 Ah were cycled with two very different profiles the first, a pulse profile derived from a PHEV subjected to the US06 drive cycle, which simulates real world, on-road conditions; The second, a simple square-wave profile with the same charge throughput and RMS current as the pulse profile. During testing, the batteries cycled with the pulse profile experienced higher voltages, a larger voltage window and larger SOC differential compared to the batteries cycled with the square profile. After 100 kAh of cycling, the capacity tests revealed that the cycle profile did not have an impact on the rate of capacity loss and the batteries cycled with both profiles exhibited capacity losses around 12 percent compared to beginning of life. The capacity fade of the batteries was found to correlate with throughput but to be independent of cycle profile.

Standardized power (HPPC) tests for the batteries did not reveal a significant change in the power capability of the batteries regardless of the profile used. However, using the data obtained from the HPPC tests, a regression-based model identified that the batteries cycled with the pulse profile showed higher increases in cell resistance compared to the batteries cycled with the square profile. The discrepancy between the increased cell resistance and the lack of significant change to the power capability of the batteries is explained by noting the small starting value of the resistance, which resulted in a relatively small values for the ohmic losses (and hence stack power losses) as the batteries aged.

In order to verify that the results obtained for the two profiles with cycling tests at 40 percent SOC (and the associated SOC differential) could be generalized; two sets of the batteries were removed from cycling after 40 kAh of charge throughput and tested (i) at higher SOC and (ii) at higher SOC differential. Testing at these conditions led to degradation similar to the base case and demonstrated that the profile did not affect degradation in either case.

These results indicate that for high power cells, the capacity degradation associated with the charge-sustaining mode of operation can be studied with relatively simple approximations of complex drive cycles. This conclusion can reduce test facility costs because the equipment needed

to test simple profiles tends to be cheaper to purchase and operate compared to the equipment needed to simulate complex profiles similar to on-road conditions.

The data generated from the capacity tests were further used for developing incremental capacity and differential voltage plots. These plots can suggest likely degradation mechanisms based on the changes observed in characteristic peaks. The changes to these curves are similar between the two profiles used, suggesting similar degradation mechanisms. The similar progression of these curves with charge throughput and the limited differences with cycle profile suggest that the charge transfer is key for the observed capacity fade and not the type of profile used. The changes to these curves also suggest the presence of active material loss and loss of lithium due to side reactions. However, these characteristic plots can only indicate the presence of degradation mechanisms but not the extent of contribution from each mechanism.

Since circumstances prevented the dismantling of the commercial cells, coin cells with similar electrode chemistries were assembled with commercially available materials in order to study the underlying degradation mechanisms. The results from cycling studies indicated that the coin cells could not match the commercial cells in terms of discharge rates. Therefore, new test protocols were developed to address the limited rate capability of these coin cells. Four cycles with the same charge throughput, each exposing the coin cells to voltages above 3.8 V for different durations were developed. These cycles, each 10 minutes long, exercised the coin cells to voltages greater than 3.8V for 0, 10, 15, and 20 percent of the cycle duration. Additionally, some of the coin cells were left at high voltages without cycling for 30 days in order to distinguish between the effects of cycling and high voltage. The cells maintained at high voltage without cycling exhibited capacity loss of 20 percent after 30 days or 0.67 percent per day. After 1000 cycles, results for the cycled coin cells indicate that regardless of the profile used, the coin cells exhibited similar capacity loss. The losses observed for the cycled coin cells were around 30 percent of the beginning of life capacity. The overall time spent at high voltages for the extreme case of cycling (i.e., 20 percent of cycle duration spent above 3.8 V) was 1.4 days. At 0.67 percent per day (from the uncycled cell study), this yields roughly 1 percent capacity loss attributable to exposure to high voltages for this profile with the remaining 29 percent attributable to cycling. This result demonstrates that the majority of degradation originates from the cycling process and that the high voltage peaks used in the cycling studies have a minimal impact on the capacity loss.

The results from the capacity and EIS tests conducted on the coin cells lead to conclusions similar to the ones reached from the commercial cell testing.

- The capacity loss is not significantly affected by the profile for similar levels of throughput.
- The majority of the capacity loss is due to the charge transfer process and not due to high voltages or calendar effects.
- The change in cell resistance is higher for batteries exposed to higher voltages.

Similar to the commercial cells, analysis curves were also generated from the discharge data of the coin cells. The changes in these characteristic peaks indicate similar degradation mechanisms between the coin cell profiles, adding support to the observation that charge transfer and not profile, is primarily responsible for the observed capacity fade. Additionally, the changes to the characteristic peaks also suggest the presence of both active material loss and loss of cyclable lithium.

Post-cycling tests of individual coin cell electrodes were also conducted to study the degradation mechanisms. Half-cells made from cycled and calendar aged electrodes were prepared using pure lithium metal as the counter electrode. These cells were tested to identify the contribution of individual electrodes to the capacity fade. These half-cells exhibited capacity losses of around 28 percent, similar to the average overall capacity lost by the full cells. However, in the case of the cells held at high voltage, the cathode half-cells and the anode half-cells exhibited only 5 and 10 percent capacity loss respectively, which is much smaller than the 20 percent overall loss observed in the full cells.

The advantage of using a lithium metal counter electrode in testing half-cells is that loss of lithium due to side reactions is not a concern and can be neglected. Pure lithium metal can be considered a pseudo-infinite source of lithium ions in half-cells specifically since the actual capacity (in mAh) of the electrodes is small compared to the capacity of a similarly sized pure lithium electrode. This observation enables us to consider the origin of any noted capacity loss to be from changes happening to the electrodes themselves. In the case of the cycled cells, the 28 percent loss noted in the individual electrodes has to originate from damage to the electrodes themselves and can be considered active material loss. However, in the case of the cells held at high voltage, the individual electrodes lost less capacity than the overall cell indicating that the active sites needed

for the lithium insertion still exist in the full cell, but there is a lack of cyclable lithium ions for these reactions to occur leading to the observed capacity fade. This means that those lithium ions were consumed elsewhere due to side reactions. The results from the half-cells indicate that the predominant degradation mechanism for the coin cells cycled with the four profiles is loss of active material.

In addition to the experiments, a physics based model derived from porous electrode theory and the single particle model was implemented in order to study the degradation mechanisms. This model considers the behavior of a single spherical particle in each electrode to be representative for the entire electrode. This model predicts the voltage of the battery by considering the open circuit potentials of the electrodes (based on the SOC), the kinetic overpotentials (based on surface concentrations), the voltage drop across the electrolyte phase (due to concentration gradients), and a voltage drop due to the cell resistance that varies with ageing. The finite difference method was used to solve for the concentration gradient in the liquid phase and to evaluate the lithium concentration inside the electrode particles.

This method was successfully used to predict the cell voltage during low C-rate discharge tests as well as cycling. Once the battery behavior at BOL was successfully predicted, the model was used to study the degradation mechanisms. The loss of active material was input into the model as direct parameters while the loss of lithium was reflected by a shift in the working range of the individual electrodes due to lithium loss. The results from the model indicate that active material losses in the electrodes were the dominant degradation mechanism with a smaller contribution due to lithium loss. The differential voltage and incremental capacity curves generated by the model are similar to the ones obtained from the experiments and the changes to the characteristic peaks due to inclusion of the degradation mechanisms in the model are similar to the changes observed in the experiments. In addition to supporting the conclusions regarding degradation mechanisms, the modeling results demonstrate that a relatively simple physics based model can provide reasonable insights into the behavior of a battery and the degradation mechanisms without resorting to expensive, and time consuming post-mortem analysis techniques.

The model was also used to study the degradation mechanism in the coin cells. Once the parameters such as electrode thickness, current collector area etc. were changed in order to reflect the properties of the coin cell materials, the model was used to predict the discharge and cycling

behavior of the coin cells. After the successful implementation of the model for predicting the coin cell voltage response, changes were made in the model to simulate active material loss and lithium loss. The model predicted active material loss of around 27 percent for both electrodes, which is similar to the experimental results from the half-cells. Thus, considering the experimental results from the coin cells, the half-cells and the model for the coin cells, it can be stated that the primary degradation mechanism for the cycled coin cells is active material loss.

Results from the cell behavior lends support to the conclusions for the commercial cells, i.e. details of the cycle profile and calendar aging had limited impact on capacity loss; and the primary cause of fade is the active material loss resulting from charge transfer. This conclusion does not exclude loss in capacity due to lithium consuming side reactions but rather states that the dominant mechanism for these power cells is the loss of active material due to the charge transfer process while the capacity loss due to lithium consuming reactions plays a secondary role.

Future Work

The work done in this study could be extended to other chemistries and battery designs in order to ascertain the range of applicability of these results. In order to meet the cost and performance targets set by USABC and other agencies, new electrode chemistries and materials are being developed at a rapid pace. By testing these new battery systems and comparing those results against this work, a database can be created that can help manufacturers identify the best material or chemistry use for a particular application. Also, electrode materials from the commercials cells could be made available for further post-mortem testing in order to confirm assumptions made in the model. This also allows for direct capacity loss and thus identification of degradation mechanisms in the commercial cell instead of having to rely on results from similar materials. The model could be expanded to include the effect of temperature and the effect of the concentration gradient across the electrodes. The model can also be used to isolate the contributions to degradation from any particular process. The effects of changes to one particular parameter representing a physical change can be studied the model can be further developed to account for diffusion and ion transport in three dimensions. The potentials advantages of such detailed higher order models can be weighed against the inherent complexities involved in their development. Additionally the use of other spectroscopy techniques could be explored in order to study the surface of the cycled electrodes as well as assess the damage to the electrode due to cycling. for example, BET can be used to identify changes to the surface area of the electrodes due the

intercalation process or techniques such as wavelength dispersive spectroscopy (WDS) can be used to study identify different elements on the surface (which can lead to clues about degradation mechanisms) when more common methods such as EDS cannot yield useful information.

References

[1] M.-K. Song, S. Park, F.M. Alamgir, J. Cho, M. Liu, Nanostructured electrodes for lithium-ion and lithium-air batteries: the latest developments, challenges, and perspectives, Mater. Sci. Eng. R Reports. 72 (2011) 203–252. doi:10.1016/j.mser.2011.06.001.

[2] T.M. Bandhauer, S. Garimella, T.F. Fuller, A Critical Review of Thermal Issues in Lithium-Ion Batteries, J. Electrochem. Soc. 158 (2011) R1. doi:10.1149/1.3515880.

[3] A. Manthiram, T. Muraliganth, Lithium Intercalation Cathode Materials for Lithium-Ion Batteries, in: Handb. Batter. Mater., Wiley-VCH Verlag GmbH & Co. KGaA, 2011: pp. 341–375. doi:10.1002/9783527637188.ch12.

[4] A. Bartlett, J. Marcicki, S. Onori, G. Rizzoni, Y. Xiao Guang, T. Miller, Model-based state of charge estimation and observability analysis of a composite electrode lithium-ion battery, Decis. Control (CDC), 2013 IEEE 52nd Annu. Conf. (2013) 7791–7796. doi:10.1109/CDC.2013.6761126.

[5] C. Liu, Z.G. Neale, G. Cao, Understanding electrochemical potentials of cathode materials in rechargeable batteries, Mater. Today. 19 (2016) 109–123. doi:10.1016/j.mattod.2015.10.009.

[6] L.O. Valøen, J.N. Reimers, Transport Properties of LiPF[sub 6]-Based Li-Ion Battery Electrolytes, J. Electrochem. Soc. 152 (2005) A882. doi:10.1149/1.1872737.

[7] USCAR DRIVE Report, 2015.

[8] J. Vetter, P. Novák, M.R. Wagner, C. Veit, K.-C. Möller, J.O. Besenhard, M. Winter, M. Wohlfahrt-Mehrens, C. Vogler, a. Hammouche, Ageing mechanisms in lithium-ion batteries, J. Power Sources. 147 (2005) 269–281. doi:10.1016/j.jpowsour.2005.01.006.

[9] S.H. Kang, J.B. Goodenough, L.K. Rabenberg, Effect of ball-milling on 3 V capacity of lithium manganese oxospinel cathodes, Chem. Mater. 13 (2001) 1758–1764. http://dx.doi.org/10.1021/cm000920g.

[10] R. Srinivasan, a. Carson Baisden, B.G. Carkhuff, M.H. Butler, The five modes of heat generation in a Li-ion cell under discharge, J. Power Sources. 262 (2014) 93–103. doi:10.1016/j.jpowsour.2014.03.062.

[11] M.C. Smart, B. V. Ratnakumar, L.D. Whitcanack, K.B. Chin, S. Surampudi, H. Croft, D. Tice, R. Staniewicz, Improved low-temperature performance of lithium-ion cells with quaternary carbonate-based electrolytes, J. Power Sources. 119–121 (2003) 349–358. doi:10.1016/S0378-7753(03)00154-X.

[12] D. Kim, S. Park, O.B. Chae, J.H. Ryu, Y.-U. Kim, R.-Z. Yin, S.M. Oh, Re-Deposition of Manganese Species on Spinel LiMn2O4 Electrode after Mn Dissolution, J. Electrochem. Soc. 159 (2012) A193. doi:10.1149/2.003203jes.

[13] T. Waldmann, M. Wilka, M. Kasper, M. Fleischhammer, M. Wohlfahrt-Mehrens, Temperature dependent ageing mechanisms in Lithium-ion batteries - A Post-Mortem study, J. Power Sources. 262 (2014) 129–135. doi:10.1016/j.jpowsour.2014.03.112.

[14] H. Yang, S. Amiruddin, H.J. Bang, Y.K. Sun, J. Prakash, A review of Li-Ion cell chemistries and their potential use in hybrid electric vehicles, J. Ind. Eng. Chem. 12 (2006) 12–38.

[15] K.N. Radhakrishnan, D.J. Nelson, M.W. Ellis, Effect of Cycling Profile on the Durability of Commercial Lithium Ion Batteries, (2016).

[16] P. Verma, P. Maire, P. Novák, A review of the features and analyses of the solid electrolyte interphase in Li-ion batteries, Electrochim. Acta. 55 (2010) 6332–6341. doi:10.1016/j.electacta.2010.05.072.

[17] T. Xia, W. Zhang, Z. Wang, Y. Zhang, X. Song, J. Murowchick, V. Battaglia, G. Liu, X. Chen, Amorphous carbon-coated TiO2 nanocrystals for improved lithium-ion battery and photocatalytic performance, Nano Energy. 6 (2014) 109–118. doi:10.1016/j.nanoen.2014.03.012.

[18] J. Qiu, C. Lai, S. Li, S. Zhang, High-performance amorphous carbon–graphene nanocomposite anode for lithium-ion batteries, RSC Adv. 4 (2014) 18899. doi:10.1039/c3ra46566g.

[19] S. Flandrois, B. Simon, Carbon materials for lithium-ion rechargeable batteries, Carbon N. Y. 37 (1999) 165–180. doi:10.1016/S0008-6223(98)00290-5.

[20] P. Novák, D. Goers, M.E. Spahr, Materials in Carbon Lithium-Ion Batteries, Carbons Electrochem. Energy Storage Convers. Syst. (2010).

[21] D. Aurbach, Review of selected electrode–solution interactions which determine the performance of Li and Li ion batteries, J. Power Sources. 89 (2000) 206–218. doi:10.1016/S0378-7753(00)00431-6.

[22] D. Aurbach, The Study of Electrolyte Solutions Based on Ethylene and Diethyl Carbonates for Rechargeable Li Batteries, J. Electrochem. Soc. 142 (1995) 2882. doi:10.1149/1.2048659.

[23] E. Peled, D. Bar Tow, a. Merson, a. Gladkich, L. Burstein, D. Golodnitsky, Composition, depth profiles and lateral distribution of materials in the SEI built on HOPG-TOF SIMS and XPS studies, J. Power Sources. 97–98 (2001) 52–57. doi:10.1016/S0378-7753(01)00505-5.

[24] E. Peled, An Advanced Tool for the Selection of Electrolyte Components for Rechargeable Lithium Batteries, J. Electrochem. Soc. 145 (1998) 3482. doi:10.1149/1.1838831.

[25] T. Zheng, Reactivity of the Solid Electrolyte Interface on Carbon Electrodes at Elevated Temperatures, J. Electrochem. Soc. 146 (1999) 4014. doi:10.1149/1.1392585.

[26] S.S. Zhang, A review on electrolyte additives for lithium-ion batteries, J. Power Sources. 162 (2006) 1379–1394. doi:10.1016/j.jpowsour.2006.07.074.

[27] P. Ramadass, B. Haran, P.M. Gomadam, R. White, B.N. Popov, Development of First Principles Capacity Fade Model for Li-Ion Cells, J. Electrochem. Soc. 151 (2004) A196. doi:10.1149/1.1634273.

[28] M. Broussely, S. Herreyre, P. Biensan, P. Kasztejna, K. Nechev, R.. Staniewicz, Aging mechanism in Li ion cells and calendar life predictions, J. Power Sources. 97–98 (2001) 13–21. doi:10.1016/S0378-7753(01)00722-4.

[29] D. Aurbach, B. Markovsky, G. Salitra, E. Markevich, Y. Talyossef, M. Koltypin, L. Nazar, B. Ellis, D. Kovacheva, Review on electrode-electrolyte solution interactions, related to cathode materials for Li-ion batteries, J. Power Sources. 165 (2007) 491–499. doi:10.1016/j.jpowsour.2006.10.025.

[30] K. Edström, M. Herstedt, D.P. Abraham, A new look at the solid electrolyte interphase on graphite anodes in Li-ion batteries, J. Power Sources. 153 (2006) 380–384. doi:10.1016/j.jpowsour.2005.05.062.

[31] K. Edström, T. Gustafsson, J.O. Thomas, The cathode-electrolyte interface in the Li-ion battery, Electrochim. Acta. 50 (2004) 397–403. doi:10.1016/j.electacta.2004.03.049.

[32] S.J. An, J. Li, C. Daniel, D. Mohanty, S. Nagpure, D.L. Wood, The state of understanding of the lithium-ion-battery graphite solid electrolyte interphase (SEI) and its relationship to formation cycling, Carbon N. Y. 105 (2016) 52–76. doi:10.1016/j.carbon.2016.04.008.

[33] S. Malmgren, K. Ciosek, M. Hahlin, T. Gustafsson, M. Gorgoi, H. Rensmo, K. Edström, Comparing anode and cathode electrode/electrolyte interface composition and morphology using soft and hard X-ray photoelectron spectroscopy, Electrochim. Acta. 97 (2013) 23–32. doi:10.1016/j.electacta.2013.03.010.

[34] M. Nie, D.P. Abraham, D.M. Seo, Y. Chen, A. Bose, B.L. Lucht, Role of Solution Structure in Solid Electrolyte Interphase Formation on Graphite with LiPF 6 in Propylene Carbonate, J. Phys. Chem. C. 117 (2013) 25381–25389. doi:10.1021/jp409765w.

[35] D. Aurbach, Y. Talyosef, B. Markovsky, E. Markevich, E. Zinigrad, L. Asraf, J.S. Gnanaraj, H.J. Kim, Design of electrolyte solutions for Li and Li-ion batteries: A review, Electrochim. Acta. 50 (2004) 247–254. doi:10.1016/j.electacta.2004.01.090.

[36] Y. Ein-Eli, B. Markovsky, D. Aurbach, Y. Carmeli, H. Yamin, S. Luski, The dependence of the performance of Li-C intercalation anodes for Li-ion secondary batteries on the electrolyte solution composition, Electrochim. Acta. 39 (1994) 2559–2569. doi:10.1016/0013-4686(94)00221-5.

[37] a. M. Andersson, K. Edström, Chemical Composition and Morphology of the Elevated Temperature SEI on Graphite, J. Electrochem. Soc. 148 (2001) A1100. doi:10.1149/1.1397771.

[38] D. Aurbach, M. Koltypin, H. Teller, Y.S. Cohen, Why Graphite Electrodes Fail in Pc Solutions : An Insight From Morphological Studies, New Carbon Based Mater. Electrochem. Energy Storage Syst. Batter. Supercapacitors Fuel Cells. (2006) 197–211. doi:10.1007/1-4020-4812-2_15.

[39] H. Ekstrom, G. Lindbergh, A Model for Predicting Capacity Fade due to SEI Formation in a Commercial Graphite/LiFePO4 Cell, J. Electrochem. Soc. 162 (2015) A1003–A1007. doi:10.1149/2.0641506jes.

[40] H. Zheng, L. Zhang, G. Liu, X. Song, V.S. Battaglia, Correlationship between electrode

mechanics and long-term cycling performance for graphite anode in lithium ion cells, J. Power Sources. 217 (2012) 530–537. doi:10.1016/j.jpowsour.2012.06.045.

[41] J.O. Besenhard, M. Winter, J. Yang, W. Biberacher, Filming mechanism of lithium-carbon anodes in organic and inorganic electrolytes, J. Power Sources. 54 (1995) 228–231. doi:10.1016/0378-7753(94)02073-C.

[42] M.C. Smart, B. V. Ratnakumar, Lithium Plating in Lithium-Ion Cells, ECS Trans. 25 (36) (2010) 241–252. doi:10.1149/1.3393860.

[43] M.C. Smart, B. V. Ratnakumar, Effects of Electrolyte Composition on Lithium Plating in Lithium-Ion Cells, J. Electrochem. Soc. 158 (2011) A379. doi:10.1149/1.3544439.

[44] W. Lu, C.M. López, N. Liu, J.T. Vaughey, A. Jansen, D.W. Dees, Overcharge Effect on Morphology and Structure of Carbon Electrodes for Lithium-Ion Batteries, J. Electrochem. Soc. 159 (2012) A566. doi:10.1149/2.jes035205.

[45] J.W. Fergus, Recent developments in cathode materials for lithium ion batteries, J. Power Sources. 195 (2010) 939–954. doi:10.1016/j.jpowsour.2009.08.089.

[46] A.S. Aricò, P. Bruce, B. Scrosati, J.-M. Tarascon, W. van Schalkwijk, Nanostructured materials for advanced energy conversion and storage devices., Nat. Mater. 4 (2005) 366–377. doi:10.1038/nmat1368.

[47] X. Li, Y. Xu, C. Wang, Suppression of Jahn-Teller distortion of spinel LiMn2O4 cathode, J. Alloys Compd. 479 (2009) 310–313. doi:10.1016/j.jallcom.2008.12.081.

[48] M. Wohlfahrt-Mehrens, a. Butz, R. Oesten, G. Arnold, R.P. Hemmer, R. a. Huggins, The influence of doping on the operation of lithium manganese oxide spinel, J. Power Sources. 68 (1997) 582–585. doi:10.1016/S0378-7753(97)02624-4.

[49] M. Wohlfahrt-Mehrens, C. Vogler, J. Garche, Aging mechanisms of lithium cathode materials, J. Power Sources. 127 (2004) 58–64. doi:10.1016/j.jpowsour.2003.09.034.

[50] H. Zheng, Y. Fu, H. Zhang, T. Abe, Z. Ogumi, Pottasium Salts Electrolyte Additives for Enhancing Electrochemical Performances of Natural Graphite Anodes, Electrochem. Solid-State Lett. 9 (2006) A115. doi:10.1149/1.2161447.

[51] J. Li, E. Murphy, J. Winnick, P. a. Kohl, Studies on the cycle life of commercial lithium ion batteries during rapid charge-discharge cycling, J. Power Sources. 102 (2001) 294–301. doi:10.1016/S0378-7753(01)00821-7.

[52] G. Ning, B. Haran, B.N. Popov, Capacity fade study of lithium-ion batteries cycled at high discharge rates, J. Power Sources. 117 (2003) 160–169. doi:10.1016/S0378-7753(03)00029-6.

[53] J.S. Striebel, Kathryn A., Performance and Degradation Evaluation of Five Different Commercial Lithium-Ion Cells, Lawrence Berkeley Natl. Lab. (2004).

[54] M. Dubarry, C. Truchot, B.Y. Liaw, K. Gering, S. Sazhin, D. Jamison, C. Michelbacher, Evaluation of commercial lithium-ion cells based on composite positive electrode for plug-in hybrid electric vehicle applications. Part II. Degradation mechanism under 2 C

cycle aging, J. Power Sources. 196 (2011) 10336–10343. doi:10.1016/j.jpowsour.2011.08.078.

[55] D. Aurbach, B. Markovsky, A. Rodkin, M. Cojocaru, E. Levi, H.J. Kim, An analysis of rechargeable lithium-ion batteries after prolonged cycling, Electrochim. Acta. 47 (2002) 1899–1911. doi:10.1016/S0013-4686(02)00013-0.

[56] J.R. Belt, C.D. Ho, C.G. Motloch, T.J. Miller, T.Q. Duong, A capacity and power fade study of Li-ion cells during life cycle testing, J. Power Sources. 123 (2003) 241–246. doi:10.1016/S0378-7753(03)00537-8.

[57] R.B. Wright, J.P. Christophersen, C.G. Motloch, J.R. Belt, C.D. Ho, V.S. Battaglia, J.A. Barnes, T.Q. Duong, R.A. Sutula, Power fade and capacity fade resulting from cycle-life testing of advanced technology development program lithium-ion batteries, J. Power Sources. 119–121 (2003) 865–869. doi:10.1016/S0378-7753(03)00190-3.

[58] G. Ning, B.N. Popov, Cycle Life Modeling of Lithium-Ion Batteries, J. Electrochem. Soc. 151 (2004) A1584. doi:10.1149/1.1787631.

[59] T. Guena, P. Leblanc, How Depth of Discharge Affects the Cycle Life of Lithium-Metal-Polymer Batteries, INTELEC 06 - Twenty-Eighth Int. Telecommun. Energy Conf. (2006) 1–8. doi:10.1109/INTLEC.2006.251641.

[60] J. Cannarella, C.B. Arnold, Stress evolution and capacity fade in constrained lithium-ion pouch cells, J. Power Sources. 245 (2014) 745–751. doi:10.1016/j.jpowsour.2013.06.165.

[61] T. Osaka, S. Nakade, M. Rajamäki, T. Momma, Influence of capacity fading on commercial lithium-ion battery impedance, J. Power Sources. 119–121 (2003) 929–933. doi:10.1016/S0378-7753(03)00233-7.

[62] D.P. Abraham, J.L. Knuth, D.W. Dees, I. Bloom, J.P. Christophersen, Performance degradation of high-power lithium-ion cells-Electrochemistry of harvested electrodes, J. Power Sources. 170 (2007) 465–475. doi:10.1016/j.jpowsour.2007.03.071.

[63] J. Belt, V. Utgikar, I. Bloom, Calendar and PHEV cycle life aging of high-energy, lithium-ion cells containing blended spinel and layered-oxide cathodes, J. Power Sources. 196 (2011) 10213–10221. doi:10.1016/j.jpowsour.2011.08.067.

[64] DOE/ID-11069, FreedomCAR Battery Test Manual For Power-Assist Hybrid Electric Vehicles, (2003).

[65] M. Ecker, N. Nieto, S. Käbitz, J. Schmalstieg, H. Blanke, A. Warnecke, D.U. Sauer, Calendar and cycle life study of Li(NiMnCo)O2-based 18650 lithium-ion batteries, J. Power Sources. 248 (2014) 839–851. doi:10.1016/j.jpowsour.2013.09.143.

[66] P. Nieho, S. Passerini, M. Winter, Interface Investigations of a Commercial Lithium Ion Battery Graphite Anode Material by Sputter Depth Pro fi le X - ray Photoelectron Spectroscopy, (2013).

[67] J. Marcicki, A. Bartlett, M. Canova, A.T. Conlisk, G. Rizzoni, Y. Guezennec, X.G. Yang, T. Miller, Characterization of Cycle-Life Aging in Automotive Lithium-Ion Pouch Cells, ECS Trans. 50 (2013) 235–247. doi:10.1149/05026.0235ecst.

[68] X. Han, M. Ouyang, L. Lu, J. Li, Y. Zheng, Z. Li, A comparative study of commercial lithium ion battery cycle life in electrical vehicle: Aging mechanism identification, J. Power Sources. 251 (2014) 38–54. doi:10.1016/j.jpowsour.2013.11.029.

[69] A. Cordoba-Arenas, S. Onori, Y. Guezennec, G. Rizzoni, Capacity and power fade cycle-life model for plug-in hybrid electric vehicle lithium-ion battery cells containing blended spinel and layered-oxide positive electrodes, J. Power Sources. 278 (2015) 473–483. doi:10.1016/j.jpowsour.2014.12.047.

[70] M. Dubarry, A. Devie, B.Y. Liaw, The Value of Battery Diagnostics and Prognostics, J. Energy Power Sources. 1 (2014) 242–249.

[71] M. Dubarry, B.Y. Liaw, Development of a universal modeling tool for rechargeable lithium batteries, J. Power Sources. 174 (2007) 856–860. doi:10.1016/j.jpowsour.2007.06.157.

[72] M. Dubarry, C. Truchot, B.Y. Liaw, Synthesize battery degradation modes via a diagnostic and prognostic model, J. Power Sources. 219 (2012) 204–216. doi:10.1016/j.jpowsour.2012.07.016.

[73] M. Dubarry, C. Truchot, B.Y. Liaw, Cell degradation in commercial LiFePO4 cells with high-power and high-energy designs, J. Power Sources. 258 (2014) 408–419. doi:10.1016/j.jpowsour.2014.02.052.

[74] A. Bartlett, J. Marcicki, S. Onori, G. Rizzoni, X.G. Yang, T. Miller, Electrochemical Model-Based State of Charge and Capacity Estimation for a Composite Electrode Lithium-Ion Battery, Control Syst. Technol. IEEE Trans. PP (2015) 1. doi:10.1109/TCST.2015.2446947.

[75] A. Bartlett, J. Marcicki, K. Rhodes, G. Rizzoni, State of health estimation in composite electrode lithium-ion cells, J. Power Sources. 284 (2015) 642–649. doi:10.1016/j.jpowsour.2015.03.080.

[76] J. Marcicki, M. Canova, a. T. Conlisk, G. Rizzoni, Design and parametrization analysis of a reduced-order electrochemical model of graphite/LiFePO4 cells for SOC/SOH estimation, J. Power Sources. 237 (2013) 310–324. doi:10.1016/j.jpowsour.2012.12.120.

[77] B.Y. Liaw, G. Nagasubramanian, R.G. Jungst, D.H. Doughty, Modeling of lithium ion cells - A simple equivalent-circuit model approach, Solid State Ionics. 175 (2004) 835–839. doi:10.1016/j.ssi.2004.09.049.

[78] J. Newman, W. Tiedemann, Porous-electrode theory with battery applications, AIChE J. 21 (1975) 25–41. doi:10.1002/aic.690210103.

[79] P. Ramadass, B. Haran, R. White, B.N. Popov, Mathematical modeling of the capacity fade of Li-ion cells, J. Power Sources. 123 (2003) 230–240. doi:10.1016/S0378-7753(03)00531-7.

[80] X. Zhang, Multiscale Modeling of Li-ion Cells: Mechanics, Heat Generation and Electrochemical Kinetics, (2009) 1–178.

[81] G.-H. Kim, K. Smith, K.-J. Lee, S. Santhanagopalan, A. Pesaran, Multi-Domain Modeling

of Lithium-Ion Batteries Encompassing Multi-Physics in Varied Length Scales, J. Electrochem. Soc. 158 (2011) A955. doi:10.1149/1.3597614.

[82] A. Shabbir, K. Gallegher, P. Nelson, N. Susarla, D. Dees, BatPaC Model Development, in: DOE Veh. Technol. Off. Annu. Merit Rev. Peer Eval. Meet., Washington, DC, 2016.

[83] M. Guo, R.E. White, An approximate solution for solid-phase diffusion in a spherical particle in physics-based Li-ion cell models, J. Power Sources. 198 (2012) 322–328. doi:10.1016/j.jpowsour.2011.08.096.

[84] S. LIU, An analytical solution to Li/Li+ insertion into a porous electrode, Solid State Ionics. 177 (2006) 53–58. doi:10.1016/j.ssi.2005.09.053.

[85] V.R. Subramanian, J.A. Ritter, R.E. White, Approximate Solutions for Galvanostatic Discharge of Spherical Particles I. Constant Diffusion Coefficient, J. Electrochem. Soc. 148 (2001) E444–E449. doi:10.1149/1.1409397.

[86] A.P. Bartlett, Electrochemical Model-Based State of Charge and State of Health Estimation of Lithium-Ion Batteries, 2015.

[87] J.C. Forman, S. Bashash, J.L. Stein, H.K. Fathy, Reduction of an Electrochemistry-Based Li-Ion Battery Model via Quasi-Linearization and Padé Approximation, J. Electrochem. Soc. 158 (2011) A93–A101. doi:10.1149/1.3519059.

[88] T. Hang, D. Mukoyama, H. Nara, N. Takami, T. Momma, T. Osaka, Electrochemical impedance spectroscopy analysis for lithium-ion battery using Li4Ti5O12 anode, J. Power Sources. 222 (2013) 442–447. doi:10.1016/j.jpowsour.2012.09.010.

[89] W. Waag, S. Käbitz, D.U. Sauer, Experimental investigation of the lithium-ion battery impedance characteristic at various conditions and aging states and its influence on the application, Appl. Energy. 102 (2013) 885–897. doi:10.1016/j.apenergy.2012.09.030.

[90] C.H. Chen, J. Liu, M.E. Stoll, G. Henriksen, D.R. Vissers, K. Amine, Aluminum-doped lithium nickel cobalt oxide electrodes for high-power lithium-ion batteries, J. Power Sources. 128 (2004) 278–285. doi:10.1016/j.jpowsour.2003.10.009.

[91] D.. Abraham, J. Liu, C.. Chen, Y.. Hyung, M. Stoll, N. Elsen, S. MacLaren, R. Twesten, R. Haasch, E. Sammann, I. Petrov, K. Amine, G. Henriksen, Diagnosis of power fade mechanisms in high-power lithium-ion cells, J. Power Sources. 119–121 (2003) 511–516. doi:10.1016/S0378-7753(03)00275-1.

[92] U. Tröltzsch, O. Kanoun, H.-R. Tränkler, Characterizing aging effects of lithium ion batteries by impedance spectroscopy, Electrochim. Acta. 51 (2006) 1664–1672. doi:10.1016/j.electacta.2005.02.148.

[93] R. Kizilel, a. Lateef, R. Sabbah, M.M. Farid, J.R. Selman, S. Al-Hallaj, Passive control of temperature excursion and uniformity in high-energy Li-ion battery packs at high current and ambient temperature, J. Power Sources. 183 (2008) 370–375. doi:10.1016/j.jpowsour.2008.04.050.

[94] S. Al-Hallaj, R. Kizilel, a. Lateef, R. Sabbah, M. Farid, J.R. Selman, Passive Thermal Management Using Phase Change Material (PCM) for EV and HEV Li ion Batteries,

2005 IEEE Veh. Power Propuls. Conf. (2005) 376–380. doi:10.1109/VPPC.2005.1554585.

[95] X. Wang, Y. Sone, G. Segami, H. Naito, C. Yamada, K. Kibe, Understanding Volume Change in Lithium-Ion Cells during Charging and Discharging Using In Situ Measurements, J. Electrochem. Soc. 154 (2007) A14. doi:10.1149/1.2386933.

[96] C. Peabody, C.B. Arnold, The role of mechanically induced separator creep in lithium-ion battery capacity fade, J. Power Sources. 196 (2011) 8147–8153. doi:10.1016/j.jpowsour.2011.05.023.

[97] M. Kassem, C. Delacourt, Postmortem analysis of calendar-aged graphite/LiFePO4 cells, J. Power Sources. 235 (2013) 159–171. doi:10.1016/j.jpowsour.2013.01.147.

[98] B. Stiaszny, J.C. Ziegler, E.E. Krauß, J.P. Schmidt, E. Ivers-Tiffée, Electrochemical characterization and post-mortem analysis of aged LiMn2O4–Li(Ni0.5Mn0.3Co0.2)O2/graphite lithium ion batteries. Part I: Cycle aging, J. Power Sources. 251 (2014) 439–450. doi:10.1016/j.jpowsour.2013.11.080.

[99] T. Sasaki, T. Nonaka, H. Oka, C. Okuda, Y. Itou, Y. Kondo, Y. Takeuchi, Y. Ukyo, K. Tatsumi, S. Muto, Capacity-Fading Mechanisms of LiNiO2-Based Lithium-Ion Batteries , J. Electrochem. Soc. . 156 (2009) A289–A293. doi:10.1149/1.3076136.

[100] K.J. Kim, Y.N. Jo, W.J. Lee, T. Subburaj, K. Prasanna, C.W. Lee, Effects of inorganic salts on the morphological, structural, and electrochemical properties of prepared nickel-rich Li[Ni0.6Co0.2Mn0.2]O2, J. Power Sources. 268 (2014) 349–355. doi:10.1016/j.jpowsour.2014.06.057.

[101] E. Markervich, G. Salitra, M.D. Levi, D. Aurbach, Capacity fading of lithiated graphite electrodes studied by a combination of electroanalytical methods, Raman spectroscopy and SEM, J. Power Sources. 146 (2005) 146–150. doi:10.1016/j.jpowsour.2005.03.107.

[102] L. Yang, B. Ravdel, B.L. Lucht, Electrolyte Reactions with the Surface of High Voltage LiNi[sub 0.5]Mn[sub 1.5]O[sub 4] Cathodes for Lithium-Ion Batteries, Electrochem. Solid-State Lett. 13 (2010) A95. doi:10.1149/1.3428515.

[103] T. Coupar, Personal Communication, (2015).

[104] S.J. Kline, F.A. McClintock, Describing Uncertainties in Single-Sample Experiments, in: Mech. Eng, 1953: p. 3.

[105] R. Deshpande, M. Verbrugge, Y. Cheng, J. Wang, P. Liu, Battery Cycle Life Prediction with Coupled Chemical Degradation and Fatigue Mechanics, 159 (2012) 1730–1738. doi:10.1149/2.049210jes.

[106] I. Bloom, J.P. Christophersen, D.P. Abraham, K.L. Gering, Differential voltage analyses of high-power lithium-ion cells, J. Power Sources. 157 (2006) 537–542. doi:10.1016/j.jpowsour.2005.07.054.

[107] P. Yu, B.N. Popov, J. a Ritter, R.E. White, Determination of the Lithium Ion Diffusion Coefficient in Graphite, J. Electrochem. Soc. 146 (1999) 8–14. doi:10.1149/1.1391556.

[108] X. Feng, J. Sun, M. Ouyang, X. He, L. Lu, X. Han, M. Fang, H. Peng, Characterization of large format lithium ion battery exposed to extremely high temperature, J. Power Sources. 272 (2014) 457–467. doi:10.1016/j.jpowsour.2014.08.094.

[109] M. Dubarry, V. Svoboda, R. Hwu, B. Yann Liaw, Incremental Capacity Analysis and Close-to-Equilibrium OCV Measurements to Quantify Capacity Fade in Commercial Rechargeable Lithium Batteries, Electrochem. Solid-State Lett. 9 (2006) A454–A457. doi:10.1149/1.2221767.

[110] J. Fuller, Thomas F. Doyle, Marc. Newman, Simulation and Optimization of the Dual Lithium Ion Insertion Cell, J. Electrochem. Soc. 141 (1994) 1. doi:10.1149/1.2054684.

[111] M.W. Verbrugge, B.J. Koch, Modeling Lithium Intercalation of Single-Fiber Carbon Microelectrodes, J. Electrochem. Soc. 143 (1996) 600. doi:10.1149/1.1836486.

[112] A.J. Bard, L.R. Faulkner, Electrochemical methods : fundamentals and applications, Wiley, 2001.

[113] J.S. Newman, K.E. Thomas-Alyea, Electrochemical systems, J. Wiley, 2004.

[114] B. Weigand, Analytical methods for heat transfer and fluid flow problems, n.d.

[115] B.R. Hunt, R.L. Lipsman, J.M. (Jonathan M. Rosenberg, A guide to MATLAB : for beginners and experienced users, Cambridge University Press, 2006.

[116] K.M. Shaju, G. V. Subba Rao, B.V.R. Chowdari, Influence of Li-Ion Kinetics in the Cathodic Performance of Layered Li(Ni[sub 1/3]Co[sub 1/3]Mn[sub 1/3])O[sub 2], J. Electrochem. Soc. 151 (2004) A1324. doi:10.1149/1.1775218.

[117] S. Krachovskiy, A. Pauric, Slice-Selective NMR Diffusion Measurements-a Robust and Reliable Tool for in situ Characterization of Ion Transport Properties in Lithium Ion Battery Electrolytes., J. …. (2013) 2–6. doi:10.1021/jz402103f.

[118] D.A.G. Bruggeman, Berechnung verschiedener physikalischer Konstanten von heterogenen Substanzen. III. Die elastischen Konstanten der quasiisotropen Mischkorper aus isotropen Substanzen, Ann. Phys. 421 (1935) 160–178. doi:10.1002/andp.19374210205.

[119] B. Tjaden, S.J. Cooper, D.J. Brett, D. Kramer, P.R. Shearing, On the origin and application of the Bruggeman correlation for analysing transport phenomena in electrochemical systems, Curr. Opin. Chem. Eng. 12 (2016) 44–51. doi:10.1016/j.coche.2016.02.006.

[120] M.D. Levi, D. Aurbach, Diffusion coefficients of lithium ions during intercalation into graphite derived from the simultaneous measurements and modeling of electrochemical impedance and potentiostatic intermittent titration characteristics of thin graphite electrodes, J. Phys. Chem. B. 101 (1997) 4641–4647. doi:10.1021/jp9701911.

[121] S. Miyoshi, H. Nagano, T. Fukuda, T. Kurihara, M. Watanabe, S. Ida, T. Ishihara, Dual-Carbon Battery Using High Concentration $LiPF_6$ in Dimethyl Carbonate (DMC) Electrolyte, J. Electrochem. Soc. 163 (2016) A1206–A1213. doi:10.1149/2.0381607jes.

[122] K. Hayamizu, Temperature dependence of self-diffusion coefficients of ions and solvents in ethylene carbonate, propylene carbonate, and diethyl carbonate single solutions and ethylene carbonate + diethyl carbonate binary solutions of LiPF 6 studied by NMR, J. Chem. Eng. Data. 57 (2012) 2012–2017. doi:10.1021/je3003089.

[123] Z.K. Tang, J.S. Tse, L.M. Liu, Unusual Li-Ion Transfer Mechanism in Liquid Electrolytes: A First-Principles Study, J. Phys. Chem. Lett. 7 (2016) 4795–4801. doi:10.1021/acs.jpclett.6b02351.

[124] L. Yang, A. Xiao, B.L. Lucht, Investigation of solvation in lithium ion battery electrolytes by NMR spectroscopy, J. Mol. Liq. 154 (2010) 131–133. doi:10.1016/j.molliq.2010.04.025.

[125] J. Zhao, L. Wang, X. He, C. Wan, C. Jiang, Determination of Lithium-Ion Transference Numbers in LiPF[sub 6]–PC Solutions Based on Electrochemical Polarization and NMR Measurements, J. Electrochem. Soc. 155 (2008) A292–A296. doi:10.1149/1.2837832.

[126] D. Aurbach, B. Markovsky, M.. Levi, E. Levi, a Schechter, M. Moshkovich, Y. Cohen, New insights into the interactions between electrode materials and electrolyte solutions for advanced nonaqueous batteries, J. Power Sources. 81–82 (1999) 95–111. doi:10.1016/S0378-7753(99)00187-1.

[127] K. Amine, C.H. Chen, J. Liu, M. Hammond, a. Jansen, D. Dees, I. Bloom, D. Vissers, G. Henriksen, Factors responsible for impedance rise in high power lithium ion batteries, J. Power Sources. 97–98 (2001) 684–687. doi:10.1016/S0378-7753(01)00701-7.

[128] Y. Hu, S. Yurkovich, Y. Guezennec, B.J. Yurkovich, Electro-thermal battery model identification for automotive applications, J. Power Sources. 196 (2011) 449–457. doi:10.1016/j.jpowsour.2010.06.037.

[129] B. Saha, K. Goebel, Modeling Li-ion battery capacity depletion in a particle filtering framework, Proc. Annu. Conf. Progn. Heal. Manag. Soc. (2009) 2909--2924. https://www.phmsociety.org/sites/phmsociety.org/files/phm_submission/2009/phmc_09_38.pdf.

[130] M. Reichert, D. Andre, A. Rösmann, P. Janssen, H.G. Bremes, D.U. Sauer, S. Passerini, M. Winter, Influence of relaxation time on the lifetime of commercial lithium-ion cells, J. Power Sources. 239 (2013) 45–53. doi:10.1016/j.jpowsour.2013.03.053.

[131] M. Ecker, J.B. Gerschler, J. Vogel, S. Käbitz, F. Hust, P. Dechent, D.U. Sauer, Development of a lifetime prediction model for lithium-ion batteries based on extended accelerated aging test data, J. Power Sources. 215 (2012) 248–257. doi:10.1016/j.jpowsour.2012.05.012.

[132] I. Bloom, L.K. Walker, J.K. Basco, D.P. Abraham, J.P. Christophersen, C.D. Ho, Differential voltage analyses of high-power lithium-ion cells. 4. Cells containing NMC, J. Power Sources. 195 (2010) 877–882. doi:10.1016/j.jpowsour.2009.08.019.

[133] L. Su, J. Zhang, J. Huang, H. Ge, Z. Li, F. Xie, B.Y. Liaw, Path dependence of lithium ion cells aging under storage conditions, J. Power Sources. 315 (2016) 35–46. doi:http://dx.doi.org/10.1016/j.jpowsour.2016.03.043.

[134] I. Bloom, L.K. Walker, J.K. Basco, D.P. Abraham, J.P. Christophersen, C.D. Ho, Differential voltage analyses of high-power lithium-ion cells 3. Another anode phenomenon, J. Power Sources. 195 (2010) 877–882. doi:10.1016/j.jpowsour.2009.08.019.

[135] D. Rahner, The role of anions, solvent molecules and solvated electrons in layer formation processes on anode materials for rechargeable lithium batteries, J. Power Sources. 81–82 (1999) 358–361. doi:10.1016/S0378-7753(98)00218-3.

[136] F. La Mantia, C.D. Wessells, H.D. Deshazer, Y. Cui, Reliable reference electrodes for lithium-ion batteries, Electrochem. Commun. 31 (2013) 141–144. doi:10.1016/j.elecom.2013.03.015.

[137] J. Marcicki, G. Rizzoni, M. Canova, Y. Guezennec, Modeling, Parametrization, and Diagnostics for Lithium-Ion Batteries with Automotive Applications Graduate Program in Graduate Program in Mechanical Engineering, (2012). https://etd.ohiolink.edu/rws_etd/document/get/osu1354652448/inline (accessed June 28, 2017).

[138] I. Bloom, A.N. Jansen, D.P. Abraham, J. Knuth, S. a. Jones, V.S. Battaglia, G.L. Henriksen, Differential voltage analyses of high-power, lithium-ion cells 1. Technique and application, J. Power Sources. 139 (2005) 295–303. doi:10.1016/j.jpowsour.2004.07.021.

[139] M. Dubarry, B.Y. Liaw, M.-S. Chen, S.-S. Chyan, K.-C. Han, W.-T. Sie, S.-H. Wu, Identifying battery aging mechanisms in large format Li ion cells, J. Power Sources. 196 (2011) 3420–3425. doi:10.1016/j.jpowsour.2010.07.029.

[140] M. Dubarry, B.Y. Liaw, Identify capacity fading mechanism in a commercial LiFePO4 cell, J. Power Sources. 194 (2009) 541–549. doi:10.1016/j.jpowsour.2009.05.036.

[141] J. Schindelin, I. Arganda-Carreras, E. Frise, V. Kaynig, M. Longair, T. Pietzsch, S. Preibisch, C. Rueden, S. Saalfeld, B. Schmid, J.-Y. Tinevez, D.J. White, V. Hartenstein, K. Eliceiri, P. Tomancak, A. Cardona, Fiji: an open-source platform for biological-image analysis, Nat. Methods. 9 (2012) 676–682. doi:10.1038/nmeth.2019.